U(VI) retention by Ca-bentonite and clay minerals at (hyper)alkaline conditions

D I S S E R T A T I O N

zur Erlangung des akademischen Grades

Doctor rerum naturalium
(Dr. rer. nat.)

vorgelegt

dem Bereich Mathematik und Naturwissenschaften der
Technischen Universität Dresden

von

MSc. Angewandte Geowissenschaften, Thimo Philipp

Geboren am 04.04.1988 in Linnich

Eingereicht im am 23.10.2019
Disputation und Rigorosum am 28.01.2020

Acknowledgements

Content

List of abbreviations and symbols

a.u.	arbitrary units
ATR FT-IR	attenuated total reflectance Fourier transform infrared
BET	Brunauer Emmet Teller
C-(A)-S-H	calcium (aluminum) silicate hydrate
CT	charge transfer
CTR	crystal truncation rod
DIC	dissolved inorganic carbon
E	resonant electronic transition line
EDX	energy dispersive X-ray spectroscopy
ESI-MS	electrospray ionization mass spectrometry
ESR	electron spin resonance
ESRF	European Synchrotron Radiation Facility
EXAFS	extended X-ray absorption fine structure
FEP	fluorinated ethylene propylene
GHS	Gipshut solution
HC	high carbonate concentration
HOMO	highest occupied molecular orbital
IC	internal conversion
ICP-MS	inductively coupled plasma mass spectrometry
IND	semi-empirical indicator function
ISA	isosaccharinic acid
ISC	inter system crossing
ITFA	iterative target transformation factor analysis
ITT	iterative target test
LC	low carbonate concentration
LSC	liquid scintillation counting
LUMO	lowest unoccupied molecular orbital
M	metal
MS	multiple scattering
N_2	experiments in nitrogen atmosphere
NMR	nuclear magnetic resonance
PCS	photon correlation spectroscopy
PE	polyethylene
RAXR	resonant anomalous X-ray reflectivity
RN	radionuclide
S	a) surface, b) lines of vibronic progression in uranyl luminescence
S/L	solid to liquid ratio
SCM	surface complexation modelling

SEM	scanning electron microscopy
TRLFS	time-resolved laser-induced luminescence spectroscopy
VR	vibrational relaxation
XANES	X-ray absorption near-edge structure
XAS	X-ray absorption spectroscopy
XRD	X-ray diffraction

A	pH correction parameter
a_{eq}	equilibrium amount of substance sorbed on a solid in mol/L
a_m	maximum amount of substance that can be sorbed on a solid
β	stability constant
b	Langmuir sorption coefficient
c_0	initial concentration in mol/L
c_{eq}	equilibrium concentration in mol/L
CN	coordination number
d	sample thickness
d_L	distance between crystallographic units
E_0	ionization energy in eV
E_h	redox potential
F	structure factor in X-ray reflectivity measurements
f	atomic scattering factor in X-ray reflectivity measurements
I	a) ionic strength in mol/L, b) intensity
k	wavenumber of photoelectron in Å^{-1}
K_d	distribution coefficient in L/kg
K_F	Freundlich coefficient in m^3/kg
λ	wavelength in nm
m	mass in kg
μ_E	absorption coefficient
n	number of components
n_F	Freundlich exponent
v_s	total symmetric stretch vibration in cm^{-1}
q	momentum transfer in Å^{-1}
R	radial distance between atoms
σ^2	Debye-Waller factor
τ	luminescence lifetime in μs
t_i	delay time
V	volume in L
$\chi(E)$	EXAFS function
z	charge of an ion

Summary

Clays are considered as potential host rocks and backfill material for deep geological repositories for radioactive waste. Therefore, profound understanding of radionuclide retention processes at clay mineral surfaces is essential for a long-term safety assessment. This understanding has already been generated in the past for simple chemical systems, in which experiments are easy to conduct and interpretation is straightforward. However, there is still a lack of molecular process understanding when considering complex natural systems (low radionuclide concentrations, high ionic strength, high pH values, multi-mineral solid phases, complex solution composition). This thesis aims to close some of these knowledge gaps, focusing on U(VI) and Np(VI) sorption on clays at (hyper)alkaline conditions. pH values between 10 and 13 can prevail in the near-field of a radioactive waste repository as a result of the degradation of concrete, which is part of the geo-engineered barrier. Existing studies on radionuclide sorption on clays do not exceed pH 10. Therefore, within this work, a comprehensive investigation in the pH range 8-13 was conducted. This included the quantification of radionuclide retention in batch sorption experiments as well as spectroscopic investigations to generate understanding about the underlying retention mechanisms on a molecular level. Beside the pH, additional focus was on the influence of dissolved carbonate and calcium on radionuclide sorption at (hyper)alkaline conditions.

Next to two small chapters dealing with the stability and surface charge of Ca-bentonite at (hyper)alkaline conditions (chapter 4.1) and the influence of ISA on U(VI) sorption at high pH values (chapter 4.3), the thesis can be subdivided in two major parts. The first part (chapter 4.2) is a detailed investigation of U(VI) sorption on Ca-bentonite at (hyper)alkaline conditions in mixed electrolyte solutions. Batch sorption experiments were conducted, varying a number of experimental parameters (sorption time, S/L ratio, U(VI) concentration, pH value, carbonate concentration) and assessing their effect on U(VI) sorption. In order to be able to explain the observed sorption behavior, next to U(VI) solubility tests, spectroscopic techniques were applied. The aqueous speciation of U(VI) was investigated with TRLFS, while its surface speciation was probed with ATR FT-IR, site-selective TRLFS, EXAFS and CTR/RAXR. Since the results of this chapter indicated a great importance of the presence of calcium (see below), the second major part of the thesis (chapter 4.4) was dedicated to a careful evaluation of the influence of calcium on An(VI) sorption on clay minerals at (hyper)alkaline conditions. This encompasses the sorption of Ca(II) on Ca-bentonite and its effect on the bentonite surface charge. Furthermore, U(VI) batch sorption experiments with Na-montmorillonite, synthetic kaolinite and muscovite were conducted in 0.1 M NaCl as well as in 0.1 M NaCl + 0.02 M $CaCl_2$ at pH 8-13, in order to quantify the influence of calcium on U(VI) sorption on supposedly Ca-free mineral phases. Site-selective TRLFS was applied with the aim to observe U(VI) sorption species involving calcium. Finally, complementary sorption experiments Np(VI) on muscovite were performed in order to check whether its sorption behavior is analogous to U(VI) under the given conditions.

Batch sorption experiments demonstrate that U(VI) retention on Ca-bentonite can be very effective at pH > 10, even in the presence of carbonate and despite the prevalence of anionic aqueous species. Above a certain pH, depending on the concentration of carbonate in solution, carbonate does not play a role in the aqueous U(VI) speciation anymore due to the predominance of hydrolysis. TRLFS measurements revealed a clear correlation between sorption behavior and aqueous U(VI) speciation, showing that retention reaches a maximum at pH 10-12, where $UO_2(OH)_3^-$ is the predominant aqueous species. This raised the question whether the strong retention can be achieved by adsorption of an anionic species to the negatively charged mineral surface or rather by precipitation of uranates. By *in situ* ATR FT-IR and CTR/RAXR experiments the formation of U(VI) precipitates on the mineral surface was observed at U(VI) concentrations of 2×10^{-5} M and 5×10^{-5} M, respectively. However, solubility tests at sub-micromolar U(VI) concentrations, which were also applied in the batch sorption experiments, showed that the observed complete U(VI) removal at pH 10-12 cannot be attributed to precipitation of (earth) alkali-uranates from the solution. In order to unambiguously distinguish between surface precipitation and surface complexation, direct spectroscopic investigations of the U(VI) complexes on the Ca-bentonite surface were performed with site-selective TRLFS and EXAFS. The occurrence of luminescence line-narrowing and the frequency of the total symmetric stretch vibration obtained from the site-selective TRLFS emission spectra, indicate the presence of two U(VI) surface complexes. Also EXAFS spectroscopy confirmed the presence of two independent U(VI) sorption species on Ca-bentonite at pH 8-13. With increasing pH, the nature of the retained U(VI) complexes shifts from bidentate inner-sphere surface complexes with an overall equatorial coordination of five adsorbed on aluminol or silanol edge sites to surface complexes with a 4-fold equatorial coordination, resembling the aqueous species $UO_2(OH)_4^{2-}$. For the first time, a 4-fold coordination in the equatorial plane of U(VI) was univocally proven with the help of a multiple-scattering feature originating from the strong symmetry of the complexes, and without the need for error-prone shell fitting. The lack of scattering paths from the substrate and the comparatively high value for the total symmetric stretch vibration indicate that the high-pH-component is an outer-sphere complex.

Concerning the character of the second sorption species at very high pH it was hypothesized that the anionic uranyl hydroxide complexes are mediated to the surface by calcium cations. It was found that calcium sorbs strongly on Ca-bentonite between pH 8 and 13. Also zeta potential measurements showed a partial compensation of the strongly negative surface charge of Ca-bentonite due to adsorption of calcium. U(VI) sorption on kaolinite and muscovite was strongly reduced in the absence of calcium at pH > 10. An increased retention upon addition of calcium proved the sorption enhancing effect of calcium at pH 10-12. Site-selective TRLFS allowed the spectroscopic observation and identification of calcium-induced U(VI) sorption complexes on muscovite. The obtained spectra correspond to the outer-sphere species found on Ca-bentonite. Combining the findings from batch sorption, zeta potential,

TRLFS and EXAFS suggests that calcium adsorbs to the mineral surface in the first place, displaying locally positively charged sites which enable an electrostatically driven attachment of anionic uranyl hydroxides. The same effect could also be demonstrated for Np(VI) sorption on muscovite, which was also strongly enhanced in the presence of calcium at pH 9-12.

ISA leads to a mobilization of U(VI) at (hyper)alkaline conditions only when present in very high excess of U(VI). A reduction of sorption on Ca-bentonite and the formation of aqueous U(VI)-ISA complexes, detected with TRLFS, occurred at an U:ISA ratio of 1:100,000. Such conditions are not likely to be found in deep geological repository environments.

Based on these findings it can be concluded that under certain alkaline repository conditions, where precipitation does not occur (due to very low concentrations or kinetic restraints), U(VI) and Np(VI) are still effectively retained in argillaceous minerals and rocks by adsorption despite the anionic character of prevailing aqueous species. Repulsive forces between the actinide species and the mineral surfaces are overcome by mediating Ca^{2+}. This finding is of great relevance, as also the migration of very small amounts of uranium or neptunium out of waste repositories could lead to a hazardous accumulation in the long term. The achieved knowledge gain concerning radionuclide retention at environmental conditions helps to take the next step towards realistic long-term safety assessment of nuclear waste repositories.

1. Introduction

1.1. Motivation

Radioactive waste, originating from nuclear power plants, military, industrial and medical applications, poses a threat to the human health due to its radio- and chemotoxic properties when migrating through the subsurface and entering the food chain. Therefore, a secure and effective disposal of such waste over long time spans must be guaranteed. As the mobility of radionuclides in the subsurface depends on their interactions with mineral surfaces, profound understanding of the physical and chemical processes at the interface between radionuclide bearing solutions and rocks/minerals (see chapter 2.3) is essential for the long-term safety assessment of deep geological nuclear waste repositories.

Particularly favorable properties for radionuclide retention are provided by clay minerals (see chapter 2.2). Clays are present in deep geological repositories for nuclear waste as potential host rock as well as in the form of bentonite, which is used as buffer and backfill material (see chapter 1.3). In the past, radionuclide retention by argillaceous material was mainly investigated under highly simplified laboratory conditions, such as pure minerals and electrolyte solutions, low ionic strengths and acidic or neutral pH. There is still a lack of understanding about radionuclide retention and migration at conditions prevailing in the near-field of a repository, where pore waters can be highly saline and alkaline and contain a number of different ions. The focus of the present work is on radionuclide retention on clay minerals at (highly) alkaline conditions. This is relevant, as the presence of concrete in a potential nuclear waste repository will cause a rise of pH upon water ingress. Promoted by the high ionic strength of the groundwater in potential host rock formations (see chapter 1.3), the concrete degrades and releases components that lead to the evolution of hyperalkaline cement pore waters ($10 < pH < 13$) (Berner, 1992; Gaucher *et al.*, 2006; Seher and Bracke, 2012). Such a shift in pore water chemistry can radically alter the retention potential of clay minerals towards radionuclides.

Among the radionuclides contained in the nuclear waste matrix, uranium is of special interest, since it represents by far the largest fraction of high-level radioactive waste (95.5%) (Figure 1). While it is not a major contributor to the overall radiotoxicity of spent nuclear fuel in the early stage of a waste repository, it becomes the main source of radiotoxicity in the form of ^{233}U after approx. 200,000 years, as being part of the ^{241}Pu decay chain (Kessler, 2012). Neptunium, initially present in the spent nuclear fuel in only minor amounts (approx. 0.03%), becomes a main source of radiotoxicity after 100,000 years, because its concentration in the nuclear waste increases with time due to the decay of ^{241}Am to ^{237}Np (Kaszuba and Runde, 1999). Due to the long half-life of ^{238}U, ^{233}U and ^{237}Np, an effective enclosure of these actinides in the repository is essential. A comparison of the sorption behavior of uranium and

neptunium is worthwhile, as both actinides feature similar redox chemistry and aqueous speciation (see chapter 2.1). In chapter 2.4, existing literature about U(VI), Np(V) and Np(VI) sorption on clay minerals is reviewed. The motivation of this work arises from the obvious gap in consistent and comprehensive sorption data at pH > 10. Beside the lack of reliable distribution coefficients and thermodynamic data which could feed databases for predictive sorption modelling, no molecular process understanding concerning the underlying retention mechanisms has been generated so far.
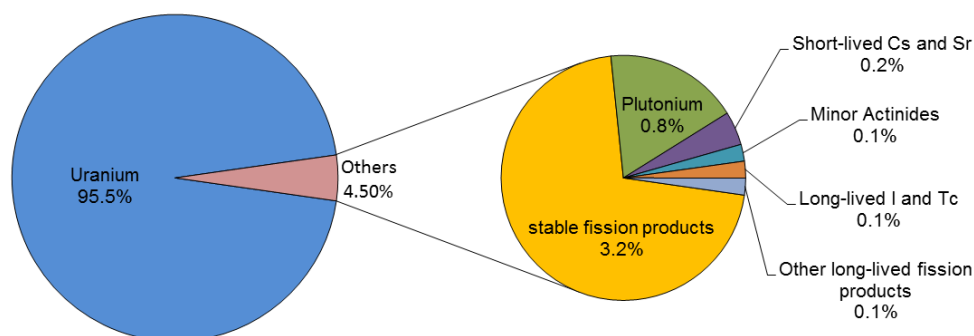
Figure 1: Composition of spent nuclear fuel of a standard pressurized water reactor with UO_2 fuel, irradiated up to a burn-up of 33 GWd/t (data from OECD/NEA (2006)).

1.2. Aim and scope of the thesis

The aim of the thesis was to describe and explain the sorption behavior of U(VI) and Np(VI) on clay minerals at (hyper)alkaline conditions in order to close knowledge gaps relevant for the safety assessment of deep geological nuclear waste repositories.

Batch sorption experiments were conducted in the first place, describing and quantifying the radionuclide retention on a macroscopic level. A number of experimental parameters (S/L ratio, radionuclide concentration, pH, sorption time, mineral phase, background electrolyte, carbonate concentration, presence of calcium and organic ligands) were varied, in order to assess their effect on radionuclide sorption. The batch experiments alone provide already substantial knowledge gain as they present for the first time a systematic study of the U(VI) and Np(VI) retention by clay rock from weakly alkaline to hyperalkaline pH.

In addition to these macroscopic and quantitative considerations, a main goal of the thesis was to shed light on the underlying radionuclide retention mechanisms at (hyper)alkaline conditions, generating process understanding on the molecular level. Different spectroscopic techniques were applied in order to differentiate between surface complexation and surface precipitation and to identify different contaminant species on the clay mineral surfaces. Time-resolved laser-induced luminescence spectroscopy (TRLFS) was used to study the aqueous U(VI) speciation in (hyper)alkaline solutions. A development of this technique, enabling site-selectivity, was used to directly investigate the sorbed U(VI) complexes on the mineral surfaces. Extended X-ray absorption fine structure (EXAFS) spectroscopy was conducted to

further clarify the underlying retention mechanisms and to provide information about the local U(VI) coordination environment of retained species. In addition to these techniques operating at sub-micromolar U(VI) concentrations, *in situ* ATR FT-IR and CTR/RAXR gave further insight into the processes at the solid/solution interface at higher U(VI) concentrations.

1.3. Radioactive waste disposal in Germany

As a reaction to the nuclear accident in Fukushima, in 2011 the German Bundestag passed a law, regulating a nuclear phase out until the year 2022. Notwithstanding, the final disposal of existing radioactive waste from power plants, military, industrial and medical applications is still a problem to be solved. According to predictions by the Federal Ministry of the Environment, Nature Conservation and Nuclear Safety (BMU), until the year 2080 approx. 10,500 tons of high-level radioactive waste from nuclear power plants will have accumulated. Additionally, approx. 600,000 m^3 of low and intermediate-level waste will have to be disposed (BMU, 2015). Among scientists and policy makers, it is international consensus to store radioactive waste in deep geological formations. While there are already dedicated sites for low- and intermediate level radioactive waste in Germany (Konrad, Morsleben), the search for a repository for high level radioactive waste has just begun and is regulated by the 'Gesetz zur Suche und Auswahl eines Standortes für ein Endlager für hochradioaktive Abfälle' (StandAG), which was enacted in 2013. Potential host rocks for a deep geological repository are rock salt, claystone and crystalline rock (BGR, 2007). All three rock types have advantages and disadvantages, and a decision based on scientific criteria requires careful evaluation. Irrespective of the selected site and host rock, the disposal will be realized according to a multi barrier concept, where the radionuclides are confined by an engineered barrier (waste container), a geo-engineered barrier (buffer, borehole sealing, backfill material) and, finally, the geological barrier (host rock). According to this model, clay minerals might contact and retard radionuclides in the geological barrier as well as in the geo-engineered barrier where bentonite is considered as backfill material.

The considerations of this thesis (embedded in the BMWi project *GRaZ* (No. 02 E 11415B)) base on the framework of the *AnSichT* project, where the feasibility of a repository in German clay formation is evaluated (Jobmann *et al.*, 2017). According to the developed site model 'NORD', Ca-bentonite will be used in the geo-engineered barrier as buffer material and borehole sealing. Concrete will be emplaced at different places within the repository for sealing and stabilization (Lommerzheim and Jobmann, 2014). A schematic sketch of a reposition borehole is depicted in Figure 2. Water ingress into the repository is regarded as a worst case scenario which could result in the mobilization of radionuclides. Pore waters in cretaceous clay formations in the North German Basin at repository depth (~800 m) are characterized by exceptionally high ionic strengths (Brewitz, 1982), with salinities of approx. 150 g/L (Wolfgramm *et al.*, 2011; Jahn and Sönnke, 2013; Nowak and Maßmann, 2013). These high salinities lead to an enhanced degradation of concrete upon water ingress and thus

promote the formation of (hyper)alkaline cement pore waters (Berner, 1992). As a consequence, (hyper)alkaline conditions can prevail in deep geological repository environments for 10^5 years (Van Loon *et al.*, 1997). Next to the high pH, a number of different ions are contained in the pore water, which can influence the retention potential of mineral surfaces toward radionuclides. Carbonate concentrations in the pore waters of North German clay formations are in the range of 1 mM – 0.1 M (Wolfgramm *et al.*, 2011). Organic molecules such as isosaccharinic acid (ISA), which is a cellulose degradation product, can be released from radioactive waste. Both carbonate and ISA can act as ligands for radionuclides, leading to the formation of highly soluble and mobile radionuclide complexes. Another complexing or competing ion is Ca^{2+} which is also ubiquitous in geological environments. For a realistic safety assessment of deep geological repositories, these complex chemical conditions of natural systems have to be considered in laboratory experiments and modelling.

Even though the chemical conditions in the experiments of this thesis were chosen to specifically simulate those within North German clay formations, very similar conditions can be found elsewhere, so that the results are highly transferable and of significant relevance for almost all other disposal scenarios. Highly saline pore waters are prevailing for instance in Japanese clay rocks and Canadian limestones, which are also considered as potential host rocks (Mazurek, 2004; Hama *et al.*, 2007). Countries where both cement and clay (either as backfill material or host rock) are part of the disposal concept are for example France, Switzerland, Finland, USA, Great Britain and Japan (Nagra, 2002; Vuorinen *et al.*, 2006; ANDRA, 2013; NUMO, 2013; U.S.NRC, 2014; RWM, 2017).
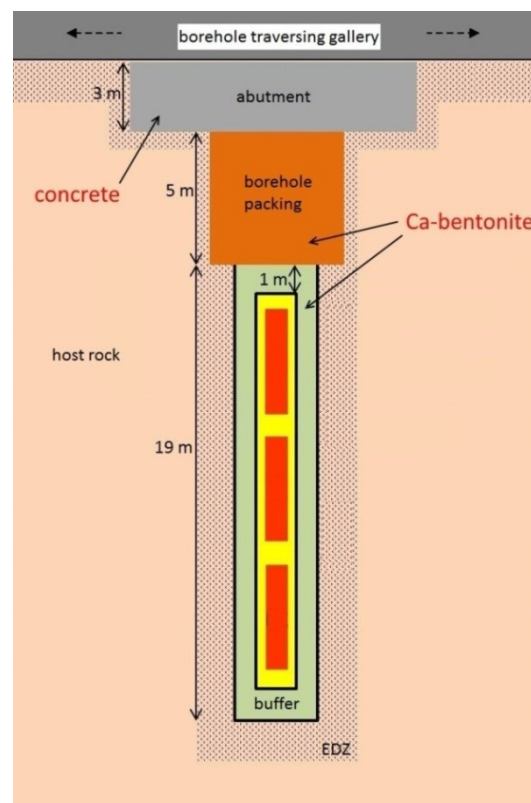
Figure 2: Schematic sketch of a repository borehole after the AnSichT project (Lommerzheim and Jobmann, 2014)

2. Theoretical Background

2.1. Chemistry of uranium and neptunium

Uranium is an actinide (5f element) and features the electronic configuration $[Rn]5f^3 6d^1 7s^2$ (Kratz and Lieser, 2013). Like all actinides, uranium has only radioactive isotopes of which three are naturally occurring. Those are ^{238}U, ^{235}U and ^{234}U. ^{238}U is the predominant isotope in natural uranium (99.274%) and is the parent nuclide of the radium decay series. With a half-life of 4.47×10^9 years it decays by alpha decay to ^{234}Th. The second most abundant natural uranium isotope is ^{235}U (0.720%), which is the parent nuclide of the actinium decay series. By alpha decay and with a half-life of 7.04×10^8 years it decays to ^{231}Th. Both, ^{238}U and ^{235}U are primordial nuclides. This is not the case for ^{234}U (0.005%) which is a daughter nuclide of ^{238}U. With a half-life of 2.46×10^5 years it decays, also by alpha decay, to ^{230}Th. Besides the naturally occurring isotopes, ^{233}U is important, as it is used in nuclear reactors. It is produced by neutron capture of ^{232}Th, forming ^{233}Th. ^{233}Th then first decays to ^{233}Pa and finally to ^{233}U, both by beta-decay. ^{233}U itself has a half-life of 1.59×10^5 years and decays (alpha-decay) to ^{229}Th (Lieser, 1991).

As for most of the early actinides, the redox chemistry of uranium is rather complex. It occurs in the oxidation states +3 to +6 (Choppin *et al.*, 1995; Cotton, 2006), depending on the redox potential (Eh) and the pH (Figure 3). While, under acidic conditions, uranium in the tetravalent oxidation state appears as a simple hydrated ion U^{4+}, the higher oxidation states form oxycations, called uranyl ions, $U^V O_2^+$ and $U^{VI} O_2^{2+}$. The most important oxidation states are +4 and +6, as U(III) is unstable under most conditions and oxidizes easily to U(IV) and U(V) disproportionates easily to U(IV) and U(VI). U(IV) is stable under reducing conditions and is relatively insoluble and therefore immobile. U(VI) is the most prominent oxidation state in ocean and groundwater environments as it is stable under oxidizing conditions. It is more soluble and consequently more mobile than U(IV) (Silva and Nitsche, 1995).
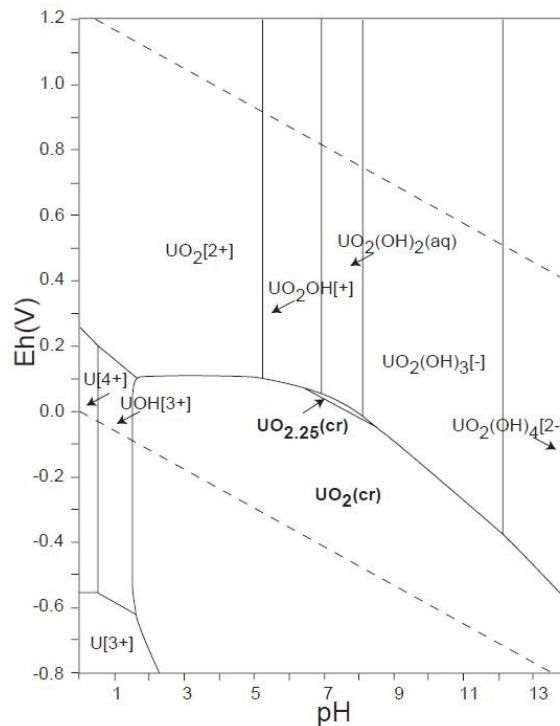
Figure 3: Predominance diagram of the system U-O-H, showing the complexity of the redox chemistry of uranium (1×10^{-10} mole/kg), based on the OECD-NEA database (Takeno, 2005).

The mobility of uranium is not only controlled by the oxidation state but also by its speciation. In case of water ingress into the repository, uranium can be mobilized by forming soluble species with the surrounding ions. Most common coordination numbers are 6, 7 and 8 but 2, 4, 9, and 12 can also occur (Cotton, 2006). In the hexavalent oxidation state, uranium is almost exclusively found in the form of a cationic oxide UO_2^{2+}. The angle of the O=U=O bond is usually 180° and ligands are arranged in the equatorial plane, perpendicular to the linear axis of the yl-bond (Figure 4). Uranyl ions are 'hard' Lewis acids and preferentially form strong complexes with 'hard' ligands, such as carbonate and hydroxide, but also with halogens, phosphates or sulfates. The axial and equatorial coordination determines the vibronic and electronic properties of the uranium compounds, which are characteristic and can be investigated with spectroscopic techniques. Implications for U(VI) luminescence spectroscopy are explained in chapter 2.5.1.
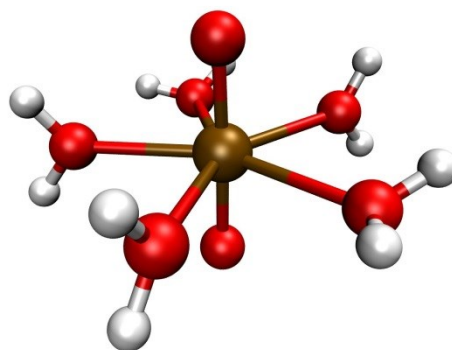
Figure 4: Uranyl(VI) aquo ion coordinated by five water molecules in the equatorial plane (UO$_2$(H$_2$O)$_5^{2+}$).

In the acidic, neutral and slightly alkaline pH region, the aqueous speciation of U(VI) is well understood. At low pH (up to pH 4) the un-complexed uranyl aquo ion is the only relevant species. At higher pH, speciation of U(VI) in aqueous solution is controlled by hydrolysis reactions and carbonate complexation with a strong dependence on the concentration of dissolved carbonate, U(VI)-concentration and pH (Guillaumont *et al.*, 2003). In the absence of CO_2 strong hydrolysis is the dominant process (Figure 5a). At micromolar UO_2^{2+} concentrations, monomeric hydroxo species are expected, while at higher concentration polymeric species are formed. In case that a sufficient amount of carbonate is available, U(VI) complexation with carbonate occurs at pH > 6 (Figure 5b), which significantly increases U(VI) solubility and lowers U(VI) sorption. In natural groundwaters also highly mobile calcium uranyl carbonate complexes have been identified (Bernhard *et al.*, 2001). Only few data is available on the U(VI) speciation at (hyper)alkaline conditions. The speciation modelling presented in Figure 5 has been performed up to pH 13 based on the PSI/Nagra Chemical Thermodynamic Database. However the contained data are not very reliable at the extreme conditions investigated in this thesis, being very high pH and elevated ionic strength (diluted Gipshut solution). Therefore calculations were performed for 0.1 M NaCl as background electrolyte. In the absence of carbonate, the aqueous U(VI) speciation is dominated by $UO_2(OH)_3^-$ and $UO_2(OH)_4^{2-}$ at pH > 10 and pH > 12, respectively. In the presence of 1×10^{-3} M carbonate uranyl carbonate complexes are predicted to prevail only up to pH 10.5. At higher pH hydrolysis is thermodynamically favored compared to complexation with carbonate, so that the same species are expected as in the absence of carbonate. This competition between hydrolysis and complexation with carbonate has not been investigated systematically over a wide alkaline pH range. In order to check the validity of the modelling results also for the system with diluted Gipshut solution, in this thesis the aqueous U(VI) speciation was investigated with luminescence spectroscopy (chapter 4.2.2).
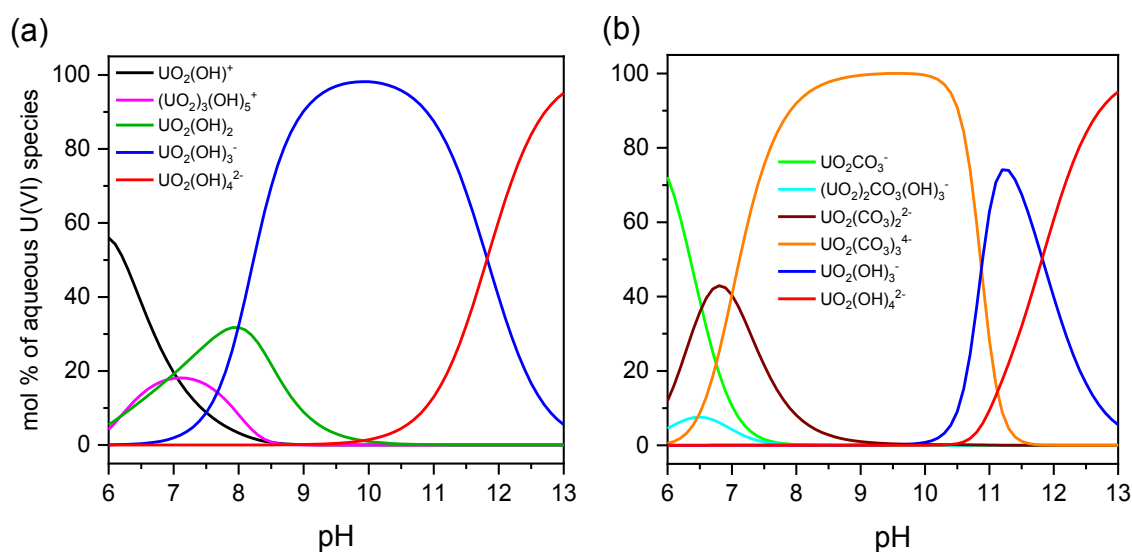
Figure 5: Aqueous speciation of U(VI) (5×10^{-7} M) in 0.1 M NaCl in the absence of CO_2 (a) and at $[CO_3^{2-}]$ of 1×10^{-3} M (b) calculated with the geochemical modelling software PHREEQC (Parkhurst and Appelo, 2013) and based on thermodynamic data of the PSI/Nagra Chemical Thermodynamic Database 12/07(Thoenen et al., 2014).

Neptunium, also belonging to the actinides (5f-elements), is the first transuranic element and features the electronic configuration $[Rn]5f^4 6d^1 7s^2$ (Kratz and Lieser, 2013). It is not primordial (due to the short half-life compared to the age of the earth) but occurs naturally in trace amounts (^{237}Np and ^{239}Np) due to neutron capture of uranium and following beta decay. The most abundant and longest-lived isotope ^{237}Np (half-life of 2.14×10^6 years) is a by-product in nuclear reactors (originating from ^{235}U and ^{238}U) and decays by alpha decay to ^{233}Pa. ^{239}Np can be synthesized by neutron irradiation. Owing to its short half-life of 2.356 days it is very useful as a radioactive tracer (Morss *et al.*, 2006).

As for uranium, the redox chemistry of neptunium is very complex. It exists in the oxidation states +3 to +7 (Choppin *et al.*, 1995; Cotton, 2006), of wich +4, +5 and +6 are environmentally relevant (see Figure 50). While Np(IV) is stable under reducing conditions, Np(V) is the most stable oxidation state at oxidizing conditions. Np(VI) can also be stable under oxidizing conditions, but is easily reduced to Np(V) (Kaszuba and Runde, 1999; Morss *et al.*, 2006). Nevertheless, according to recent considerations at alkaline conditions the stability field of Np(V) may be significantly limited in favor of Np(VI) (Gaona *et al.*, 2012; Tits *et al.*, 2014). In analogy to uranyl, in the pentavalent and hexavalent oxidation state neptunium is present as linearly arranged neptunyl $Np^{V}O_2^{+}$ and $Np^{VI}O_2^{2+}$, respectively. At low pH the fully hydrated neptunyl ion is the predominant aqueous species. For Np(VI) the aqueous speciation is very similar to the one of U(VI), with neptunyl hydroxide complexes prevailing at pH > 4 in the absence of CO_2 and the formation of neptunyl carbonate complexes in the presence of carbonate (Guillaumont *et al.*, 2003). The modeled Np(VI) speciation at the conditions of the performed Np(VI) sorption experiment on muscovite in the absence of CO_2 is shown in Figure Appendix 1. In the pH range of interest in this thesis (8-13) the speciation is controlled by the anionic neptunyl hydroxide species $NpO_2(OH)_3^{-}$ and $NpO_2(OH)_4^{2-}$ (Thoenen *et al.*, 2014). Due to the similarities in aqueous speciation of U(VI) and Np(VI) at alkaline conditions, comparison of sorption behavior is interesting and was pursued within this thesis.

A release of uranium and neptunium to the biosphere has to be avoided since they are both radiotoxic and chemotoxic. Both are contained in spent nuclear fuel and will be disposed in a deep geological repository. Even though natural uranium is a comparably weak radiological threat (due to its low specific activity) it poses a severe cell destroying threat in case that it is incorporated (Bleise *et al.*, 2003). Moreover, by featuring heavy metal properties, uranium is chemically toxic being able to destroy the function of organs such as liver or heart (Choppin *et al.*, 1995).

2.2. Clay mineralogy, bentonite, montmorillonite and muscovite

The term 'clay' is has several meanings. It can stand for a particle size fraction (smaller than silt) irrespective of mineralogy, but also for a group of silicate minerals, classified as clay minerals. Moreover, clay is also defined as a multi-mineral rock type of sedimentary origin that mainly consists of clay minerals (< 2 μm). In the following section the structure and properties of clay minerals will be presented. Special focus is on the clay mineral montmorillonite, as it is the main constituent of the clay rock bentonite. Furthermore kaolinite and the mica mineral muscovite, featuring a clay mineral like structure, are introduced as these were used as model minerals in several batch sorption experiments within this work.

In general, clay minerals are water-bearing aluminum silicates with a layered structure. They are composed of sets of $[SiO_4]$-tetrahedra and $[M(O,OH)_6]$-octahedra ($M = Al^{3+}$, Fe^{3+}, Fe^{2+} or Mg^{2+}). The tetrahedra ('T' in Figure 6) are combined to form a layered network to which a layer of octahedra ('O' in Figure 6) is condensed via the octahedra edges. Consequently, oxygen ions of the tetrahedra are at the same time part of the octahedra. Oxygen ions of the octahedra layers which do not belong to a tetrahedron, are binding a proton, forming hydroxide (OH^-) ions. This arrangement is repetitively stacked to form layered silicate clay minerals. Different types of clay minerals can be distinguished by the occupation of their layers with cations and anions and the sequence and connection of those. In case a unit is composed of one tetrahedral and one octahedral layer, the mineral is defined as 1:1 layer silicate (two sheet silicate) (Figure 6a). The most prominent 1:1 clay mineral is kaolinite ($Al_4[(OH)_8|Si_4O_{10}]$). Its units are uncharged and are held together by dipole-dipole interactions, hydrogen bonds and van der Waals forces. Kaolinite is not swellable, fixing the distance between the units (d_L in Figure 6) to 7.0-7.3 Å (Jasmund and Lagaly, 1993). 2:1 layer silicates (three sheet silicates) refer to minerals in which an additional tetrahedral layer is bound to the octahedral layer (the octahedral layer is enclosed) (Figure 6b). In the case of talk or pyrophyllite those units are also uncharged. In many 2:1 clay minerals, however, the units are negatively charged, mostly due to substitution processes. Trivalent central ions in the octahedra (i.e. Al^{3+}) can be replaced by divalent ions (e.g. Mg^{2+}), or analogously, divalent by monovalent ions. Also Si^{4+} in the tetrahedra can be replaced by Al^{3+}. In order to compensate the charge, interlayer cations (such as K^+ or Ca^{2+}) are incorporated into the structure. The distance between the units (d_L) is approximately 10 Å. Additionally, water molecules can be present in the interlayers, further increasing d_L. Examples for 2:1 clay minerals are illite and smectite. Montmorillonite ($(Na,Ca)_{0,3}(Al,Mg)_2Si_4O_{10}(OH)_2 \cdot nH_2O$), the main constituent of bentonite, is the most prevalent smectite mineral. It is very swellable and has the ability to very effectively bind cations and liquids in their interlayers. Due to this ability, the spacing between the layers in the crystallographic c-direction can vary strongly. In montmorillonite Al^{3+} is substituted by Mg^{2+}, causing a permanent negative surface charge (Jasmund and Lagaly, 1993).
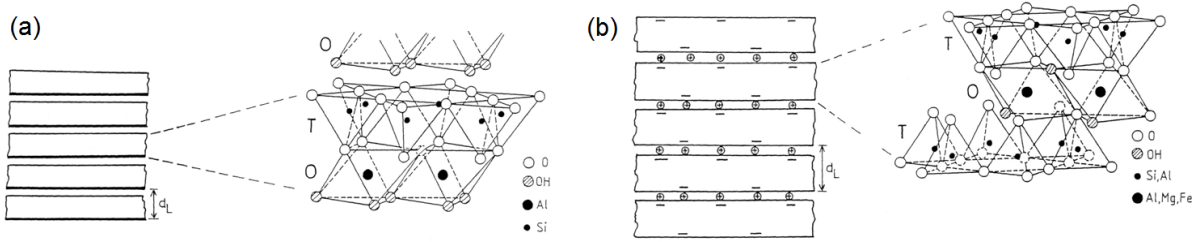
Figure 6: (a) Structure of 1:1 layer silicates (two sheet clay minerals) consisting of units of one octahedral layer and one tetrahedral layer. The uncharged units are held together by dipole-dipole interactions, hydrogen bonds and van der Waals forces. (b) Structure of 2:1 layer silicates (three sheet clay minerals) with an octahedral layer framed by two tetrahedral layers. The negatively charged units are stacked, containing interlayer ions for charge compensation Modified after Jasmund and Lagaly (1993).

As a result of the characteristic structure, clay minerals feature a number of specific properties that qualify them as barrier/sealing units. Due to their high swelling capacity, thixotropy, plasticity and nano-scale pore structure their permeability is extremely low. Furthermore, clays feature a pronounced sorption capacity regarding heavy metals, caused by the large specific surface area, high cation exchange capacity and availability of surface complexation sites (Heim, 1990). Since montmorillonite combines many of those favorable characteristics (e.g. high specific surface area and high swelling capacity), bentonite is considered as buffer and backfill material in deep geological repositories for radioactive waste. Bentonite is defined as rock that mainly consists of smectite (i.e. montmorillonite) (Hiltmann and Stribrny, 1998). Additionally it can contain variable amounts of illite, kaolinite, chlorite, quartz, feldspars and carbonate minerals. It occurs naturally as in situ degradation product of volcanic ash (Jasmund and Lagaly, 1993) and can be subdivided into Na-bentonite and Ca-bentonite, depending on the montmorillonite interlayer cations.

The mica mineral muscovite ($KAl_2[(OH,F)_2|AlSi_3O_{10}]$) is a precursor of clay minerals. Exhibiting no swelling capacity, the units of the 2:1 sheet silicate are weakly held together by large interlayer cations (conventionally potassium), causing perfect basal cleavage. Due to the strong structural similarity to clay minerals, muscovite can be regarded as a clay mineral analogue. In this work it was used as calcium-free model mineral for montmorillonite.

2.3. Sorption mechanisms

The mobility of radionuclides in the geosphere is considerably influenced by their interaction with solids (Kratz and Lieser, 2013). Owing to different types of processes at the solid-water interface, migration can be retarded or inhibited. Therefore a fundamental understanding of retardation processes is crucial for the long-term safety assessment of a deep-geological repository for high-level radioactive waste. Such processes, by which dissolved ions or molecules are attached to a mineral surface (i.e. are transferred from the liquid to the solid phase) are referred to as sorption (Ościk, 1982). The solid phase is termed sorbent and the metal ion that can be adsorbed is termed sorptive. The adsorbed species is referred to as sorbate. Sorption is a generic term. Beside precipitation and ion exchange it encompasses

adsorption and incorporation (Appelo and Postma, 1994). Incorporation of a substance into the crystal lattice of another can be realized by co-precipitation or by diffusive migration accompanied by a replacement in the lattice. These mechanisms can yield so called 'solid-solutions' in which the sorptive (i.e. radionuclide) is bound very strongly. It is the most effective and stable form of retardation. The process of adsorption is further subdivided into chemical adsorption (chemisorption) and physical adsorption (physisorption), depending on whether a chemical (ionic or covalent) bond is formed between the metal and the electron donating surface ions, or if a cation of opposite charge approaches the surface groups with a critical distance, separated by water molecules (Stumm, 1992). Electrical interactions with the surface (electrostatic interactions, polarization interactions) lead to the formation of so-called outer-sphere complexes. The fully hydrated ion is not bound directly to the mineral surface and attaches only weakly (e.g. by van der Waals forces). The formation of such electrostatically bound outer-sphere complexes is strongly dependent on the ionic strength (I). Changes in I can lead to an immediate remobilization. Chemical reactions with surfaces (surface hydrolysis, surface complexation, surface ligand exchange and hydrogen bond formation) lead to the formation of so-called inner-sphere complexes. Here the ion/molecule (i.e. radionuclide), which has lost parts of its hydration shell, is interacting directly via the inner coordination sphere in the form of strong covalent (sometimes ionic) bonding (Dekov *et al.*, 2007). Inner-sphere complexes are therefore much more stable than outer-sphere complexes. Remobilization requires a strong change in the pH of the surrounding solution. The different types of interactions at the solid-water interface are summarized in Figure 7. In order to determine the exact mechanism by which a certain contaminant is bound to the surface, one can apply spectroscopic techniques such as luminescence spectroscopy (TRLFS), vibrational spectroscopy (IR, Raman), X-ray absorption spectroscopy (XANES, EXAFS), resonance spectroscopy (NMR, ESR), X-ray diffraction (XRD) and X-ray reflectivity (CTR/RAXR).
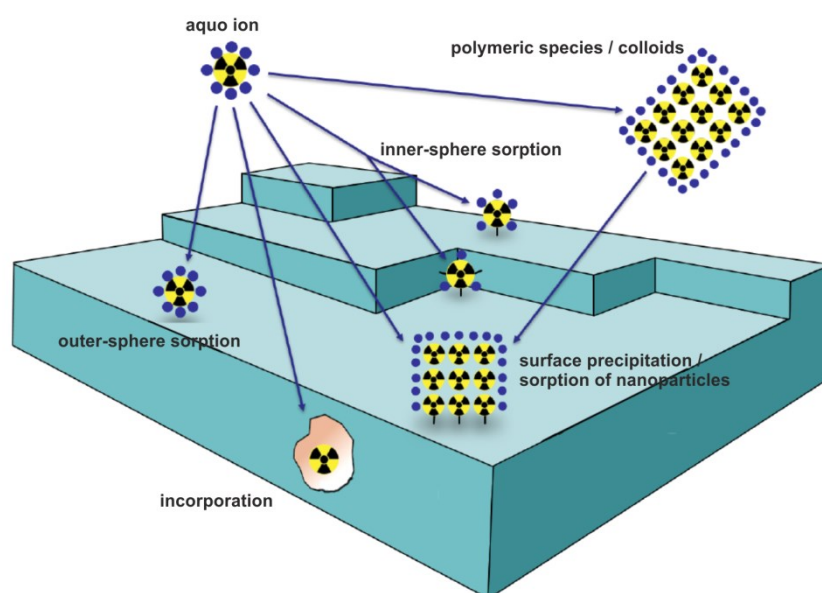
Figure 7: Possible interaction of radionuclides with a mineral surface (modified after Manceau et al. (2002)).

Surface complexation can be described by chemical reactions between dissolved species and mineral surface binding sites, whereby sorbed surface species evolve. Reactions of hydroxo complexes or ionic forms of metals M (i.e. radionuclides) with hydroxyl groups at the surface (S) of solids (such as $\equiv$SiOH, =AlOH or =FeOH) are frequently observed (Stumm, 1992; Kratz and Lieser, 2013):

$$S - OH(s) + HO - M \ \leftrightarrow \ \equiv S - O - M(s) + H_2O \tag{1}$$
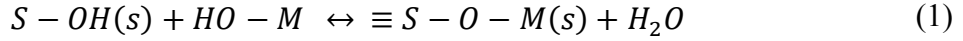
This type of reaction is referred to as hydrolytic adsorption and can lead to mono- or multidentate surface complexes. Such complexation is strongly dependent on the pH. At higher pH, the surface hydroxyls tend to be more easily deprotonated, leading to rise of sorption (pH-edge). Formulating equations like equation (1) as mass laws, stability constants (β) of certain complexes can be deduced which serve as input data for surface complexation modelling (SCM) (Stumm, 1992).

Tools to describe and quantify sorption are sorption isotherms and the distribution coefficient K_d. Considering the reaction S + M $\leftrightarrow$ SM, the distribution coefficient is defined as the ratio of the sorbed species (SM) and the species remaining in solution (M) (Stumm, 1992).

$$K_d = \frac{[SM]}{[S][M]} \tag{2}$$

From sorption experiments the initial (c_0) and the equilibrium (c_{eq}) metal concentration [M] are known so that the K_d can be calculated as

$$K_d = \frac{c_0 - c_{eq}}{c_{eq}} \times \frac{V}{m} \tag{3}$$

where V [L] is the volume of the solution and m [kg] the mass of the solid. K_d values strongly depend on the experimental conditions (pH, ionic strength, metal concentration, temperature, present ligands, competing ions) and are therefore not applicable for extrapolation. The dependence of sorption on the metal concentration can be expressed with sorption isotherms. If the amount of substance sorbed on the solid in equilibrium a_{eq} is linearly dependent on the equilibrium concentration of substance in the solution c_{eq}, sorption can be described by the linear Henry isotherm (Henry, 1803) (equation (4)).

$$a_{eq} = K_d \times c_{eq} \tag{4}$$

In natural systems, however, sorption mechanisms are quite complex, which calls for more sophisticated sorption isotherms, considering more parameters. The most commonly used isotherms are the Freundlich and the Langmuir isotherm. The Freundlich isotherm (equation (5)) considers interactions between the sorptive and ions that have already been adsorbed. The

more ions/molecules are already adsorbed, the lower is the chance that additional sorption can take place.

$$a_{eq} = K_F \times c_{eq}^{n_F} \tag{5}$$

K_F is the Freundlich coefficient [m^3/kg] and n_F is the Freundlich exponent [-] with n < 1 (Stumm, 1992). The Langmuir isotherm (equation (6)) takes into account that there is saturation at the surface due to limited sorption sites by adding the parameter a_m, representing the maximum amount of substance that can be sorbed onto the solid. b is the Langmuir sorption coefficient (Langmuir, 1918).

$$a_{eq} = \frac{a_m \times b \times c_{eq}}{1 + b \times c_{eq}} \tag{6}$$

2.4. U(VI) and Np(VI) sorption on clay minerals – state of knowledge

Clay minerals are known for their high retardation capability due to their properties described in chapter 2.2. Thus, in natural rocks (such as bentonite), clay minerals act as the major sorbents for actinides (Hartmann *et al.*, 2008). Different interaction mechanisms between actinides in solution and clay mineral surfaces are possible. Ions can interact with clay minerals at the basal surfaces as well as at the edge surfaces. Another possibility is ion exchange in the interlayers (Figure 8). As described in chapter 2.2, the external basal surfaces (001) are formed by tetrahedral sheets with a permanent negative, pH-independent charge. Sorption of metal ions at these charged sites takes place by exchange of bound cations and is determined by electrostatic interaction. This mechanism corresponds to outer-sphere complexation. On the other hand, the edge surfaces of clay minerals consist of interrupted Si–O, R^{2+}–OH, or R^{3+}–OH bonds with variable, pH-dependent charge. Protonation of the sites at low pH leads to Lewis acids, deprotonation at high pH to Lewis bases. By chemical bonding with those aluminol and silanol groups, inner-sphere complexes are formed (Figure 8).
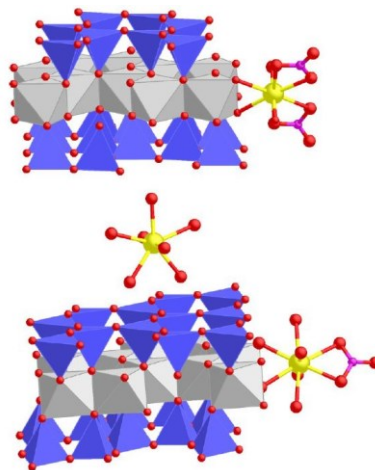
Figure 8: Uranyl sorption in the interlayers and at the edge sites of montmorillonite. Adopted from Maher et al. (2013).

The retardation of U(VI) in montmorillonite/bentonite is highly dependent on key solution parameters, such as the pH, ionic strength and presence or absence of CO_2 and has been investigated in various studies (Akcay, 1998; Chisholm-Brause *et al.*, 2004; Bradbury and Baeyens, 2005; Catalano and Brown, 2005; Bachmaf *et al.*, 2008; Meleshyn *et al.*, 2009; Ivanov *et al.*, 2012; Marques Fernandes *et al.*, 2012; Verma *et al.*, 2015; Tournassat *et al.*, 2018). From these studies, a general sorption behavior can be deduced. Under acidic conditions (pH < 5) and low ionic strengths, the uranyl, present as fully solvated ion, binds via cation exchange. The overall uptake under these conditions is low (Maher *et al.*, 2013). As the pH increases to the near-neutral range, various U(VI) hydrolysis complexes dominate the solution speciation, which further can form inner-sphere sorption complexes at the deprotonated montmorillonite edge sites (silanol and/or aluminol groups), resulting in a quantitative uptake of uranium by the clay mineral (Stumm, 1992; Maher *et al.*, 2013). The U(VI) surface speciation investigated in EXAFS measurements confirmed a splitting of the equatorial oxygen shell of uranyl at circumneutral pH and backscattering contributions from substrate atoms (Si/Al, Fe), indicative of inner-sphere complexation. Shell fitting suggested bidentate coordination to aluminum octahedra and/or silicon tetrahedra (Chisholm-Brause *et al.*, 1994; Sylwester *et al.*, 2000; Hennig *et al.*, 2002; Chisholm-Brause *et al.*, 2004; Catalano and Brown, 2005; Marques Fernandes *et al.*, 2012). In the absence of carbonate, the sorption maximum is maintained also at higher pH (Figure 9). However, in the presence of CO_2, sorption decreases drastically at pH > 6 due to the formation of aqueous uranyl carbonate complexes. These complexes are extremely stable in solution (Guillaumont *et al.*, 2003) and have a low tendency to attach to mineral surfaces (Marques Fernandes *et al.*, 2012; Maher *et al.*, 2013; Richter, 2015; Fritsch, 2018; Tournassat *et al.*, 2018) (Figure 9).
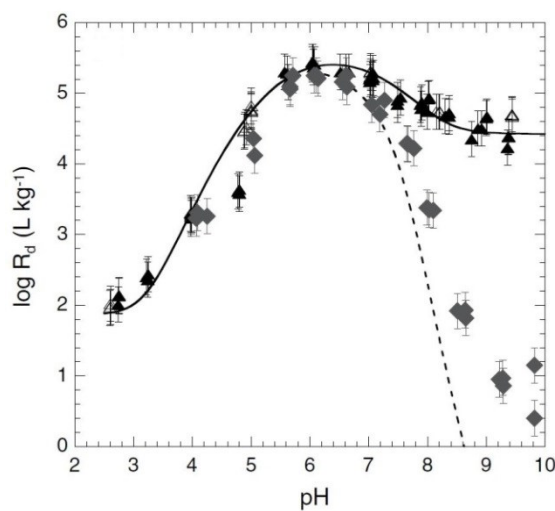
Figure 9: U(VI) sorption edge on montmorillonite in the absence of CO_2 (triangles) and with atmospheric pCO_2 (diamonds), exemplarily showing the sorption trend found in many studies up to pH 10 (adopted from Marques Fernandes et al. (2012)).

Nevertheless, modelling by Marques Fernandes *et al.* (2012) suggested that uranyl carbonate complexes sorb at least to some extent to montmorillonite surfaces and also a number of spectroscopic studies indicate the formation of ternary uranyl carbonate surface complexes on montmorillonite, silica, Hanford sediment and ferrihydrite (Wang *et al.*, 2005; Rossberg *et al.*, 2009; Troyer *et al.*, 2016; Saleh *et al.*, 2018). On the other hand, Marques Fernandes *et al.* (2012) could not provide spectroscopic evidence for the formation of such surface complexes by EXAFS. Furthermore, Tournassat *et al.* (2018) were able to model U(VI) retention behavior under a wide range of chemical conditions without the introduction of uranyl carbonate surface complexes with the help of a refined surface complexation model based on the consideration of surface charge spillover effects and precise measurements of dissolved inorganic carbon (DIC). The presence of Ca^{2+} in the solution can further modify the U(VI) retention behavior. Formation of highly soluble ternary $CaUO_2(CO_3)_3^{2-}$ and $Ca_2UO_2(CO_3)_{3(aq)}$ complexes can additionally suppress U(VI) adsorption (Bernhard *et al.*, 2001; Meleshyn *et al.*, 2009; Joseph, 2013; Schmeide *et al.*, 2014). Modelling of sorption isotherms and pH-edges has been successfully applied in order to verify the assumed surface complexation reactions. A very prominent model is the Two Site Protolysis Non-Electrostatic Surface Complexation and Cation Exchange (2SPNE SC/CE) model (Bradbury and Baeyens, 1997). This quasi-mechanistic thermodynamic model calculates the uptake of metal species by combination of cation exchange and pH-dependent inner-sphere surface complexation at the amphoteric edge sites, using hydrolysis and complexation constants of the NEA Chemical Thermodynamic Database (Guillaumont *et al.*, 2003).

Thus, the sorption of U(VI) on montmorillonite is already well understood at low ionic strength and acidic to slightly alkaline pH values. However, a huge lack of knowledge still exists concerning the extent and mechanisms of U(VI) retention in a saline, hyperalkaline regime, as it can be expected in the near-field of a concrete-containing deep geological repository for radioactive waste. In the previous BMWi-Project "Retention of radionuclides relevant for final disposal in natural clay rock and saline systems" (No.: 02 E 10971, 2011-2015) the focus was directed to the influence of high ionic strength. In batch experiments K. Fritsch found that the retention of U(VI) by montmorillonite is not significantly affected by ionic strength (up to 3 M) in the circumneutral pH region (Fritsch, 2018). The current BMWi-Project GRaZ focusses additionally on high pH, originating from the degradation of cementitious material in the repository. Almost no published studies exist about the sorption of U(VI) by clay at pH > 10. None of the studies dealing with the formation of uranyl carbonate complexes address if such complexes still prevail when further increasing the pH value. No clear upper pH boundary for their formation has been shown experimentally as a function of DIC due to increasing competition of carbonate with the hydroxyl ligand. Beside uranyl carbonates, the aqueous speciation in the pH range 8-13 is dominated by the higher hydrolysis complexes of uranyl ($UO_2(OH)_3^-$ and $UO_2(OH)_4^{2-}$) (see Figure 5a). Generally, almost no studies were published about the adsorption of U(VI) by clay at pH > 10,

describing surface complexes formed by contribution of these anionic aqueous U(VI) species. In his thesis, Andreas Schnurr (2015) quantified the U(VI) retention by illite and kaolinite up to pH 12. For both minerals almost complete sorption was maintained up to pH 11. At pH above that, a slight decrease in sorption was observed. Possible explanations for the observed retention behavior were not pursued spectroscopically. The mentioned study was performed in the absence of CO_2. To our knowledge, no U(VI) sorption study on clay minerals at (hyper)alkaline pH exists, which would additionally consider the effect of carbonate in the solution at pH 10-13. Studies concerning the U(VI) retention at hyperalkaline conditions mainly address colloid formation or precipitation processes. Generally, U(VI) solubility in (hyper)alkaline solutions is very low and (earth) alkali uranates are the solubility limiting phases (Yamamura *et al.*, 1998; Bots *et al.*, 2014; Altmaier *et al.*, 2017; Tits and Wieland, 2018). In carbonate-free NaCl solutions at pH 8-11, Altmaier *et al.* (2017) determined the U(VI) solubility, controlled by $Na_2U_2O_7 \cdot H_2O(cr)$, to be at nanomolar concentrations (*I*=2.6 M). In Ca-containing solutions, U(VI) preferentially precipitates as Ca-uranate ($CaUO_4(s)$) (Tits *et al.*, 2011; Ochs *et al.*, 2016; Tits and Wieland, 2018). Above pH 11, U(VI) solubility increases, reaching micromolar concentrations at pH 13 (Altmaier *et al.*, 2017). Kaplan *et al.* (1998) investigated the U(VI) retention by sediments up to pH 12 and observed a number of heterogeneous precipitation processes. Kenney *et al.* (2017) attributed the removal of U(VI) from the solution above pH 10 to the precipitation of uranyl carbonates. Smith *et al.* (2015) observed the formation of U(VI) colloids and surface mediated precipitation processes in hyperalkaline calcite systems in most of their experiments. Indications for the formation of U(VI) surface complexes on calcite at pH 10.5 and 13.3 were only observed at sub-micromolar U(VI) concentrations. Also Bots *et al.* (2014) observed the formation of U(VI) nanoparticles at pH > 13. Considerable research has been performed concerning the U(VI) immobilization in cementitious systems at pH > 13. U(VI) is effectively retained in calcium silicate hydrate (C-S-H) phases and hardened cement paste (Tits *et al.*, 2008; Wieland, 2014; Ochs *et al.*, 2016; Wolter *et al.*, 2019) and uptake is facilitated by the presence of dissolved calcium (Pointeau *et al.*, 2004; Tits and Wieland, 2018). Spectroscopic studies further investigated the nature of the retained U(VI) complexes. TRLFS revealed the presence of surface complexes as well as incorporated species and precipitation of Ca-uranates (Tits *et al.*, 2011; Tits *et al.*, 2015). EXAFS investigations suggest a local coordination environment similar to U(VI) silicates (such as uranophane) with a split equatorial oxygen shell and short and long silicon distances (Harfouche *et al.*, 2006; Macé *et al.*, 2013). Despite all the above mentioned findings, U(VI) sorption in (hyper)alkaline systems is still poorly understood as the existing studies provide only insight at very specific conditions (pH, carbonate concentration, etc.), with sometimes contradictory results, often lacking information on the molecular level.

While retention of Np(V) has been extensively studied, published data about Np(VI) sorption on clay minerals is non-existent. The sorption edge of Np(V) is considerably shifted to higher

pH, compared to U(VI). At low to neutral pH, Np(V) retention is low and dominated by ion exchange. Increasing sorption between pH 6 and 10 is caused by a successive deprotonation of surface groups. This results in surface complexation of the neptunyl aquo ion NpO_2^+, dominating the aqueous Np(V) speciation up to pH 10, and the hydrolyzed species $NpO_2(OH)_{aq}$ at higher pH (Bradbury and Baeyens, 2005; Schmeide and Bernhard, 2010; Amayri *et al.*, 2011; Kasar *et al.*, 2014; Elo *et al.*, 2017; Semenkova *et al.*, 2018). For Np(VI) only one sorption study exists, dealing with retention on TiO_2 and CSH at pH 10-14 (Tits *et al.*, 2014). The authors observed high sorption at pH 10 and a decrease of sorption with increasing pH. Additionally they found a positive correlation between calcium concentration and distribution ratio R_d at pH 12, 13.3 and 14. The solubility of Np(VI) at alkaline conditions was studied by Gaona *et al.* (2013) and Fellhauer *et al.* (2017). In NaCl solutions ($I = 0.1\text{-}5.0$ M) the solubility at pH 9-10.5 lies between 1×10^{-8} and 1×10^{-7} M. In analogy to U(VI), the solubility limiting phase at these conditions is $Na_2Np_2O_7(cr)$ (Gaona *et al.*, 2013). In $CaCl_2$ solutions ($I = 0.25\text{-}4.5$ M) at pH 8-12 the Np(VI) solubility lies between 1×10^{-7} and 1×10^{-6} M and is controlled by non-stoichiometric calcium neptunates $Ca_xNpO_{3+x}(s,hyd)$.

2.5. Fundamentals of spectroscopic techniques

2.5.1. Time-resolved laser-induced luminsescence spectroscopy (TRLFS)

Time-resolved laser-induced luminsescence spectroscopy (TRLFS) is a powerful technique to distinguish different U(VI) complexes at trace level concentrations through spectral changes induced by the ligand field (Moulin *et al.*, 1998). Luminescence is defined as the emission of light from a substance after previous excitation. By absorption of light (e.g. laser) electrons are excited from the ground state (S_0) to a higher energy state (S_1, S_2... S_n) or to higher vibrational states of those. Generally, possible energy levels of the electron are given by the different electronic-, vibrational- and rotational states, it can adopt. Between those energetic states, different types of electronic transitions are possible (Lakowicz, 2006), summarized in Figure 10. Radiationless relaxation accompanied with a change in electronic state (e.g. $S_2 \rightarrow S_1$), are referred to as internal conversion (IC). Radiationless relaxation from higher vibrational states of an excited state to the lowest energetic level of the respective excited state (VR) can occur. This happens due to collisions with other atoms or molecules, leading to an energy transfer. From the lowest energetic level of an excited state, a transition to the ground state ($S_1 \rightarrow S_0$) can occur by the release of the excess energy in the form of a photon (fluorescence) (Lakowicz, 2006; Steudtner, 2010; Drobot, 2016). The energy and lifetime of the luminescence is indicative for the chemical compound. Upon relaxation to the lowest excited state, also the spin multiplicity can change from a singlet to a triplet state ($S_1 \rightarrow T_1$). This is called intersystem crossing (ISC). The transition from this triple state to the ground state upon emission of a photon ($T_1 \rightarrow S_0$) is defined as phosphorescence (Lewis and Kasha, 1944).
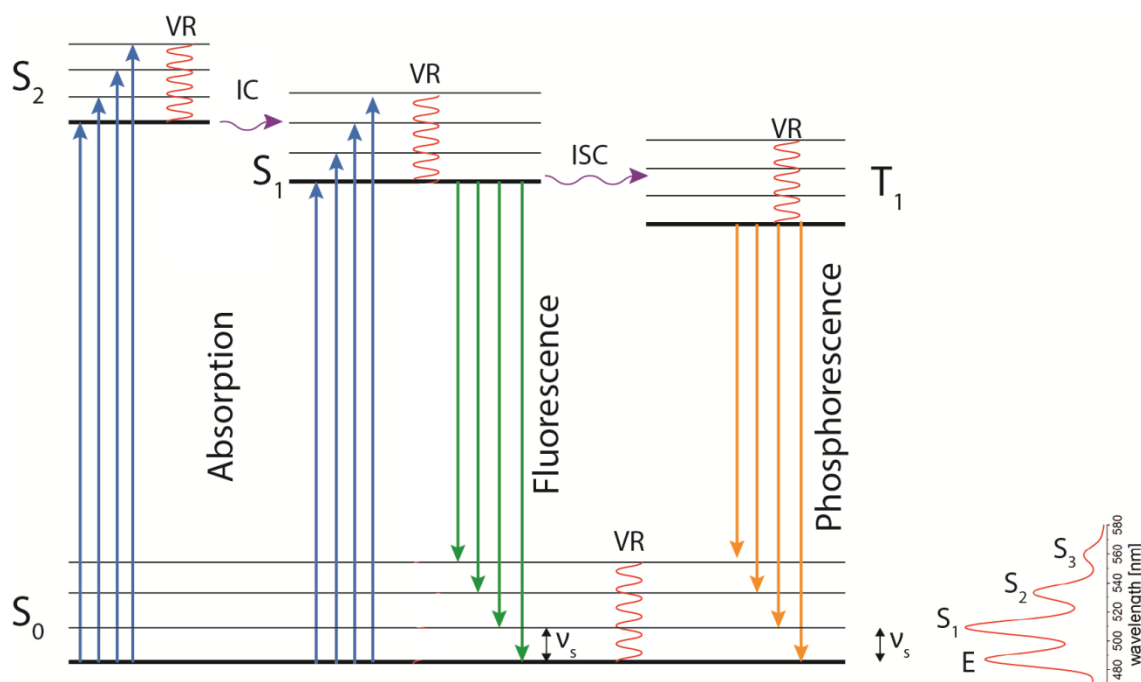
Figure 10: Jablonski diagram, schematically showing different energetic states which the electrons can adopt and the possible transitions between these states.

For lanthanides, the electronic transitions leading to luminescence are attributed to f-electrons. However, U(VI) formally does not possess any f-electrons. Since U(VI) occurs in combination with oxygen as '–yl-ion', molecular orbitals have to be considered instead of atomic orbitals (Denning, 2007). Figure 11 shows the molecular orbitals and their relative energy levels of uranyl, resulting from the overlap of the atomic orbitals 6s, 6p, 5f, 6d, and 7s of uranium and 2s and 2p of oxygen. The highest occupied molecular orbitals are $1\pi_g$, $2\pi_u$, $3\sigma_g$ and $3\sigma_u$, since they have a strong contribution from the 2p orbital of oxygen (Denning, 2007; Drobot, 2016). The $3\sigma_u$ orbital does not only form as an overlap of the 2p oxygen orbital and the 5f uranium orbital, but also involves the 6p uranium orbital. This leads to a significant rise in energy, making the $3\sigma_u$ orbital to the highest occupied molecular orbital (HOMO). The lowest unoccupied molecular orbital (LUMO) is $1\phi_u$, which is dominated by the 5f uranium orbital (Pierloot and van Besien, 2005; Denning, 2007). Therefore the lowest excitation energy is needed for the transition $3\sigma_u \rightarrow 1\phi_u$. As this transition stands for a transfer of electronic charges from oxygen- (2p) to uranium dominated orbitals (5f), it is denoted as 'charge transfer' (CT). The reversion of the CT then results into luminescence. Transitions to the lowest vibrational level of the degenerated ground state (electronic transition line E) and to higher vibronic levels of the electronic ground state (lines of vibronic progression S_1, S_2, etc.) are possible, leading to independent maxima in the uranyl emission spectra (470, 488, 509, 533, 559, 585 nm for the uranyl aquo ion) (Bell and Biggers, 1968; Tan *et al.*, 2010) (bottom right in Figure 10). The degeneration is a result of the symmetric stretching vibration of the uranyl(VI). The spacing between E_1 and S_1, defined as ν_s, represents the total symmetric stretch vibration frequency of the uranyl moiety (Wang *et al.*, 2005; Tits *et al.*, 2015). The magnitude of this frequency is sensitive to the number and type of ligands present

in the equatorial plane and can be taken as a measure of the binding strength of coordinating ligands. An increased binding strength of equatorially bound ligands will withdraw electron density from the axial oxygens, reducing the strength of the 'yl'-bond which in turn reduces the total symmetric stretch vibration frequency. Thus, a smaller E_1 to S_1 spacing is indicative of stronger bonding in the equatorial plane.

In addition to the peak positions, time-resolved measurement of the luminescence signal provides also information about the luminescence lifetime. The luminescence lifetime, which can vary between ns and ms (Drobot, 2016), is characteristic for the ligand as it correlates with the probability of the respective transitions. The lifetime also depends on many other factors such as temperature and quenching effects, so that absolute values are not particularly meaningful. However, measured luminescence lifetimes allow the investigation of multi component systems. A mono-exponential decay of the lifetime suggests the presence of only one species, a bi-exponential decay the existence of two species, and so on.

In certain cases it can be advantageous to perform TRLFS at cryogenic conditions (cryo-TRLFS). At low temperatures, quenching of the luminescence signal is minimized, lowering the detection limit of the technique significantly. This allows the detection of species, which do not show measurable luminescence at room temperature, such as uranyl(VI)-carbonates.
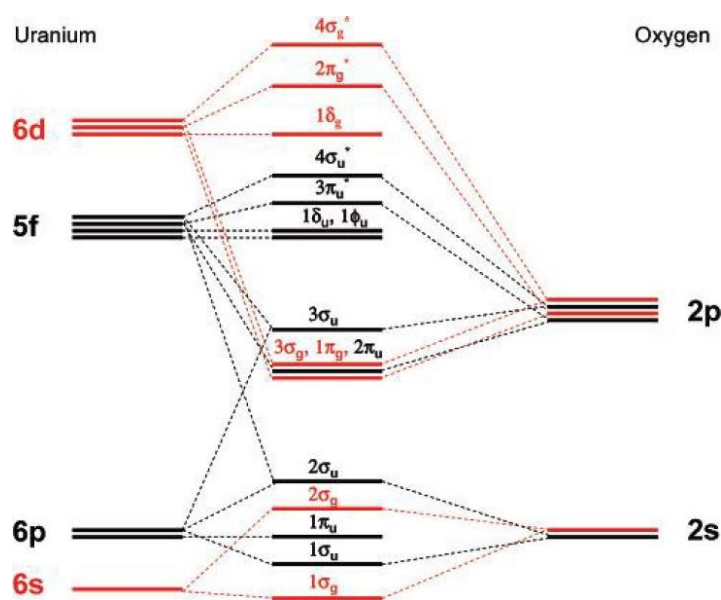
Figure 11: Relative energies of the uranyl valence orbitals. $3\sigma_u$ is the HOMO and $1\varphi_u$ is the LUMO after Denning (2007).

Conventionally, U(VI) luminescence is measured after indirect excitation with a high incident laser energy so that all U(VI) species contained in the sample are excited simultaneously. In case of a large heterogeneity of bonding environments (species or sorption sites) within the sample, this will lead to broadened and poorly resolved spectra. This broadening can be overcome by applying site-selective TRLFS at liquid helium temperatures. With this

technique single species within the sample can be excited selectively by varying the excitation energy. At each wavelength within the inhomogeneously broadened absorption band only a small subset of uranyl ions is excited directly to the lowest vibrational level of the excited state, decaying radiatively to the ground state. This leads to a significant line-narrowing in the spectrum. However, this line-narrowing can be suppressed by an effect called homo-resonance energy transfer. In case the U-atoms arranged in close distance to each other (e.g. in U(VI)-precipitates) the excited uranyl molecules transfer the energy to their neighbors, leading to a mutual excitation. As a consequence, the effect of selective excitation is canceled and the spectra appear inhomogeneously broadened. The critical distance between the donor and the acceptor uranyl ion at which the energy transfer can occur is referred to as Förster distance. For a more detailed explanation the reader is referred to Tits *et al.* (2015), who applied this technique successfully for the first time for U(VI).

2.5.2. Extended X-ray absorption fine structure (EXAFS) spectroscopy

X-ray absorption spectroscopy (XAS) is a powerful element specific technique which allows the determination of the local 3-dimensional structure around a central atom (i.e. type, number and distance of neighboring atoms). The short-range sensitivity is particularly useful for amorphous or highly dispersive materials, which are lacking the long-range order, required for the application of diffraction techniques.

XAS bases on the photoelectric effect and the wave nature of electrons. Upon irradiation of a sample with X-rays, a photon is completely absorbed, in case the energy of the incident photon at least equals the binding energy of a core-level electron. The energy of the photon is transferred to the electron (then called photoelectron) which gets ejected from the atomic shell to the continuum (photoelectric effect) (Figure 12a). This gives rise to a sharp rise in measured absorption as a function on incident X-ray energy (absorption edge) (Newville, 2004). Depending on the atomic shell from which the electron is emitted, one speaks of K-, L- or M-edge (Figure 12a). For uranium the L_{III}-edge of the 2p-electron is at 17166 eV (Nitsche, 1995). The emitted photoelectrons spherically propagate in the form of matter waves and are scattered at the neighboring atoms of the absorber atom. This leads to an interference of the initial and the scattered photoelectron waves. Thereby, depending on the wavelength of the photoelectrons and the distance of the neighboring atoms, the initial wave can be enhanced or attenuated (constructive and destructive interference) (Figure 12b) (Koningsberger *et al.*, 2000). Expression of this interference is a modulation (local maxima and minima) in the absorption spectrum directly above the absorption edge. This region of the spectrum (up to 1000 eV above the edge) is referred to as extended X-ray absorption fine structure (EXAFS). By contrast, the region of the spectrum directly at the absorption edge (-10 eV to +40 eV relative to the edge) is known as X-ray absorption near-edge structure (XANES) (Figure 13a). It provides information about the backscattering atom itself (e.g. its oxidation state) and not the surrounding structure. In this work only the EXAFS region was investigated.
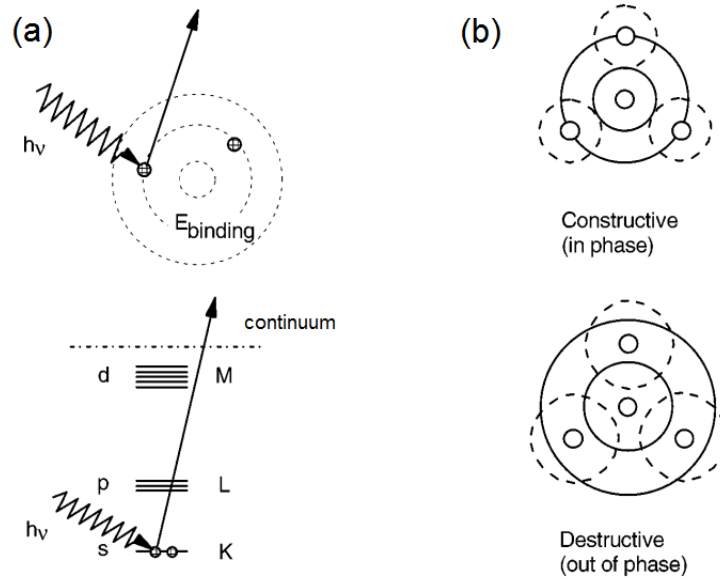
Figure 12: (a) Schematic illustration of the photoelectric effect. Excitation of electrons in different orbitals (top) at different energy levels (bottom). (b) Constructive (top) and destructive (bottom) interference of initial and backscattered photoelectron waves. Modified after Koningsberger et al. (2000).

For the measurement of the spectra monochromatized synchrotron radiation is required since it provides a high intensity and a broad tunable energy spectrum. Such radiation is accessible at the Rossendorf Beamline (ROBL) as part of the synchrotron radiation facilitiy ESRF in Grenoble, France. According to Beer-Lambert law (equation (7)) the absorption coefficient $\mu(E)$ is determined by the thickness of the sample d and the ratio between incident X-ray intensity I_0 and measured intensity I after interaction with the sample (Newville, 2004).

$$\mu(E) \times d = log\,\frac{I_0}{I} \tag{7}$$

I can be measured either in transmission or fluorescence mode. While in transmission mode the transmitted intensity behind the sample is recorded, in fluorescence mode the intensity of fluorescent X-rays (as a result of de-excitation after ejection of the photoelectron) is measured. The fluorescence intensity is proportional to the absorbance. Measurement in fluorescence mode is the preferred geometry in very dilute (geological/biological) and very concentrated samples.

After background-, deadtime- and energy (x-axis) correction of the recorded absorption spectra, the EXAFS oscillation well above the absorption edge ($\chi(E)$) can be extracted by subtracting a smooth background function $\mu_0(E)$ (idealized single atom without surrounding fine structure) from the measured absorption coefficient and normalizing it with the measured jump in absorption at the absorption edge $\Delta\mu_0(E)$ (equation (8)) (Newville, 2004).

$$\chi(E) = log\,\frac{\mu(E) - \mu_0(E)}{\Delta\mu_0(E)} \tag{8}$$
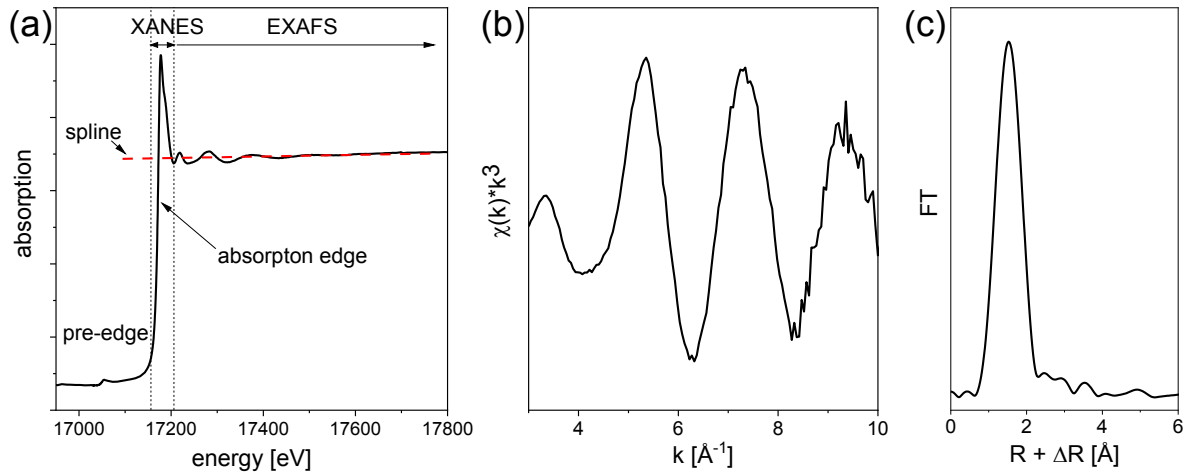
Figure 13: (a) Measured X-ray absorption spectrum, with the different regions of the spectrum (pre-edge, XANES, EXAFS) around the absorption edge. A spline is used for background correction. (b) Extracted normalized EXAFS oscillation after background correction, k-transformation and weighting with k^3. (c) Fourier transform of the EXAFS spectrum in R-Space. All spectra were taken from the U(VI) sorption sample on Ca-bentonite at pH 12.5, measured in this study (chapter 4.2.4.3).

The smooth background function cannot be measured but is numerically approximated with a spline function (Figure 13a). As the photoelectron features wave-behavior, the obtained EXAFS spectrum is commonly not plotted as a function of energy but of the wave number of the photoelectron k. Furthermore the resulting function $\chi(k)$ is weighted with k^3 in order to compensate for the decreasing oscillation amplitude at high k. A final EXAFS function is exemplarily shown in Figure 13b. Details about the EXAFS function, the contained Debye-Weller factor and the conversion from E to k are contained in Newville (2004). For a better visualization and evaluation, the EXAFS function is converted from k-space into R-space by Fourier transformation, yielding the so called Pseudo Radial Distribution Function (PRDF) (Fay *et al.*, 1988). The maxima in the Fourier transform correspond to individual radial coordination shells and show the pseudo-distances of backscattering atoms in close proximity to the central atom Figure 13c. In order to obtain quantitative structural information, such as number and distance of coordinated atoms, the measured spectra have to be approximated by *ab initio* modelling. Several well established computer programs can be used to fit theoretical structure models to the processed data on the basis of the EXAFS function. These fitting codes take into account single as well as multiple scattering paths. In this work for the shell fit theoretical scattering phase and amplitude functions were calculated with the scattering code FEFF 8.20 (Ankudinov *et al.*, 1998). Another well-established tool for EXAFS data analysis is iterative target transformation factor analysis (ITFA). It decomposes spectral mixtures into their spectral components and fractions and can therefore be applied in order to quantify the structurally different species within one sample. For a detailed description of ITFA the reader is referred to Rossberg (2002) and Rossberg *et al.* (2003).

2.5.3. Attenuated total reflectance Fourier transform infrared (ATR FT-IR) spectroscopy

Based on the principle of reaction-induced difference spectroscopy, *in situ* ATR FT-IR spectroscopy is a technique that allows the detection of small structural changes at the solid-liquid interface, as they are induced by the adsorption of uranyl moieties.

Infrared spectroscopy, in general, makes use of the fact that molecules absorb light at frequencies which match their vibrational frequencies. These resonant frequencies are characteristic for the structure of the molecule, so that the present species can be identified from the measured absorbance as a function of frequency (or wavelength). The vibrational mode relevant for U(VI) IR spectroscopy is the asymmetric stretch vibration of the axial O=U=O bond. Complexation of U in the equatorial plane weakens this bond, leading to an increased bond length and a red-shift of the spectra. The extent of this shift is related to the strength of the uranyl-ligand/surface interaction (Müller, 2010).

In attenuated total reflectance (ATR) spectroscopy, a mineral film (stationary phase) is directly prepared on an ATR crystal. When infrared light is introduced to the ATR crystal it gets reflected at the interface between the crystal and the applied mineral film. Due to the much lower index of refraction in the sample compared to the crystal, an evanescent electromagnetic field forms in the sample, which decays exponentially and therefore penetrates the sample only for a few micrometers. To obtain a total internal reflection of the incident infrared light, a critical angle between the beam and the plane perpendicular to the interface has to be exceeded. Multiple internal reflections correspond to multiple points where radiation is absorbed, leading to an attenuation of the reflected wave (Lefevre, 2004; Müller, 2010; Richter, 2015).

Mounted in a flow cell, the mineral film on the ATR crystal is rinsed by a flushing aqueous solution which could contain the adsorbing radionuclide (i.e. U(VI)). This enables *in situ* observations at the solid/liquid interface. Recording spectra at different time steps after introduction of the radionuclide furthermore enables a live and time-resolved monitoring of the sorption process. Changes at the mineral surface caused by the sorption of radionuclides become apparent by the generation of difference spectra. By subtracting a spectrum recorded before the start of the sorption from all spectra recorded at a later stage of the experiment, contributions from background and other constant parts are eliminated. Hence, all features remaining in the spectrum can unequivocally be attributed to the sorption of the radionuclide. The entire experiment has three stages: (1) A conditioning stage where the mineral film is rinsed with the background electrolyte without the radionuclide, where the stability of the mineral film can be probed; (2) A sorption stage, where the radionuclide is contained in the background electrolyte; (3) A flushing stage where the mineral film is flushed again with the radionuclide-free solution, in order to potentially trigger desorption. The principle of difference spectroscopy is illustrated in Figure 14.
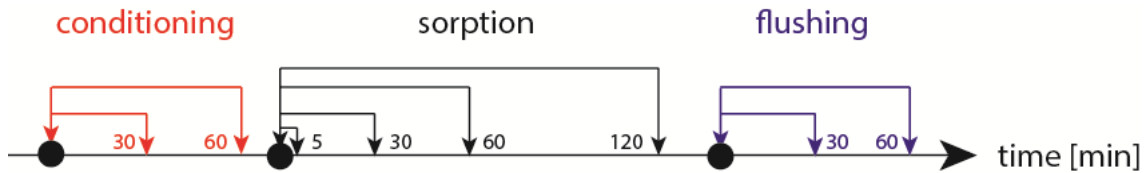
Figure 14: Principle of the calculation of difference spectra in in the three stages of the experiment during in situ ATR FT-IR spectroscopy.

2.5.4. Crystal truncation rod (CTR) and resonant anomalous X-ray reflectivity (RAXR)

The principle of surface X-ray reflectivity measurements is introduced very briefly within this chapter. For a detailed explanation, including all underlying equations, the reader is referred to Fenter (2002), Fenter *et al.* (2007) and Park and Fenter (2007).

X-ray reflectivity measurements use synchrotron-generated X-rays to probe the mineral/solution interface on the atomic level (resolution < 1 Å). X-rays are reflected at a single crystal in contact with a solution, enabling measurement at *in situ* conditions. By combination of the two techniques crystal truncation rod (CTR) diffraction and resonant anomalous X-ray reflectivity (RAXR), both surface-specific and element-specific information about the interfacial structure can be obtained. This is based on the measurement of scattered intensity, which is a function of the electron density at the mineral surface. Underlying principle is the specular reflection of X-rays on a crystal surface according to Bragg's law. Depending on the wavelength, the distance between the lattice planes and the scattering angle, the X-rays undergo interference due to reflection on different lattice planes.

In CTR measurements, the reflectivity (ratio of incident and scattered intensity) is measured as a function of momentum transfer q, which is a surface-normal vector in reciprocal space. It is defined by the difference between the reflected and incident photon wave vector (Figure 15) and depends on the wavelength λ and the diffraction angle θ (equation (9)).
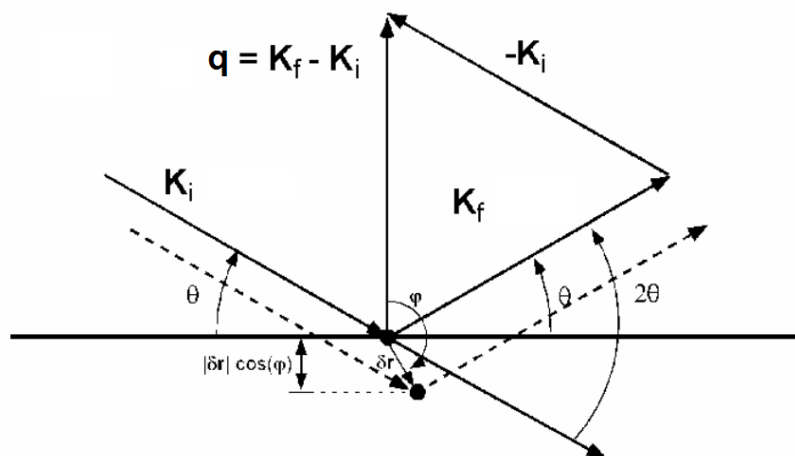
Figure 15: Diffraction of X-rays on a crystal lattice in reciprocal space. The vector of momentum transfer q is normal to the surface and is defined by the difference between the reflected beam (K_f) and incident beam (K_i).Modified after Fenter (2002).

$$q = \frac{4\pi}{\lambda} \times \sin\left(\frac{2\theta}{2}\right) \tag{9}$$

Therefore, CTR is measured while rotating the sample with respect to the beam at fixed photon energy. At geometries leading to constructive interference according to Bragg's law, Bragg peaks occur, which are intersected by lines (rods) in reciprocal space. The measured reflectivity in the regions between the Bragg peaks contains valuable information about the surface structure. The system can be described with the help of the structure factor F, which is proportional to the measured intensity. F is a function of atomic scattering factors f_j, the position R_j and the vibrational amplitude u_j of atom j (equation (10)).

$$F = \sum_{j}^{\infty} f_j(Q) \exp(i\,q\,R_j)\, exp\left[-\frac{1}{2}\left(q\,u_j\right)^2\right] \tag{10}$$

Since the X-rays scatter on the electron shell of atoms, there is a direct correlation between the electron density at the surface and the measured reflectivity. Hence, the measurement is sensitive towards changes at the mineral surface, such as adsorption of metals (Fenter, 2002).

The measured reflectivity as a function of momentum transfer (CTR, Figure 16a) can be approximated with different models according to a best-fit procedure. As an expression of the assumed model structure an electron density profile in z-direction above the surface is derived, containing information about atomic positions, surface roughness and structure of oriented water and adsorbed species (Figure 16c). However, based on the total electron density profile, it is not possible to obtain element specific information. The contribution of certain elements (e.g. adsorbed U(VI)) to the total electron density (e.g. compared to other adsorbed solution ions or water) remains speculative. Therefore CTR is complemented with the element specific RAXR technique.

RAXR makes use of the fact that even though reflectivity is principally independent of the X-ray energy, modulations of the reflectivity occur at characteristic adsorption edges if the resonant element is part of the interfacial structure. Therefore, RAXR measurements probe the reflectivity as a function of photon energy (around the adsorption edge) at fixed momentum transfer (Figure 16b). The structure factor F, described for CTR above, can be subdivided into a non-resonant and a resonant part. Once the non-resonant structure factor is known from the CTR measurement, any RAXR spectra can be explained with information specific to the resonant atom (Fenter *et al.*, 2007). By model-independent and model-dependent fitting procedures, the resonant, element-specific contribution to the total electron density can be derived (Figure 16c). Such the structure of sorbed species (height from the surface, distribution width, coverage) at the mineral surface can be characterized. As an advantage compared to other element-specific techniques (e.g. XAS), RAXR is surface-specific.
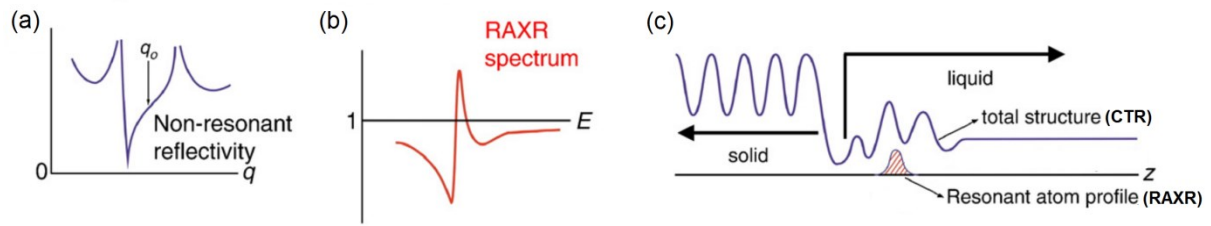
Figure 16: Non-resonant specular reflectivity as function of momentum transfer at fixed photon energy (CTR) (a) and resonant reflectivity as a function of photon energy at fixed momentum transfer (RAXR spectrum) (b). Fitting allows the derivation of the total electron density at the solid/liquid interface (from CTR) and of the resonant, element-specific fraction (from RAXR) (c). Modified after Fenter et al. (2007).

3. Materials and Methods

3.1. Materials

The Ca-bentonite was of the type *Calcigel®* (Clariant, Munich, Germany). This naturally occurring clay rock is mined in Bavaria (Germany) and was received as a powder with particle sizes between 0.5 and 150 µm, the dominant fraction (90%) of the particles being smaller than 90 µm (laser granulometer HELOS Series KF + Quixel (SYMPATEC, Clausthal-Zellerfeld, Germany), range "R3": 0.5-75 µm) (Figure 17). The mineral composition is given by the supplier according to Table 1, with montmorillonite being the major constituent (60-70%) and with a relatively large fraction of quartz (6-9%). The specific surface area of Ca-bentonite was determined to be 76.5 ± 0.3 m^2/g, applying the Brunauer-Emmet-Teller (BET) method, using a SA 3100 surface area analyzer (Beckman Coulter, Fullerton, USA). Before measurements, samples were degassed at the vacuum station of the instrument at 80 °C and at 100 °C for at least 8 h each. Nitrogen was used as adsorber gas.
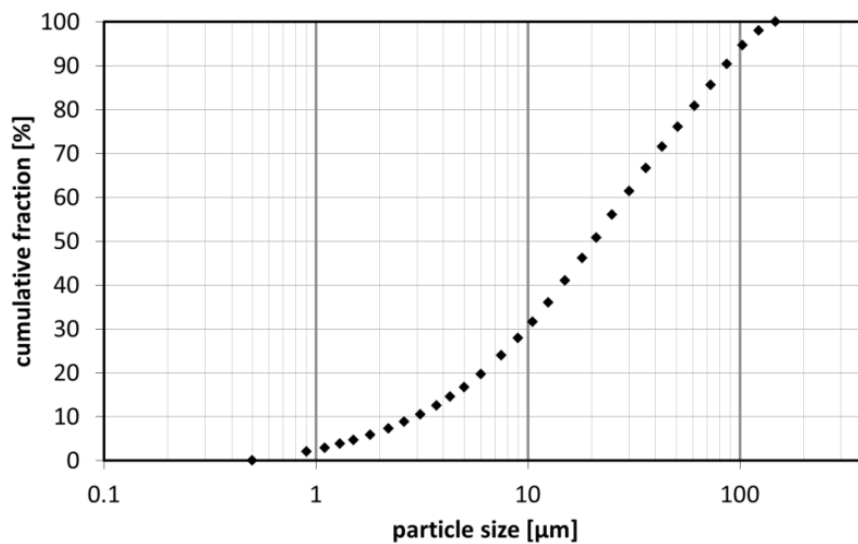
Figure 17: Particle size distribution of Ca-bentonite (Calcigel®) plotted as cumulative fraction against the grain size.

Table 1: Mineral composition of Ca-bentonite (Calcigel®) according to product information of Clariant (Munich, Germany).

Mineral phase	Fraction [%]
Montmorillonite	60 − 70
Quartz	6 − 9
Feldspar	1 − 4
Kaolinite	1 − 2
Mica	1 − 6
Others	5 − 10

Montmorillonite (SWy-2, Crook County, Wyoming, USA) was purified in the course of the PhD project of Katharina Fritsch (Fritsch, 2018) according to Bradbury and Baeyens (2009) to obtain the Na-form. A sieved fraction with particles < 63 μm and a BET surface area of 41.1 ± 0.8 m^2/g was used in the sorption experiments. Synthetic kaolinite was obtained by hydrothermal treatment of a aluminosilica gel at 220 °C by Nina Huittinen (Huittinen *et al.*, 2010) according to the procedure by Fialips *et al.* (2000). The BET surface area was determined to be 22.2 m^2/g. As observed by SEM, the size of the particles was < 1.1 μm and EDX mapping revealed that the synthetic kaolinite did not contain any impurities (only elements detected were O, Al and Si) (Huittinen *et al.*, 2010). Muscovite was purchased in the form of single crystals (12.7 × 12.7 × 0.2 mm^3) from the Asheville-Schoonmaker Mica Company (USA). These single crystals were used for the CTR/RAXR measurements. For the batch sorption experiments, the single crystals were milled with a ball mill, yielding a mineral powder, of which a < 63 μm grain size fraction was obtained by sieving. The BET surface area of the mineral fraction was determined to be 9.9 m^2/g (Hellebrandt, 2017). The elemental composition of the muscovite and the Ca-bentonite after digestion of the mineral and of the kaolinite from SEM-EDX is displayed in Table Appendix 1.

Background electrolytes in the sorption, solubility or leaching experiments were either pure NaCl (p.a., Carl Roth, Karlsruhe, Germany) solutions, mixed NaCl/CaCl$_2$ (puriss. AppliChem, Darmstadt, Germany) and NaCl/SrCl$_2$ (p.a., Merck, Darmstadt, Germany) solutions or a so called 'diluted Gipshut solution', consisting of 2.5 M NaCl, 0.02 M CaCl$_2$, 0.02 M Na$_2$SO$_4$ (p.a., Merck) and 0.0051 M KCl (p.a., Merck). Featuring a total ionic strength of 2.63 M, it simulates in situ pore waters of North German clay and salt formations at hypothetical repository depth (Wolfgramm *et al.*, 2011). Desorption experiments were performed additionally with 1 M HNO$_3$ (p.a., ISO, Carl Roth). Carbonate was introduced to the samples by adding aliquots of 1 M NaHCO$_3$ (p.a., Carl Roth) or 2 M Na$_2$CO$_3$ (p.a., Merck) stock solutions. The 0.636 M ISA stock solution was synthesized in a two-step procedure as described in detail in Brinkmann *et al.* (2019) and Dullies (2019). All solutions were prepared with deionized water (18 MΩ cm^{-1}; mod. Milli-RO/Milli-Q-System, Millipore, Schwalbach, Germany). For all experiments under N$_2$ atmosphere, water was additionally degassed prior to solution preparation.

^{238}U(VI) addition was realized with a 1×10^{-3} M stock solution (U$_{nat}$ in 0.005 M HClO$_4$). For the experiments applying ^{233}U, a 1.85×10^{-4} M UO$_2$Cl$_2$ stock solution was used. Np(VI) sorption experiments were performed with the highly active isotope ^{239}Np. The ^{239}Np stock solution was produced by irradiation of ^{238}U (UO$_2$(NO$_3$)$_2$ in Milli-Q water) at the TRIGA research reactor in Mainz. ^{239}Np was separated from its fission products by anion exchange chromatography with the resin Dowex AG 1-X8 (200–400 mesh, chloride form, Bio-Rad Laboratories GmbH, München, Germany) packed in a glass column. In a first step, the fission products were washed from the resin with 8 M HCl, while the neptunium remained adsorbed. Subsequently, ^{239}Np was eluted by washing with a mixture of 4 M HCl and 0.05 M HF. The

obtained solution was fumed several times with 1 M $HClO_4$, to finally obtain a Np(VI) stock solution (Amayri *et al.*, 2011). The concentration of the ^{239}Np stock solution was 1×10^{-11} M. The ^{45}Ca stock solution was purchased from PerkinElmer (Waltham, USA) as $^{45}CaCl_2$ in aqueous solution and had a concentration of 2×10^{-11} M.

3.2. Bentonite surface charge and stability at (hyper)alkaline conditions

3.2.1. Zeta potential

The surface charge of Ca-bentonite particles was determined by zeta potential measurements. Ca-bentonite suspensions (0.1 g/L) in the pH range 7-13 were prepared in 0.1 M NaCl, 0.1 M $NaCl + 0.02$ M $CaCl_2$ and 0.1 M $NaCl + 0.02$ M $SrCl_2$ in order to evaluate the effect of pH, calcium and strontium concentration. Samples were equilibrated with frequent pH adjustments until a constant pH was reached (after approx. 2 weeks). Measurements, based on laser Doppler velocimetry, were performed with a Zetasizer Nano ZS (Malvern Instruments, Malvern, United Kingdom). Potentials were averaged over ten measurements, each consisting of 10-50 scans.

3.2.2. Leaching at (hyper)alkaline conditions

Leaching experiments were performed as a function of pH and contact time in order to evaluate the stability of Ca-bentonite towards treatment with alkaline solutions. Duplicate samples of 10 g/L Ca-bentonite were contacted (a) with 0.1 M NaCl solution for three weeks at pH 8-13 (increments of 0.5) and (b) with diluted Gipshut solution at pH 8 for different contact times (few seconds to three weeks). The suspensions were placed on an end-over-end shaker and frequent pH adjustments (every two or three days) were done with diluted NaOH and HCl solutions. After centrifugation ($6800\times g$, 30 min) in an Avanti J-20 XP centrifuge (Beckman Coulter, Fullerton, USA), the supernatant was analyzed for Na, Mg, Al, Si, K and Ca with ICP-MS (NexION 350X, PerkinElmer, Waltham, USA), and for CO_3^{2-} with total inorganic carbon measurements (multiN/C 2100, Analytik Jena, Germany).

3.2.3. X-ray diffraction (XRD)

Powder XRD measurements were performed in order to evaluate the effect of saline and alkaline solutions on the stability of the main constituents of Ca-bentonite and to detect possible formation of secondary mineral phases. For that, the bentonite (10 g/L) was conditioned in the absence of CO_2 (N_2 glove box) with diluted Gipshut solution at pH 8-13 for 3 weeks with frequent pH adjustments in order to apply the same experimental conditions as in the sorption experiments. After centrifugation ($6800\times g$, 30 min) the wet bentonite paste was loaded into an inert gas sample holder. The measurement was conducted with the powder X-ray diffractometer Rigaku MiniFlex 600 (Tokyo, Japan), using Cu Kα radiation and a

Bragg-Brentano geometry (in θ-2θ geometry) with a step size of 0.02°2θ and a speed of 0.92 steps per second. For mineral phase identification, the ICDD PDF database was used.

3.3. Batch sorption experiments

In this section the general procedure of the batch sorption experiments is described. Details on radionuclide, carbonate, calcium and electrolyte concentrations, pH, S/L ratio and sorption time can be found in the sub-section to the respective type of experiment and in Table 2.

All sorption samples were prepared in duplicate. The mineral powder was weighed in 15 mL polypropylene centrifuge tubes (Greiner Bio-One, Frickenhausen, Germany), and was suspended with the respective background electrolyte. In the sorption experiments with ISA, calculated aliquots of the ISA stock solution were added. Experiments were carried out both at carbonate-free conditions (N_2 glove box) and in the presence of carbonate. Low dissolved carbonate (LC = 1 mM) and high carbonate (HC = 100 mM) concentrations were achieved by adding calculated amounts of $NaHCO_3$ or Na_2CO_3 to the solutions. These concentrations are representative of the lower and upper boundary of natural carbonate concentrations expected in pore waters in the North German Basin at repository depth (Wolfgramm *et al.*, 2011). CO_2 from the ambient air did not lead to additional increase of carbonate concentration within the time frame of the experiments as analytical determination of the carbonate content confirmed stable concentrations of dissolved carbonate. Measured carbonate concentrations as a function of pH are shown exemplarily in Figure Appendix 2.

Suspensions were pre-conditioned with pH-adjustments with diluted NaOH or HCl every other day until a constant pH value (±0.05) was reached (approx. two weeks). The pH was measured with an InoLab pH 7110 pH meter (WTW, Weilheim, Germany) and a SenTix MIC glass electrode (WTW). Three point calibration was executed with WTW buffer solutions (pH 6.865, 9.180 and 12.454). During this time, samples were placed in an end-over-end shaker.

In solutions with high ionic strengths, the measured potential at the pH electrode, and accordingly pH_{exp}, deviates from the true potential due to the great discrepancy between the activity coefficients of the sample and the electrolyte of the electrode (Altmaier *et al.*, 2003). By introducing a correction parameter A, the true pH can be derived according to:

$$-\log[H^+] = pH_{exp} + A \qquad (11)$$

At constant ionic strength, A is independent of pH. Empirical formulas exist to calculate A from given concentrations of pure electrolytes such as NaCl. Due to the complexity of the diluted Gipshut solution, the correction parameter A was determined for this system experimentally by measuring the pH of solutions with $I = 2.63$ M and known H^+ or OH^- concentrations. For several solutions with different pH, A was determined to be 0.4.

After pre-equilibration, U(VI), Np(VI) or Ca(II) were added to the suspension by pipetting calculated volumes of the stock solutions. In the experiments with Np(VI), 0.01 M NaClO was added in order to stabilize the hexavalent oxidation state. The sorption time was always seven days for U(VI) based on kinetic sorption experiments (see chapter 4.2.1.2). For Np(VI), the sorption time was only three days due to the short half-life of ^{239}Np. Sorption time for Ca(II) was one day. During this time the samples were rotated in an end-over-end shaker.

For phase separation, U(VI) and Ca(II) samples were centrifuged for 30 min at 6800×g in an Avanti J-20 XP centrifuge (Beckman Coulter). Photon correlation spectroscopy (PCS) measurements (Zetasizer Nano ZS, Malvern Instruments) showed that this procedure led to a sufficient phase separation, leaving no measurable particle fraction in solution. Np(VI) samples were separated for 60 min at 3770×g in a SIGMA 3K30 centrifuge (Sigma Laborzentrifugen GmbH, Osterode, Germany).

U_{nat} concentrations in the supernatants were determined by ICP-MS (see above). ^{233}U concentrations applied for the sorption isotherms were derived from liquid scintillation counting (LSC) with a Hidex 300 SL instrument (Turku, Finland), using an Ultima Gold scintillation cocktail (PerkinElmer). Using the same scintillation cocktail, ^{45}Ca concentrations in the supernatant were measured with a Winspectral α/β, Wallac 1414 liquid scintillation counter (PerkinElmer). Equilibrium concentrations of ^{239}Np after sorption were determined with γ-ray spectroscopy, using a HPGe (GMX-13180-S, EG & G ORTEC) coaxial γ-ray detector, Canberra InSpector 2000 (model IN2K, Canberra Industries, Inc., USA). The counting time was adjusted for every measurement so that both peaks at the characteristic gamma lines at 103.4 and 106.1 keV featured at minimum 10,000 counts each.

From the radionuclide equilibrium concentration (c_{eq}) and the initial radionuclide concentration (c_0) the percentage of radionuclide (RN) sorption is calculated according to equation (12). Furthermore, K_d values were determined using equation (3).

$$RN\ sorbed\ [\%] = \frac{c_0 - c_{eq}}{c_0} \times 100\% \tag{12}$$

In order to evaluate the extent of U(VI) sorption onto the vial walls, samples without mineral phase (only background electrolyte and radionuclide) were prepared and treated equivalently to the sorption samples. In the absence of CO_2, the loss of U(VI) from the solution to the vial walls was significant. However, this effect only occurred when the mineral phase was absent. This was proven by treating the used and washed vials with 1 M HNO_3. While for the sample vials without mineral phase, the removed U(VI) could be fully retrieved, no U(VI) was detected after treating the sorption sample vials. Consequently, U(VI) sorption on the vial walls can be considered as insignificant as long as the sorbing mineral is present.

Table 2: Overview of performed batch sorption experiments. 'N$_2$' refers to experiments in the absence of CO$_2$ (minimal carbonate concentrations from bentonite leaching), 'LC' to low carbonate concentrations (1 mM) and 'HC' to high carbonate concentrations (100 mM). 'Sorp.' = Sorptive, 'dil. GHS' = dil. Gipshut solution, 'ISA' = Isosaccharinic acid.

Sorptive	Experiment	Mineral	Electrolyte	S/L [g/L]	atm.	[Sorp.] [M]	pH
^{238}U(VI)	S/L ratio	Ca-bentonite	dil. GHS	0.1-20	N$_2$	5×10^{-7}	8, 10.5
					LC	1×10^{-6}	8
	Kinetics	Ca-bentonite	dil. GHS	10	N$_2$	5×10^{-7}	8, 10.5, 12.5
					LC	1×10^{-6}	8
					HC	1×10^{-6}	12.5
	pH-edge	Ca-bentonite	dil. GHS	10	N$_2$	5×10^{-7}	8-13
					LC	1×10^{-6}	8-13
					HC	1×10^{-6}	8-13
		Ca-bentonite	0.1 M NaCl + 5×10^{-4} M to 5×10^{-2} M ISA	10	N$_2$	5×10^{-7}	8-13
		Na-mont-morillonite	0.1 M NaCl	10	N$_2$	5×10^{-7}	8-13
					LC	1×10^{-6}	8-13
			2.6 M NaCl	10	N$_2$	5×10^{-7}	8-13
					LC	1×10^{-6}	8-13
		Kaolinite	0.1 M NaCl	0.5	N$_2$	5×10^{-7}	10-13
			0.1 M NaCl + 0.02 M CaCl$_2$	0.5	N$_2$	5×10^{-7}	10-13
		Muscovite	0.1 M NaCl	3	N$_2$	5×10^{-7}	8-13
			0.1 M NaCl + 0.02 M CaCl$_2$	3	N$_2$	5×10^{-7}	8-13
			0.1 M NaCl + 0.02 M SrCl$_2$	3	N$_2$	5×10^{-7}	10-13
	Desorption	Ca-bentonite	dil. GHS	10	N$_2$	5×10^{-7}	11, 13
			5 M NaCl	10	N$_2$	5×10^{-7}	11
			1 M HNO$_3$	10	N$_2$	5×10^{-7}	1
^{233}U(VI)	Isotherms	Ca-bentonite	dil. GHS	10	N$_2$	1×10^{-9} to 3.2×10^{-6}	8, 10.5, 12.5
					LC	1×10^{-9} to 3.2×10^{-4}	8
^{239}Np(VI)	pH-edge	Muscovite	0.1 M NaCl	3	Ar	1×10^{-11}	8-13
			0.1 M NaCl + 0.02 M CaCl$_2$	3	Ar	1×10^{-11}	8-13
[^{45}Ca]Ca(II)	S/L ratio	Ca-bentonite	-	0.2-20	N$_2$	2×10^{-4}	10
	pH-edge	Ca-bentonite	-	10	N$_2$	2×10^{-4}	8-13

3.3.1. S/L ratio dependence

In order to determine a reasonable solid to liquid ratio (S/L ratio) for all following experiments, the sorption of U(VI) by Ca-bentonite was tested with S/L ratios of 3, 5, 9, 13 and 20 g/L, both in the absence of CO_2 as well as at low carbonate concentration, at equilibrium pH of the Ca-bentonite in the diluted Gipshut solution (pH 8). Additional experiments were performed at pH 10.5 at S/L ratios of 0.1, 0.5, 1 and 5 g/L. The U(VI) concentration was 1×10^{-6} M in the presence and 5×10^{-7} M in the absence of CO_2.

The effect of the solid to liquid ratio on Ca(II) sorption on Ca-bentonite was investigated at pH 10 in a 2×10^{-4} M $CaCl_2$ solution with a spike of 1×10^{-12} M ^{45}Ca. S/L ratios of 0.2, 1, 2, 10 and 20 g/L were achieved by weighing in different amounts of Ca-bentonite powder.

3.3.2. Kinetic sorption experiments

The kinetics of the U(VI) sorption process on Ca-bentonite in the diluted Gipshut solution was studied by taking and analyzing aliquots from bentonite suspensions (10 g/L) at different times (1 h, 6 h, 1, 2, 3, 4, 7 days) after the addition of uranium. Such kinetic series were performed in the absence of CO_2 ([U] = 5×10^{-7} M) at pH 8, 10.5 and 12.5, at low carbonate concentration ([U] = 1×10^{-6} M) at pH 8 and at high carbonate concentration ([U] = 1×10^{-6} M) at pH 12.5.

3.3.3. Sorption isotherms

At the high ionic strength of the diluted Gipshut solution, ICP-MS is not suitable for determination of U(VI) concentrations < 1×10^{-7} M, since operation of the instrument in this case requires strong dilution. Therefore, ^{233}U was used as a tracer for U(VI) sorption isotherms and ^{233}U(VI) concentrations were determined with liquid scintillation counting. U(VI) sorption isotherms on Ca-bentonite were recorded at pH 8 both in the absence of CO_2 and at low carbonate concentration with [^{233}U]U(VI) concentrations of 1×10^{-9} M to 3.2×10^{-6} M and 1×10^{-9} M to 3.2×10^{-4} M, respectively. Additional sorption isotherms at pH 10.5 and 12.5 were recorded in the absence of CO_2.

3.3.4. pH dependency of sorption

U(VI) sorption on Ca-bentonite as a function of pH was investigated in diluted Gipshut solution and 0.1 M NaCl at a S/L ratio of 10 g/L in the absence of CO_2 ([U] = 5×10^{-7} M), at low carbonate concentration ([U] = 1×10^{-6} M) and at high carbonate concentration ([U] = 1×10^{-6} M), each in the pH range 8-13, with increments of 0.5.

The influence of isosaccharinic acid on U(VI) retention in this system was studied in three additional pH-edges with ISA concentrations of 5×10^{-4}, 5×10^{-3} and 5×10^{-2} M (corresponding to an U:ISA ratios of 1:1,000, 1:10,000 and 1:100,000), achieved by addition of calculated

aliquots of the ISA stock solution after two weeks of pre-equilibration of Ca-bentonite suspensions. After another week of reaction time U(VI) was finally added to the suspensions.

The influence of calcium on U(VI) sorption was investigated in a number of pH-dependent sorption experiments with different minerals and different background electrolytes. These experiments include sorption on Ca-bentonite in 0.1 M NaCl (pH 8-13), on Na-montmorillonite in 0.1 and 2.6 M NaCl (pH 8-13), on kaolinite in 0.1 M NaCl and 0.1 M NaCl + 0.02 M $CaCl_2$ (pH 10-13) and on muscovite in 0.1 M NaCl, 0.1 M NaCl + 0.02 M $CaCl_2$ and 0.1 M NaCl + 0.02 M $SrCl_2$ (pH 8-13).

Np(VI) sorption on muscovite as a function of pH (pH 8-13, increments of 0.5) was investigated in 0.1 M NaCl and in 0.1 M NaCl + 0.02 M $CaCl_2$, both in the absence of CO_2 (Ar glove box) and at an initial Np(VI) concentration of 1×10^{-11} M.

Ca(II) sorption experiments on Ca-bentonite (10 g/L) as a function of pH (pH 8-13) were performed in the absence of CO_2 (N_2 glove box) in 2×10^{-4} M $CaCl_2$ spiked with 1×10^{-12} M ^{45}Ca.

3.3.5. Desorption

The stability and reversibility of U(VI) sorption on Ca-bentonite at pH 11 in the absence of CO_2 was tested in batch desorption experiments. After performing sorption experiments in diluted Gipshut solution (as described in chapter 3.3.4), the samples were centrifuged for 10 min at $3000 \times g$ (Avanti J-20 XP) and the supernatant was removed. After that, 10 mL of four different U(VI)-free solutions (dil. Gipshut solution at pH 11 and 13, 5 M NaCl and 1 M HNO_3) were added and the U-loaded Ca-bentonite was resuspended. After one week of reaction time the supernatant was analyzed for remobilized U(VI) with ICP-MS.

3.4. Solubility tests

Samples without mineral powder were prepared in order to investigate the solubility of U(VI) in the bentonite leachate under the given experimental conditions. As polypropylene centrifuge tubes showed significant uptake of U(VI) in the absence of the mineral, for these experiments fluorinated ethylene propylene (FEP) vials (Thermo Scientific Nalgene, Waltham, USA) were used, featuring an inert surface that minimizes uranium adsorption. Leachates of Ca-bentonite were produced at different pH values by contacting it with diluted Gipshut solution (10 g/L) for 2 weeks with continuous pH adjustments (pH 8 – 12.5, increments of 0.5). After phase separation, U(VI) was added to 10 mL of the leachate to reach a U(VI) concentration of 5×10^{-7} M. Seven days after U(VI) addition, the samples were ultracentrifuged (60 min, $187,000 \times g$, Optima XL 100K, Beckman Coulter) and the supernatants were analyzed for uranium with ICP-MS. The solubility experiments were conducted in the absence of CO_2 (N_2 glove box).

3.5. TRLFS

The aqueous speciation of U(VI) in the diluted Gipshut solution was investigated with non-selective TRLFS at λ_{ex} = 266 nm. Measurements were performed in the absence of CO_2, at low and at high carbonate concentrations, equivalent to the pH-dependent sorption studies. Batch samples with uranium concentrations of 5×10^{-7} M in diluted Gipshut solution were prepared in FEP vials at pH 8-13. After 7 days, with frequent pH adjustments, 1 mL of each sample was filled in a polystyrene one time cuvette (Carl Roth, Karlsruhe, Germany) and quick-frozen with liquid nitrogen. TRLFS measurements were performed at 153 K by using a cryogenic cooling system. The laser system used was a Nd:YAG laser (Minilite high-energy solid-state laser; Continuum, San Jose, USA) as described in Steudtner *et al.* (2011) operating at an average pulsed energy of 0.3 mJ. The emission of the samples was recorded using an iHR550 spectrograph (HORIBA Jobin Yvon, Bensheim, Germany) and an ICCD camera (HORIBA Jobin Yvon). A gate width of 2000 µs and a slit width to the spectrograph of 2000 µm were chosen. Spectra were recorded at different delay times (t_i), defined by the equation $t_i = 0.1 + 0.005 \cdot x + i^{4/2000}$, with i being the step number. At each time step, 100 measurements were averaged. Peak positions were identified from second derivatives of FFT-filter smoothed spectra by determining their negative maxima. Luminescence lifetimes were obtained by plotting cumulative intensities at each time step against delay time. Data points were then fitted exponentially.

Site-selective TRLFS was applied to investigate the U(VI) species sorbed on the surface of Ca-bentonite, muscovite and kaolinite. Samples were prepared in the absence of CO_2 as described in chapter 3.3, but with lower S/L ratio (0.3 g/L) in order to increase the U(VI) surface coverage. Two samples were prepared with Ca-bentonite in diluted Gipshut solution at pH 11, where sorption is at maximum: One with the same U(VI) concentration as in the pH-dependent sorption experiments (5×10^{-7} M) and one with a U(VI) concentration two orders of magnitude higher than that (5×10^{-5} M) to provoke U(VI) precipitation for comparison. U(VI) sorption on muscovite was investigated in 0.1 M NaCl at pH 11 and in 0.1 M NaCl + 0.02 M $CaCl_2$ at pH 11 and 12. Kaolinite samples were prepared in 0.1 M NaCl at pH 10 and in 0.1 M NaCl + 0.02 M $CaCl_2$ at pH 12. After ultracentrifugation (187,000×g) each wet paste pellet was transferred into a copper sample holder with a sealable quartz glass lid. Measurements were performed with a pulsed Nd:YAG (Continuum Surelite II, San Jose, USA) pumped dye laser setup (Radiant Dyes Narrow Scan K, Wermelskirchen, Germany). The emitted luminescence light was directed into a spectrograph (Shamrock 303iAndor Oxford Instruments, Abingdon, United Kingdom) equipped with a polychromator with 300, 600, and 1200 lines/mm gratings, and the emission was monitored with an intensified CCD camera (Andor iStar, Oxford Instruments) 10 µs after the exciting laser pulse in a time window of 10 ms. The laser pulse energy and the exact excitation wavelength were monitored in every measurement with an optical power meter (Newport 1918-R, Irvine, USA) and a wavelength meter (High Finesse WS-5, Tübingen, Germany), respectively. Spectra were

recorded at excitation wavelengths between 460 and 520 nm with a step size of 0.2 nm. Additionally, time-resolved luminescence spectra were recorded at selected excitation wavelengths with a temporal step size of 10 μs. To achieve the desired spectral resolution the solid samples were cooled to ~10 K in a helium-refrigerated cryostat.

3.6. *In situ* ATR FT-IR spectroscopy

Infrared spectra were measured from 1800 to 800 cm^{-1} on a Bruker Vertex 80/v vacuum spectrometer equipped with a Mercury Cadmium Telluride (MCT) detector. A KRS-5 diamond crystal was used and 256 scans were averaged for each spectrum. 2.5 μL of a 2.5 g/L Ca-bentonite suspension in 0.1 M NaCl was evaporated to leave a mineral film on the surface of the ATR diamond crystal. First, the mineral film was conditioned by rinsing with the blank solution for 60 min at a flow rate of 100 μL/min. Thereafter, sorption was induced by rinsing the mineral film for 120 min with 0.1 M NaCl, containing 2×10^{-5} M U(VI). Finally, the mineral film was flushed again with 0.1 M NaCl for 60 min. Three samples at different pH (6.8, 8 and 10.5) were prepared in the absence of CO_2 in FEP vials (Thermo Scientific Nalgene) and the pH was adjusted several times until a constant value was obtained. The U(VI) containing solution was ultracentrifuged (60 min, 187,000$\times g$, Optima XL 100K, Beckman Coulter) directly before the experiment in order to remove colloids from solution which might have been formed due to reduced U(VI) solubility at elevated pH.

3.7. EXAFS spectroscopy

Batch sorption samples (U(VI) on Ca-bentonite) for the EXAFS measurements were prepared as described in chapter 3.3. A total of 10 samples (Table 3) with variable pH and carbonate concentration was prepared with a S/L ratio of 0.3 g/L, leading to sufficiently high surface coverage, despite the low initial U(VI) concentrations. In order to achieve such a low S/L ratio with sufficient solid material (150 mg), the volume of suspensions was increased to 500 mL (polypropylene centrifuge tubes, Corning, Oneonta, USA). Phase separation was done with ultracentrifugation (see above), after which the Ca-bentonite wet paste was transferred into polyethylene (PE) sample holders. Samples were covered with capton tape, enclosed with a PE cap and finally sealed by soldering.

The U L$_{III}$-edge (17,166 eV) EXAFS spectra were recorded at the Rossendorf Beamline (ROBL, BM20) at the European Synchrotron Radiation Facility (ESRF) (Matz *et al.*, 1999), operated at 6 GeV and an electron current of 200 mA. For rejection of higher harmonics two Rh-coated mirrors were used and the incident white X-rays were monochromatized with a liquid nitrogen cooled Si(111) double crystal monochromator. Samples were measured under cryogenic conditions (15 K) by using a closed cycle He-cryostat. In order to increase the signal-to-noise ratio for each sample, a maximum of 11 fluorescence spectra were recorded by counting the signal of the U L$\alpha_{1,2}$ fluorescence lines with a 13-element Ge-detector. For

energy calibration the absorption of a Y metal foil at the K-edge (17,038 eV) was measured simultaneously during each energy scan. The incident photon flux and the absorption were measured with gas filled ionization chambers. For the calculation of the photoelectron wave vector (k) the ionization potential (E_0) was set arbitrarily to $E_0 = 17,185$ eV.

EXAFSPAK (George and Pickering, 1995) and WinXAS (Ressler, 1998) were used for the data treatment which included a correction for the dead-time of the 13 fluorescence channels, energy calibration, averaging of the multiple sample scans, isolation of the EXAFS signal from the averaged data and shell fit. As a reference for the aqueous $UO_2(OH)_4^{2-}$ complex we used published data from Moll *et al.* (2014), where six absorption spectra were measured at room temperature. For the shell fit theoretical scattering phase and amplitude functions were calculated with the ab-initio scattering code FEFF 8.20 (Ankudinov *et al.*, 1998) by using an arbitrary structural model of the sorption complex and of the aqueous $UO_2(OH)_4^{2-}$ complex.

Iterative target transformation factor analysis (ITFA) (Rossberg *et al.*, 2003) was applied in order to quantify the structurally different sorption complexes and to isolate their spectra from the EXAFS spectral mixtures of the sorption samples. ITFA is a well-established tool for the decomposition of spectral mixtures into their spectral components and fractions. In the first step the spectral mixtures are decomposed into a set of eigenvectors and the semi-empirical indicator (*IND*) function (Malinowski, 2002) is applied in order to estimate the number of components (n), while *IND* reaches its lowest value at n. Once n is determined the linear combination of the n eigenvectors enables a reproduction of all spectral mixtures. The spectral components originate from the pure chemical species and/or backscattering signals stemming from atoms which change their fraction and/or coordination number (*CN*) as a function ($F(P)$) of a varied physicochemical parameter (P) like the pH, concentration, etc. The distribution of the components as $F(P)$ is model independently estimated by an orthogonal rotation of the eigenvectors through the VARIMAX procedure (Kaiser, 1958). In the third step and in order to calculate the spectra of the components and their fractional contribution for each spectral mixture, n^2-n fractions of the components must be known and fixed during the iterative target test (ITT) (Brayden *et al.*, 1988).

Table 3: EXAFS samples and their pH, carbonate concentration and U(VI) surface load.

Sample no.	Sample name	CO_3^{2-} conc. [M]	pH	U(VI) load [ppm]
1	U_Bent_N2_pH8	-	8.0	331.2
2	U_Bent_N2_pH9	-	9.0	327.6
3	U_Bent_N2_pH10.5	-	10.5	375.6
4	U_Bent_N2_pH11.5	-	11.5	259.0
5	U_Bent_LC_pH9	0.001	9.0	340.3
6	U_Bent_LC_pH10.5	0.001	10.5	1080.5
7	U_Bent_LC_pH11.5	0.001	11.5	1173.3
8	U_Bent_LC_pH12.5	0.001	12.5	1091.2
9	U_Bent_HC_pH12	0.1	12.0	591.4
10	U_Bent_HC_pH12.5	0.1	12.5	715.2

3.8. CTR/RAXR

X-ray reflectivity measurements were conducted at the GeoSoilEnviroCARS (GSECARS) beamline 13-ID-C at the Advanced Photon Source (APS, Lemont, USA). The used diffractometer was a Newport 6-circle kappa and the desired wavelength of the X-rays was controlled by a liquid nitrogen cooled Si (111) double crystal monochromator. The beam is collimated both vertically and horizontally using a pair of 1-m long Rh-coated silicon Kirkpatrick−Baez mirrors. To minimize beam damage the beam position on the sample was changed repeatedly. Sample stability during the experiments was monitored by multiple measurements of both CTR and RAXR data sets. The reflectivity data were collected with a Dectris PILATUS 100 K 2D pixel array detector. CTR scans were recorded by varying the momentum transfer between 0.09 and 5.48 Å^{-1} at a fixed incident photon energy of 14 keV. RAXR spectra were measured by varying the incident X-ray energy around the L_{III} absorption edge of U(VI) (16.87 to 17.47 keV) at different fixed momentum transfer between 0.13 and 3.62 Å^{-1}. Additional measurements were performed at the Rossendorf Beamline ESRF. For the sake of this thesis data analysis will focus on the data measured at GSECARS.

U(VI) batch sorption samples on muscovite single crystals were prepared prior to the measurements. At first, two different electrolyte solutions, 0.1 M NaCl and 0.1 M NaCl + 0.02 M $CaCl_2$, were adjusted to pH 11. Then muscovite single crystals were freshly cleaved and immersed in the solutions. Finally calculated amounts of a $UO_2(NO_3)_2$ stock solution were added in order to reach a U(VI) concentration of 5×10^{-5} M. One blank sample was prepared without addition of U(VI). Sorption time was 24 h, before the samples were transferred into a sample cell. After 20 µL of the reaction solution were pipetted on top of the sample, it was covered with a Kapton film and sealed with two additional Kapton domes (for details about the sample holder, the reader is referred to Schmidt *et al.* (2012)). The three samples which were prepared for measurement were (1) U(VI) sorption on muscovite at pH 11 in 0.1 M NaCl + 0.02 M $CaCl_2$, (2) U(VI) sorption on muscovite at pH 11 in 0.1 M NaCl, and (3) muscovite at pH 11 in 0.1 M NaCl + 0.02 M $CaCl_2$.

4. Results and Discussion

4.1. Bentonite surface charge and stability at (hyper)alkaline conditions

4.1.1. Zeta potential

Zeta potential measurements of Ca-bentonite in 0.1 M NaCl show a negative surface charge over the entire pH range, as it can be expected from the permanent negative charge of 2:1 clay minerals due to isomorphous substitution of cations within the octahedral and tetrahedral layers (Figure 18). With increasing pH, surface charge becomes increasingly negative, reaching approximately -40 mV at pH ~12.5. A less negative surface charge was observed at pH ~13 due to extremely high ionic strength of the solution, caused by the addition of large amounts of NaOH. At high ionic strength the potential is generally dragged towards neutral charge due to the high density of cations close to the surface. The influence of the additional presence of bivalent cations (Ca^{2+} and Sr^{2+}) on the zeta potential is presented in chapter 4.4.1.
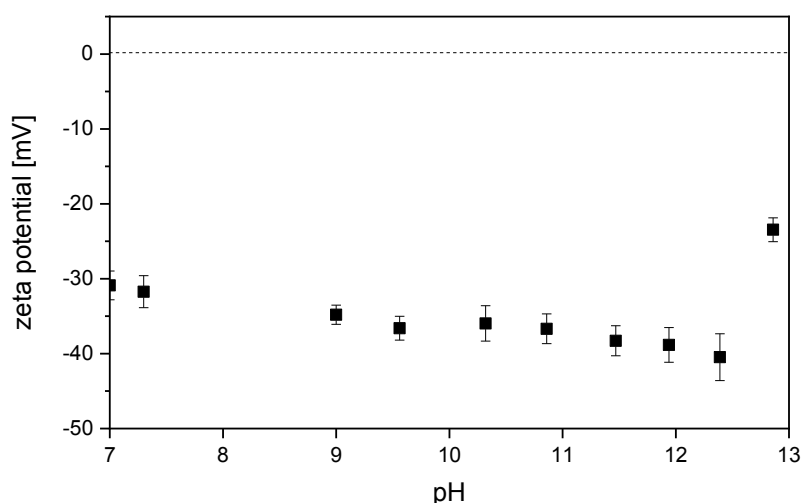
Figure 18: Surface potential of Ca-bentonite (0.1 g/L) as a function of pH in 0.1 M NaCl.

4.1.2. Powder X-ray diffraction (PXRD)

Powder XRD diffractograms of Ca-bentonite leached in diluted Gipshut solution between pH 8.5 and 13 have a very similar appearance, featuring the same main peaks (Figure 19). Major identified phases are quartz (peaks at $2\theta = 20.8$, 26.6 and 50.2°) and the clay minerals montmorillonite (peaks at $2\theta = 5.7$, 19.8, 35.1 and 61.9°), illite and muscovite. Illite and muscovite have a similar diffraction behavior so that some peaks cannot be unambiguously attributed. No alteration of mineral composition (dissolution, precipitation, recrystallization) with increasing pH was detected up to pH 12.5. Additional peaks appear at $2\theta = 11.2°$ and 27.4° at pH 12.5 and 13. These are attributed to the mineral hydrotalcite, which has been reported to precipitate from alkaline fluids in contact with bentonite (Fernández *et al.*, 2009).
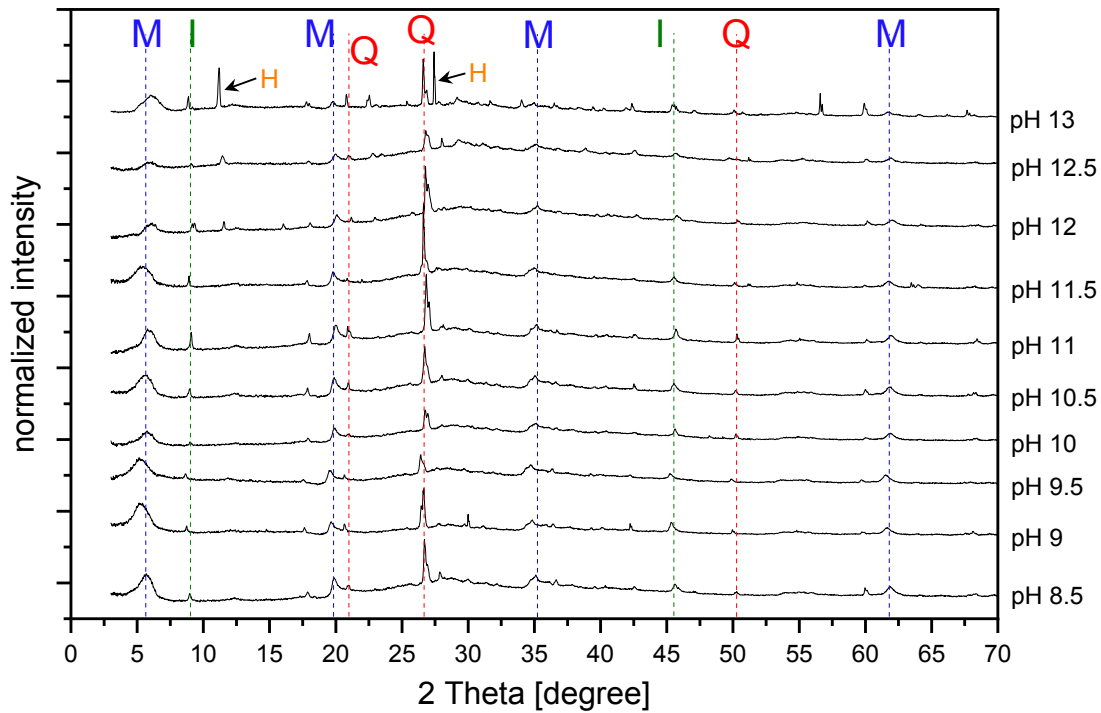
Figure 19: X-ray diffractograms of Ca-bentonite treated with diluted Gipshut solution for 3 weeks at pH 8.5-13. Mineral phases assigned to the peaks: M = montmorillonite, Q = quartz, I = illite or muscovite, H = hydrotalcite

At pH 13 additionally portlandite $Ca(OH)_2$ precipitates, being responsible for the appearance of peaks at 56.6° and 60.0°. The results suggest a general stability of bentonite up to pH 12.5. This is in accordance with several studies where treatment with alkaline fluids of pH 12.5 only led to minimal alteration of smectites or left the bentonite virtually unchanged (Vuorinen *et al.*, 2006; Fernández *et al.*, 2009; Milodowski *et al.*, 2016). Additionally, Schatz *et al.* (2013) found that Ca-montmorillonite is more stable towards chemical erosion than Na-montmorillonite. Severe alterations only occur at even higher pH values (> 13), higher temperatures and over longer timespans. However, it has to be mentioned, that these studies investigated systems with much higher S/L ratios, making direct comparison difficult. Furthermore, PXRD is not sensitive for amorphous phases, such as calcium silicate hydrate (C-S-H). Consequently, partial mineral dissolution and precipitation of amorphous minerals is possible. This is discussed with the results of the leaching experiment in chapter 4.1.3.

4.1.3. Leaching

Ions leached out of the Ca-bentonite in 0.1 M NaCl and diluted Gipshut solution to noticeable amounts are Ca, Mg, Si and Al (Figure 20). The kinetic leaching experiment at pH 8 showed that the concentrations of dissolved elements reach equilibrium after short time. Concentrations can be regarded as stable after 1 week within the margin of error (Figure 20a). Concentrations of leached carbonate, resulting from the dissolution of small fractions of calcite contained in the bentonite were determined to be at maximum 2.9×10^{-4} M. The most strongly leached element is calcium, which is predominantly mobilized from the interlayers of Ca-montmorillonite. However, calcium is removed from the solution in the presence of

carbonate by precipitation of calcite above pH 8.5 (not shown). In the absence of carbonate in diluted Gipshut solution (where calcium concentrations exceed 0.02 M) Ca precipitates as portlandite $(Ca(OH)_2)$ above pH 12 (not shown). This can be observed with the naked eye in samples at pH 12.5 and 13. In 0.1 M NaCl, leached calcium concentrations do not exceed the solubility limit with respect to portlandite (1.3 mM). Nevertheless, the amount of dissolved calcium decreases with increasing pH (Figure 20b). A possible explanation for this trend is the formation of calcium (aluminum) silicate hydrate (C-(A)-S-H) phases at hyperalkaline conditions. This would require the availability of silicon. Al and Si concentrations in the leachates are very low up to pH 12. Only at pH 12.5 and 13 a significant increase in concentration of both elements can be observed (Figure 20b). This would technically suggest a stability of the montmorillonite up to pH 12. However, in the light of calcium concentrations decreasing strongly in the solution at pH > 10, Al and Si might be released from the montmorillonite already at lower pH but are immediately bound in the form of C-A-S-H. Both Al and Si appear then in solution at pH 12.5 and 13, when the availability of calcium becomes the limiting factor for C-(A)-S-H formation. In line with this hypothesis, significant release of Al and Si from kaolinite was observed already at pH > 10 by Huittinen *et al.* (2012). C-(A)-S-H phases cannot be detected with PXRD as they have an amorphous structure.

The leaching experiments show an apparent stability of the Ca-bentonite up to pH 12.5. However, indirect proof for the release of Al and Si and formation of C-A-S-H phases at pH > 10 arises from the decreasing calcium concentrations. Consequently, C-A-S-H has to be considered as an additional sorbing mineral in the sorption experiments. Nevertheless, in relation to the remaining clay mineral fraction this can be considered as a minor contribution. Also the results of the site-selective TRLFS measurements underpin the assumption that U(VI) sorption on clay minerals is still the dominating process (chapter 4.4.2.2).
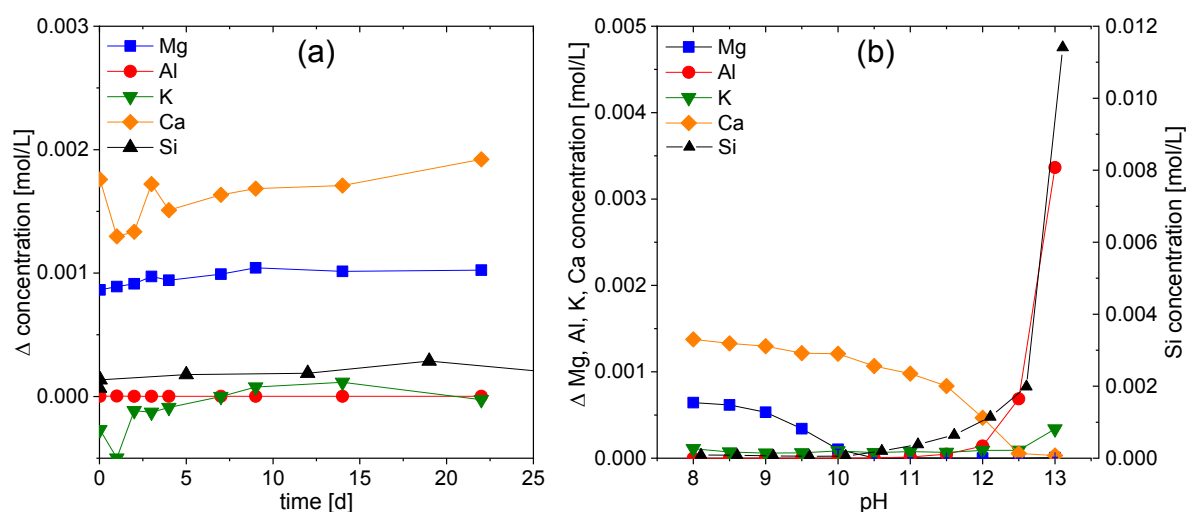
Figure 20: Concentration of ions leached out of Ca-bentonite (10 g/L) (difference to initial concentrations) in the absence of CO_2 in diluted Gipshut solution at pH 8 as a function of contact time (a) and in 0.1 M NaCl as a function of pH after three weeks of contact time (b).

4.2. Sorption of U(VI) on Ca-bentonite at hyperalkaline conditions

Parts of the results presented in this chapter are published in the following article:

Philipp, T., Shams Aldin Azzam, S., Rossberg, A., Huittinen, N., Schmeide, K. and Stumpf, T. (2019) U(VI) sorption on Ca-bentonite at (hyper)alkaline conditions - Spectroscopic investigations of retention mechanisms. Sci Total Environ 676, 469-481 (Philipp *et al.*, 2019).

4.2.1. Batch sorption experiments

4.2.1.1.   S/L ratio dependence

In the absence of CO_2, U(VI) sorption is independent of the S/L ratio in the probed range, both at pH 8 (3-20 g/L) and at pH 10.5 (0.1-5 g/L), with a sorption percentage of approx. 80% and close to 100%, respectively (Figure 21). The strong U(VI) retention at the lowest S/L ratio indicates a high excess of sorption sites in the bentonite in the absence of CO_2.

By contrast, at low carbonate concentration at pH 8, U(VI) sorption increases with increasing S/L ratio from 38% at 3 g/L to 64% at 20 g/L. Sites for uranyl adsorption in the presence of carbonate seem to be rather limited as an increase of solid fraction in the suspension caused a strong increase in sorption due to an increase of available sorption sites. This observation hints to different sorption processes in the absence and presence of carbonate at pH 8. Based on these results a S/L ratio of 10 g/L was chosen for all following batch sorption experiments with Ca-bentonite.
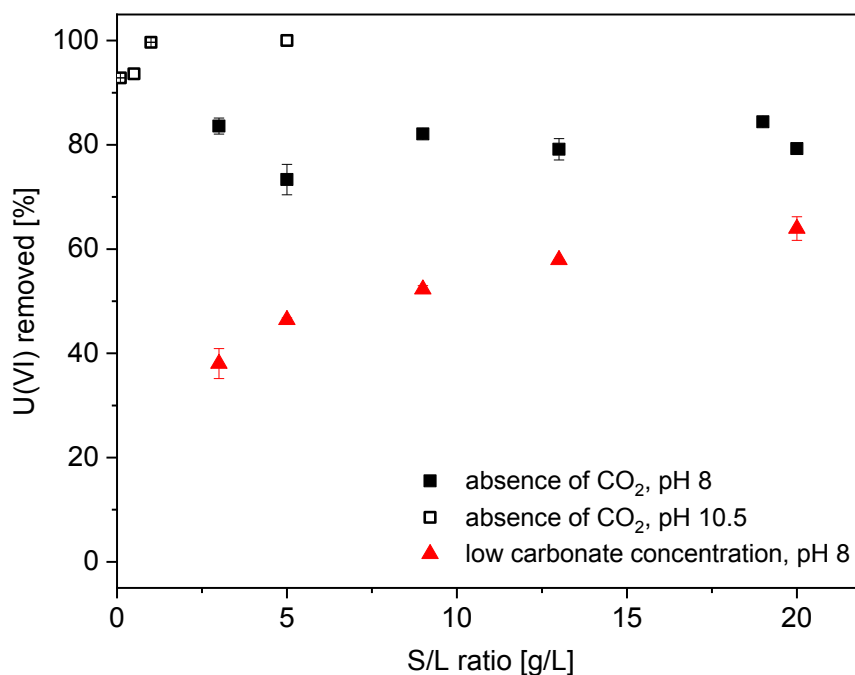
Figure 21: Percentage of U(VI) sorbed on Ca-bentonite in diluted Gipshut solution as a function of S/L ratio in the absence of CO_2 ([U(VI)] = 5×10^{-7} M) at pH 8 and 10.5 and at low carbonate concentration (1 mM) ([U(VI)] = 1×10^{-6} M) at pH 8.

4.2.1.2. Kinetic sorption experiments

All kinetic sorption experiments show that the U(VI) sorption process is fairly fast. At low carbonate concentration at pH 8 half of the maximum sorption of 62% is already reached after one hour and sorption is almost completed after two days. In the absence of CO_2 (pH 8, 10.5 and 12.5) and at high carbonate concentration at pH 12.5 the U(VI) sorption process is even faster. After one hour sorption is already almost completed and it finally reaches a plateau after one day (Figure 22). The similarity between the kinetic behavior in the system without carbonate and the system with carbonate at pH 12.5 indicates that the underlying retention mechanisms under these conditions are similar. This will also be discussed in chapters 4.2.1.4 and 4.2.2. To guarantee that the reaction has reached equilibrium, sorption time in all other experiments was chosen to be 7 days.
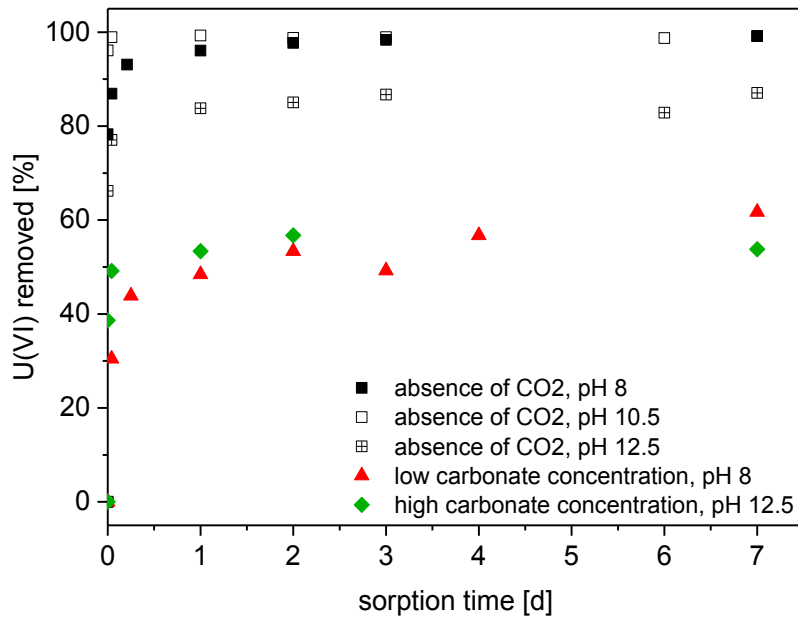
Figure 22: Percentage of U(VI) sorbed on Ca-bentonite in diluted Gipshut solution at different pH in the absence of CO_2 ([U] = 5×10^{-7} M) and at low and high carbonate concentrations ([U] = 1×10^{-6} M) as a function of sorption time.

4.2.1.3. Sorption isotherms

When plotting the logarithm of the equilibrium amount of uranium sorbed on the bentonite a_{eq} against the logarithm of the equilibrium uranium concentration in the solution c_{eq} (Figure 23), the slope of a linear fit represents the Freundlich exponent n (eq. (13)). If the slope of the fit is 1, the sorption behavior can be described as linear, as the Freundlich isotherm (eq. (5)) then equals the linear Henry isotherm (eq. (4)). In that special case, the y-intercept represents the $\log(K_d)$ value.

$$\log(a_{eq}) = n \times \log(c_{eq}) + \log(k_F) \tag{13}$$

In the absence of CO_2, n was determined to be 0.99 at pH 8 and 1.03 at pH 12.5, indicating a linear sorption behavior (Figure 23a,b). On the contrary, at low carbonate concentration at pH 8 sorption cannot be described as linear since a Freundlich exponent of 0.89 was obtained. The K_d values were derived by forcing the fit through the data points to have a slope of 1. Resulting $\log(K_d)$ values were 2.19 log(L/kg) at low carbonate concentration at pH 8 and 3.03 and 3.06 log(L/kg) in the absence of CO_2 at pH 8 and 12.5, respectively. Consequently U(VI) sorption on Ca-bentonite at pH 8 is much weaker in the presence of carbonate, which is in accordance with previous studies (see chapter 2.4).

Another sorption isotherm was recorded in the absence of CO_2 at pH 10.5. In the entire U(VI) concentration range of 1×10^{-9} M to 3.2×10^{-6} M the uranium was removed to 100%. As no uranium was left in solution after the experiment ($c_{eq} = 0$), irrespective of the initial concentration, no isotherm could be plotted. Nevertheless, this observation contains valuable information. The complete retention over the entire concentration range suggests that the U(VI) removal at high initial concentration (i.e. $\geq 1 \times 10^{-8}$ M) is probably not due to precipitation, because the same removal is observed when oversaturation can be ruled out (at $[U(VI)] \leq 1 \times 10^{-8}$ M). Therefore, a uniform retention mechanism can be assumed for the entire U(VI) concentration range studied - most probably adsorption (discussed in the following chapters).

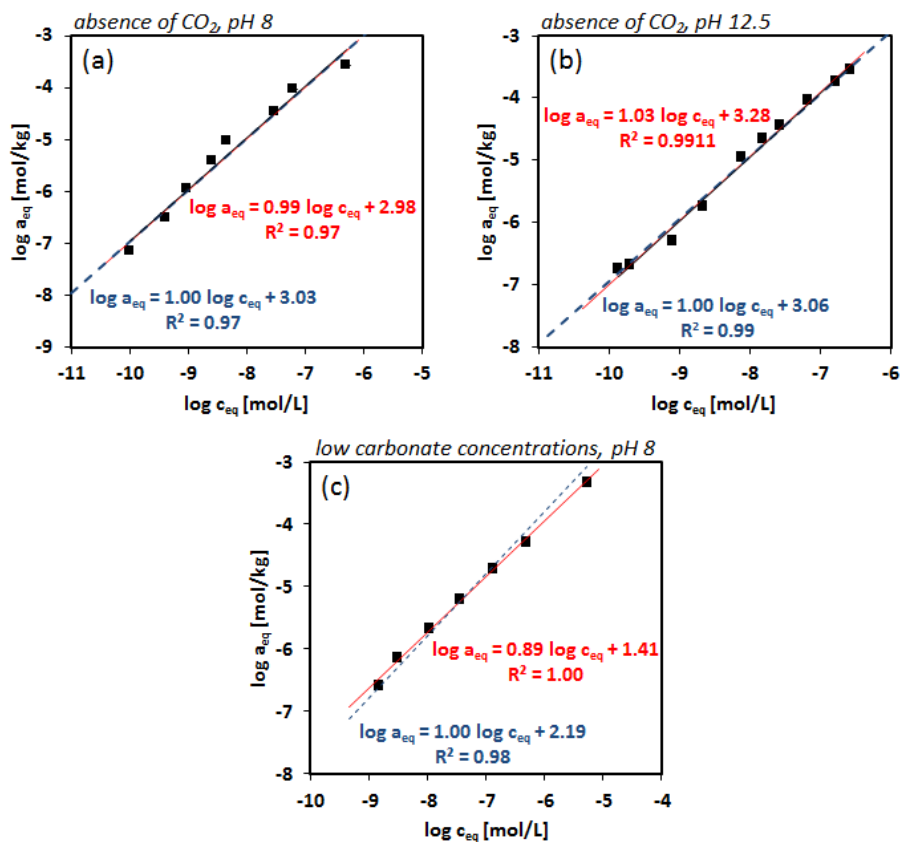Figure 23: Sorption isotherms at pH 8 and pH 12.5. Red lines show a linear fit through the data points. Dashed blue lines represent a fit with a forced slope of 1. (a) Sorption isotherm in the absence of CO_2 at pH 8, (b) Sorption isotherm in the absence of CO_2 at pH 12.5. (c) Sorption isotherm at low carbonate concentrations at pH 8.

The sorption isotherms reveal that at pH 8 the adsorption of uranyl in the presence and absence of carbonate follows different processes. The retention of U(VI) in the absence of CO_2 can be described as linear within the investigated concentration range. This indicates that enough sorption sites are available on the bentonite. This is in accordance with the sorption experiments as a function of the S/L ratio, showing that a very small solid fraction already provides enough sorption sites to reach maximum U(VI) sorption. By contrast, the removal of U(VI) at low carbonate concentration at pH 8 is non-linear, meaning that not enough high affinity sites are available or that the complexes are generally hampered to occupy the sites. This also fits to the observation from the S/L ratio dependent sorption, where an increased amount of solid fraction caused a substantially increased retention (see chapter 4.2.1.1). The observed differences are attributed to differences in the aqueous speciation of U(VI) as a function of carbonate concentration, which is discussed in chapter 4.2.2.

4.2.1.4. pH dependency of sorption

Batch sorption experiments as a function of pH exhibit a complex U(VI) retention behavior depending on the amount of carbonate present in solution (Figure 24). In the absence of CO_2, U(VI) retention is approx. 90% at pH 8-9 (squares in Figure 24). At higher pH, sorption even increases, forming a plateau of complete retention from pH 9.5 to about pH 12. At pH $\geq$ 12, U(VI) sorption decreases again to only 50% at pH 13. At low carbonate concentration (1 mM), U(VI) retention is low (approx. 20%) at pH 8-9. Going to higher pH values, the retention increases drastically, following a similar pH-dependent trend as in the absence of CO_2. Also here a plateau of complete sorption is observed at pH 10-12, followed by a pronounced drop at pH $\geq$ 12 (triangles in Figure 24). When carbonate concentration is high (0.1 M), U(VI) retention remains on a very low level (< 10%) up to pH 11. Thereafter it increases, reaching 80% at pH 12 (diamonds in Figure 24), before dropping again, similar to the previously described series. The complete U(VI) retention in the absence of CO_2 and at low carbonate concentration corresponds to maximum $\log(K_d)$ values of approx. 5-6 $\log$(L/kg), restricted by the detection limit of the ICP-MS measurements (0.1 µg/L). At high carbonate concentration, the maximum retention at pH 12 corresponds to a $\log(K_d)$ value of 2.6 $\log$(L/kg) (Figure 25). The obtained $\log(K_d)$ values are generally in good agreement with those found in literature for U(VI) sorption by montmorillonite in the pH range 8-10. Boult *et al.* (1998), Bradbury and Baeyens (2005), Marques Fernandes *et al.* (2012) and Fritsch (2018) reported distribution coefficients of 4-5 $\log$(L/kg) in the absence of CO_2 and of 1-2 $\log$(L/kg) in the presence of CO_2. In the absence of CO_2 at pH 8 the $\log(K_d)$ value determined in the present study is comparatively small with approx. 3 $\log$(L/kg). An obvious explanation for this difference is that the main sorbing mineral phase, montmorillonite, only makes up 60–70% of the Ca-bentonite, while the aforementioned studies all investigated the sorption behavior of pure montmorillonite. Another reason could be the complexation of a minor fraction of U(VI) with carbonate which was released from the bentonite (see chapter 4.1.3).
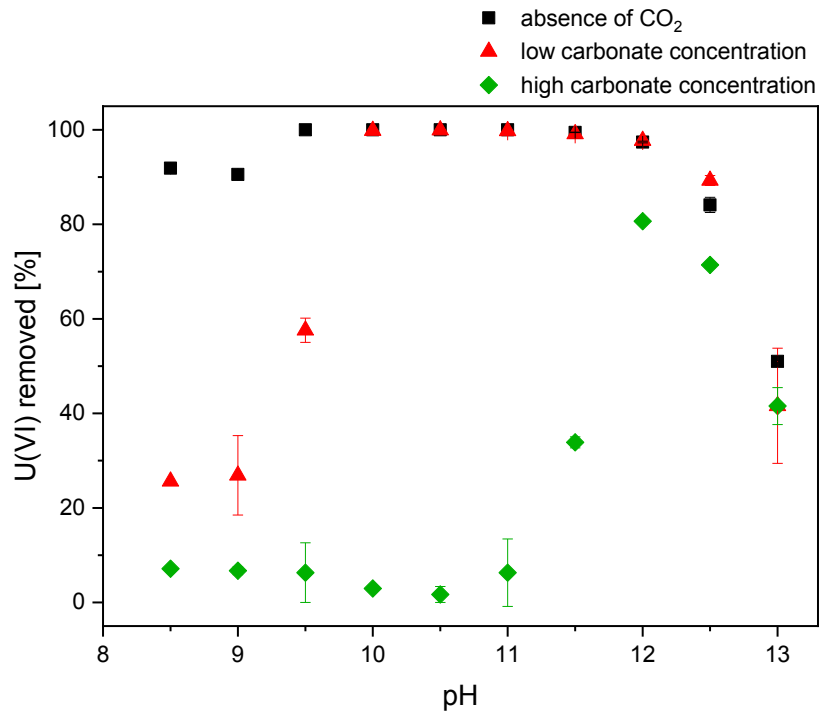
Figure 24: Percentage of U(VI) sorbed on Ca-bentonite (10 g/L) in dil. Gipshut solution (I = 2.63 M) as function of pH and carbonate concentration. Initial U(VI) concentrations were 5×10^{-7} M in the absence of CO_2 and 1×10^{-6} M at low (1 mM) and high (0.1 M) carbonate concentrations.

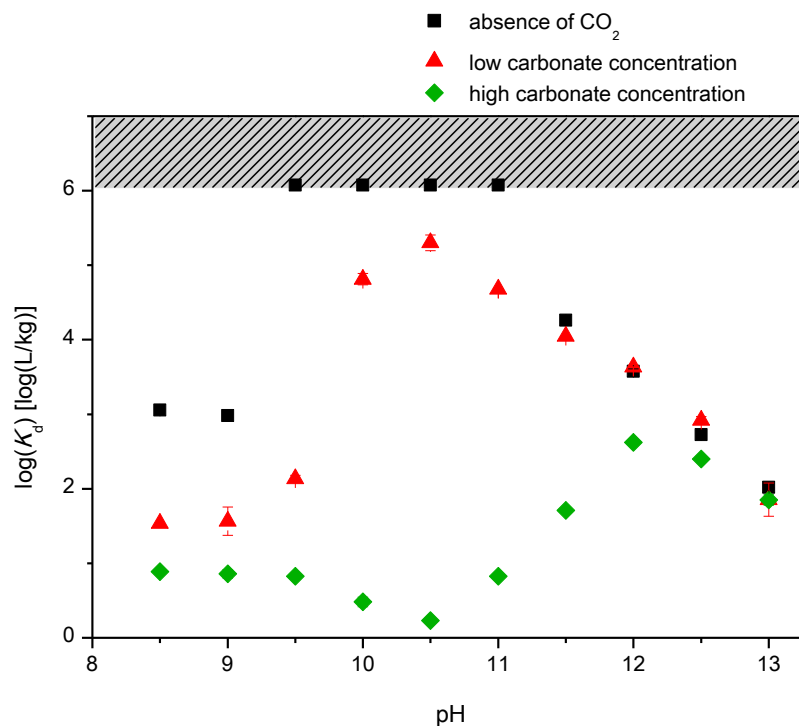*Figure 25: Logarithmized U(VI) distribution coefficients $\log(K_d)$ for U(VI) sorbed on Ca-bentonite (10 g/L) plotted as a function of pH and carbonate concentration. Initial U(VI) concentrations were 5×10^{-7} M in the absence of CO_2 and 1×10^{-6} M at low (1 mM) and high (0.1 M) carbonate concentrations.*

The strong increase of the $\log(K_d)$ at pH around 9.5 from 3 to 5-6 log(L/kg), as it has been demonstrated in this study, has not yet been reported in literature, where sorption always reached its maximum at circumneutral pH. For pH > 10, no published data exist for comparison. The lower U(VI) retention in the presence of carbonate at pH 8 to 9.5 is in accordance with literature and is attributed to the predominant formation of weakly sorbing (calcium) uranyl carbonate complexes (Bachmaf *et al.*, 2008; Marques Fernandes *et al.*, 2012; Joseph *et al.*, 2013; Maher *et al.*, 2013; Richter *et al.*, 2016; Tournassat *et al.*, 2018). An increase in retention with further increasing pH has not been systematically reported for such carbonate-containing systems as none of the mentioned studies expands to the hyperalkaline regime.

Even without discussing the underlying retention mechanism on a molecular level, the presented batch results alone provide already substantial knowledge gain as they present for the first time a systematic study of the U(VI) retention by clay rock from weakly alkaline to hyperalkaline pH. The results show that sorption can be very effective up to pH 12, also in the presence of carbonate. The decreased U(VI) retention in the presence of carbonate, reported previously in the literature, does only apply up to a certain pH and is highly dependent on the amount of carbonate in the solution.

Reasons for the observed differences in sorption behavior as a function of pH and carbonate concentration are discussed in the following chapters based on U(VI) solubility experiments and spectroscopic investigations on the aqueous and surface speciation of U(VI).

4.2.1.5.   Desorption

The stability and reversibility of the U(VI) retention at pH 11 in the absence of CO_2 was tested in batch desorption experiments. After performing sorption experiments exactly as described above, the background electrolyte was exchanged with different U(VI)-free solutions as described in chapter 3.3.5. After one week of reaction time the supernatant was analyzed for remobilized U(VI).

Exchanging the diluted Gipshut solution with exactly the same electrolyte did not lead to any remobilization of U(VI) (Figure 26). After having reached a steady distribution between the phases, no force exists that would drive the U(VI) towards the liquid phase again. Also contact with 5 M NaCl results in 0% desorption (Figure 26). Conventionally, an increase in ionic strength (as here from 2.63 to 5 M) causes a decrease of sorption in the case of outer-sphere complexation where the high density of solution ions near the surface prevents electrostatic attachment of U(VI). Consequently, conventional outer-sphere complexation can be excluded under the given conditions. This retention mechanism was anyway considered unlikely, because the ionic strength was already very high in the initial sorption experiments (2.63 M). A change of pH from 11 to 13 of the diluted Gipshut solution resulted in a U(VI) remobilization of 50.5% (Figure 26). This corresponds to the observed amount of sorption at

pH 13 in the pH-dependent batch sorption experiment (chapter 4.2.1.4) where approx. 50% U(VI) removal from solution was observed. Changing the pH of a solution is a strong alteration of the chemical system, which can cause even inner-sphere complexes to desorb. Desorption experiments with 1 M HNO_3 prove that all U(VI) was adsorbed to the Ca-bentonite in the first place and that theoretically 100% are recoverable.

Applying conventional criteria for inner- and outer-sphere surface complexation, the desorption experiments suggest that at pH 11 all U(VI) is retained in the form of inner-sphere sorption complexes, as it cannot be remobilized by a change of ionic strength, but only by a change of pH. However, in the special case of U(VI) sorption at hyperalkaline conditions, this classical concept has to be reassessed. Conventionally, outer-sphere complexation applies to cationic metal ions that adsorb to a negatively charged surface. By contrast, at pH 11 the prevailing U(VI) species are anionic (see chapter 4.2.2). In that case the solution cations are no longer direct competitors for sorption sites and also do not electrostatically repel the metal ion. They rather attract the anionic U(VI), possibly even facilitating an adsorption. Hence, anionic metal ions could possibly form outer-sphere complexes on negatively charged clay mineral surfaces via bridging cations (such as Ca^{2+}). Such kind of outer-sphere complexes would then not be influenced negatively by increasing the ionic strength. Consequently, to unequivocally distinguish the underlying retention mechanisms, spectroscopic investigations are indispensable.
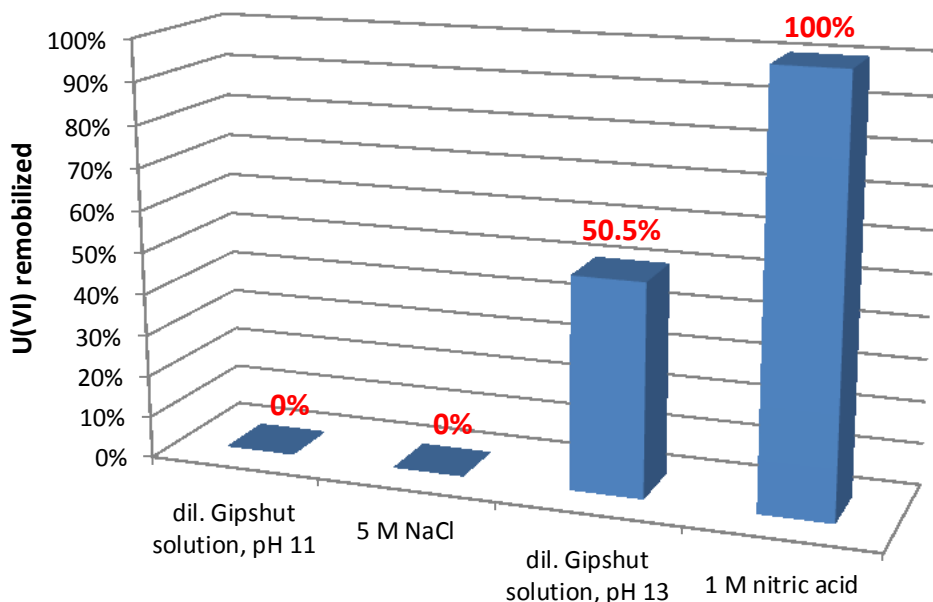

Figure 26: Percentage of U(VI) ([U] = 5×10^{-7} M) remobilized after one week of reaction time from Ca-bentonite (10 g/L) after exchanging the background electrolyte (diluted Gipshut solution at pH 11) with different solutions (as indicated in the diagram).

4.2.2. Aqueous speciation of U(VI) investigated with TRLFS

In the absence of CO_2, the luminescence spectra of U(VI) in diluted Gipshut solution measured at 153 K feature a low intensity with a poor spectral resolution (Figure 27a). Both phenomena are characteristic for uranyl hydroxide complexes at alkaline conditions. This has been reported by Moulin *et al.* (1998), Martínez-Torrents *et al.* (2013) and Drobot *et al.* (2016), where monomeric hydrolysis species $UO_2(OH)_2$, $UO_2(OH)_3^-$ were shown to exhibit broadened spectra with weak spectral splitting. In spite of the low signal to noise ratio (particularly up to pH 10), the positions of the first two main peaks could be identified, being at approx. 500 nm and 521 nm for the samples up to pH 12 (Table 4). Drobot *et al.* (2016) observed maxima at 499 and 520 nm for $UO_2(OH)_{2\ (aq)}$ and at 503 and 525 nm for $UO_2(OH)_3^-$. Moulin *et al.* (1998) and Martínez-Torrents *et al.* (2013) described peaks for $UO_2(OH)_3^-$ at 499 nm and 519 nm and at 503 and 521 nm, respectively. Luminescence lifetimes depend on the presence of quenchers and, to a large degree, on the temperature of the sample. Therefore, comparing lifetimes obtained in different studies is difficult. From the aforementioned studies only Martínez-Torrents *et al.* (2013) performed measurements at cryogenic conditions (10 K). The reported luminescence lifetime of 198 μs for $UO_2(OH)_3^-$ corresponds very well to the 208 μs obtained in the present work at pH 11 (measured at 153 K). At pH 13 the luminescence spectrum is shifted towards lower wavelength, having the first two maxima at approx. 490 nm and 511 nm (Table 4). These positions are in agreement with spectra measured by Tits *et al.* (2011) at very alkaline conditions (pH 13.3), which were assigned to the higher hydrolysis species $UO_2(OH)_4^{2-}$. In the present study, the luminescence lifetime at pH 13 was measured to be somewhat shorter than at lower pH. This observation is consistent with the works of Martínez-Torrents *et al.* (2013) and Kitamura *et al.* (1998) in which shorter lifetimes are reported for $UO_2(OH)_4^{2-}$ compared to $UO_2(OH)_3^-$. Consequently, based on analysis of peak positions and luminescence lifetimes, (anionic) uranyl hydroxides ($UO_2(OH)_2$, $UO_2(OH)_3^-$ and at very high pH $UO_2(OH)_4^{2-}$) dominate the aqueous speciation of U(VI) in the diluted Gipshut solution in the absence of CO_2 between pH 8 and 13.

In the presence of carbonate, the recorded luminescence emission spectra vary strongly within the investigated pH range 8-13. Up to pH 10 at low carbonate concentration and up to pH 11 at high carbonate concentration, the shape of the spectra is very similar, exhibiting a well-resolved spectral splitting (Figure 27b,c). Compared to the uranyl aquo ion, these spectra are shifted towards lower wavelengths, which is characteristic for uranyl carbonate complexes (Bernhard *et al.*, 2001; Wang *et al.*, 2004; Steudtner *et al.*, 2011; Lee and Yun, 2013). The obtained peak positions (first two main peaks at approx. 480 and 500 nm) match very well with literature data for $UO_2(CO_3)_3^{4-}$ and the ternary calcium uranyl carbonate complexes $Ca_2UO_2(CO_3)_{3\ (aq)}$ and $CaUO_2(CO_3)_3^{2-}$ (Table 4). Luminescence lifetimes of these samples range between 700 and 1000 μs. As peak positions are very similar and the luminescence lifetimes depend on temperature and solution composition, it is not possible to distinguish between $UO_2(CO_3)_3^{4-}$ and ternary $Ca-UO_2-CO_3$ complexes here, based on the spectral

properties. However, given that the diluted Gipshut solution contains large amounts of calcium, the formation of ternary complexes with calcium is expected. Another plausible complex is $MgUO_2(CO_3)_3^{2-}$, which was described by Lee *et al.* (2017) with almost the same luminescence spectroscopic properties as $UO_2(CO_3)_3^{4-}$. The formation of this complex might be favored when calcium is removed successively from the solution with increasing pH due to calcite precipitation. Magnesium is then still available as brucite precipitation is initiated at somewhat higher pH. At pH 10.5 at low carbonate concentration and at pH 11.5 at high carbonate concentration, an abrupt change in speciation is visible. The well resolved emission bands are not detectable anymore. Instead, broad spectra with lower luminescence intensity are observed (Figure 27b,c). Peak positions and lifetimes compare very well to those that were obtained in the absence of CO_2 (Figure Appendix 3) and are therefore also interpreted as monomeric uranyl hydroxide complexes $UO_2(OH)_3^-$ and $UO_2(OH)_4^{2-}$. Consequently, uranyl carbonate complexes, which have been widely reported to dominate the aqueous U(VI) speciation at alkaline conditions, prevail only up to a certain pH, depending on the concentration of dissolved carbonate. At higher pH, the formation of uranyl hydroxides is favored.
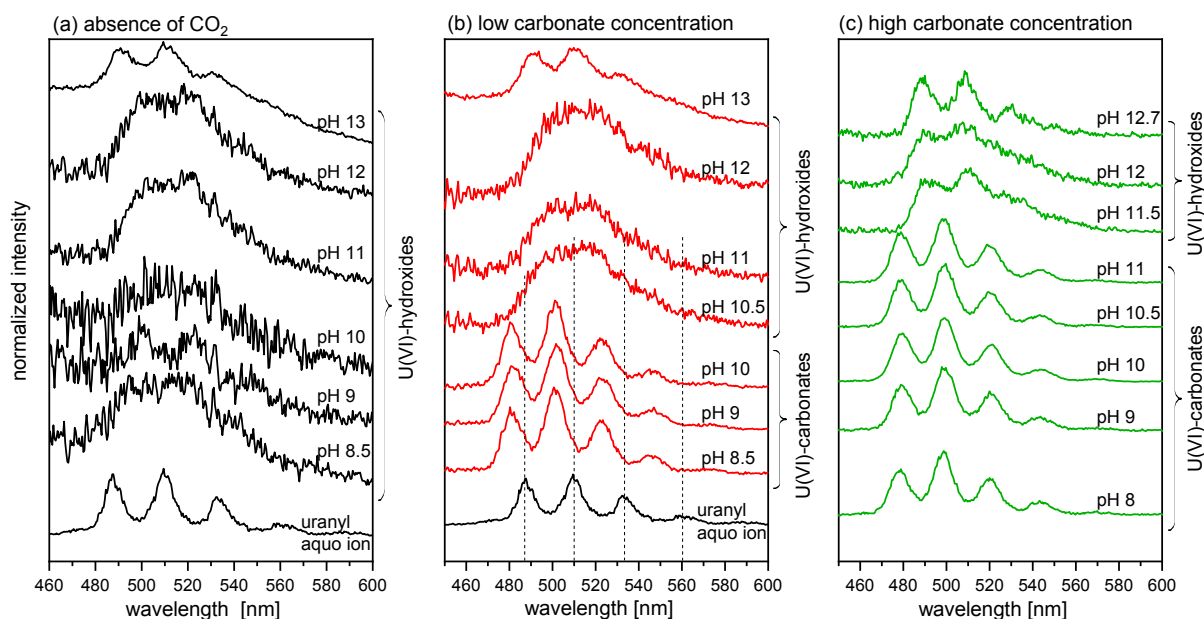
Figure 27: Luminescence spectra of uranyl ([U(VI)] = 5×10⁻⁷ M) in the diluted Gipshut solution as a function of pH in the absence of CO₂ (a), at low carbonate concentration (b) and at high carbonate concentration (c).

Table 4: Luminescence spectroscopic properties (peak positions and luminescence lifetimes) of U(VI) in the diluted Gipshut solution at different pH and carbonate concentrations (LC = low carbonate concentration, HC = high carbonate concentration). Literature data are given for comparison.

Series	pH	Peak positions [nm]				Lifetime [μs]	T [K]
N_2	8.5	497.4	517.3			-	153
	9.0	502.1	522.9			-	153
	11.0	499.3	521.0			208 ± 30	153
	12.0	500.2	521.5			130 ± 21	153
	13.0	490.4	510.7	531.6		74 ± 17	153
LC	9.0	481.2	502.1	523.4	546.9	877 ± 17	153
	9.5	481.2	501.6	523.4	546.9	995 ± 55	153
	10.0	480.8	501.1	522.9	546.0	882 ± 15	153
	10.5	495.6	518.3	546.2	567.0	193 ± 0	153
	11.0	497.0	519.2	542.8	569.6	149 ± 13	153
	12.0	496.5	523.8			166 ± 16	153
	13.0	490.4	510.3	532.5		89 ± 7	153
HC	8.0	477.4	498.3	520.0	544.1	851 ± 33	153
	9.0	478.8	499.6	521.4	544.1	804 ± 17	153
	9.5	478.8	499.2	521.4	544.1	727 ± 20	153
	10.0	479.3	499.6	521.4	544.5	704 ± 10	153
	10.5	478.8	499.2	520.5	543.1	792 ± 19	153
	11.0	477.9	499.2	520.5	544.1	808 ± 18	153
	11.5	489.9	511.2	533.4	557.5	123 ± 7	153
	12.0	489.0	508.4			133 ± 7	153
	12.5	488.1	509.4	530.2	556.3	146 ± 16	153
	12.7	488.1	508.9	530.2		112 ± 10	153
UO_2^{2+} [a]		488	509	533	560	0.9 - 2	293
$UO_2(CO_3)_3^{4-}$ [b]		480.7	499.9	520.3	542.5	834 ± 9	153
$UO_2(CO_3)_3^{4-}$ [c]		479.6	499.2	519.9	542.4	883	6
$Ca_2UO_2(CO_3)_{3\ (aq)}$ [c]		480.5	501.2	522.7	546.0	1282	6
$Ca_2UO_2(CO_3)_{3\ aq}$ [d]		484	504	524		0.036	293
$UO_2(OH)_3^-$ [e]		503.0	521.0	534.0	550.0	198 ± 8	10
$UO_2(OH)_3^-$ [f]		503	525	547	572	3.4 ± 0	274
$UO_2(OH)_3^-$ [a]		499	519	543	567	0.8	293
$UO_2(OH)_4^{2-}$ [g]		491.4	510.5			140 ± 30	153

[a] Moulin *et al.* (1998) ; [b] Steudtner *et al.* (2011); [c] Wang *et al.* (2004); [d] Bernhard *et al.* (2001) ; [e] Martínez-Torrents *et al.* (2013); [f] Drobot *et al.* (2016); [g] Tits *et al.* (2011)

A clear correlation between changes in aqueous speciation and changes in the sorption behavior can be observed. U(VI) retention on Ca-bentonite is low in the pH range, where uranyl carbonate complexes dominate the aqueous speciation according to the TRLFS measurements. The observed increase in retention in the presence of carbonate above a certain pH coincides with the change in aqueous speciation from uranyl carbonates to uranyl hydroxides. Generally, it can be stated that U(VI) retention is very high in samples, where $UO_2(OH)_3^-$ dominates the aqueous speciation. At pH > 12 the decrease in retention correlates with the formation of the higher hydrolysis species $UO_2(OH)_4^{2-}$. In the light of electrostatic interactions, it has to be discussed if the very strong U(VI) retention at pH 10-12 can be attributed to adsorption of a negatively charged metal complex to the negatively charged bentonite surface, or if the retention under these conditions is rather caused by a precipitation of uranates. This was clarified by solubility tests (chapter 4.2.3) and direct spectroscopic investigation of U(VI) sorbed on the bentonite surface (chapter 4.2.4).

4.2.3. Solubility of U(VI)

Batch samples of U(VI) in leachates of Ca-bentonite in diluted Gipshut solution demonstrate that substantial amounts of the initial U(VI) (5×10^{-7} M) remained in solution over the entire pH range after one week of contact time and after ultracentrifugation (Figure 28). Hence, the complete removal of U(VI) observed for the sorption samples at pH 10-12 cannot exclusively be attributed to precipitation from the solution. This is in contrast to literature solubility studies, where U(VI) solubility is often described to induce nanomolar concentrations at alkaline conditions (Kitamura *et al.*, 1998; Altmaier *et al.*, 2017). The solubility limiting phase between pH 8 and 13 is sodium di-uranate ($Na_2U_2O_7 \cdot H_2O$) in pure sodium chloride solutions (Altmaier *et al.*, 2017) and calcium uranate ($CaUO_4$) in the presence of calcium (Moroni and Glasser, 1995; Tits *et al.*, 2008; Tits *et al.*, 2011; Bots *et al.*, 2014; Smith *et al.*, 2015; Tits and Wieland, 2018). Due to the high calcium concentration in the diluted Gipshut solution, the precipitation of Ca-uranates would be expected in the present study. However, the solubility data given in literature were determined from undersaturation experiments, consistently yielding lower equilibrium U(VI) concentrations compared to an oversaturation approach. Furthermore, most solubility studies (e.g. Altmaier *et al.* (2017)) were conducted over much longer time spans, so that kinetics have to be considered. Under the given conditions, precipitation of uranates might be a much slower process than U(VI) adsorption, making precipitation negligible within the one-week sorption experiments. Tits and Wieland (2018) also found that at least up to 2×10^{-6} M U(VI) is stable in Ca-rich alkaline solutions for a time span of seven days. The observed partial loss of U(VI) from the solution in the present experiment might be caused by a local supersaturation with respect to uranates upon addition of the highly concentrated acidic U(VI) stock solution. Formed colloids would dissolve only slowly with time.
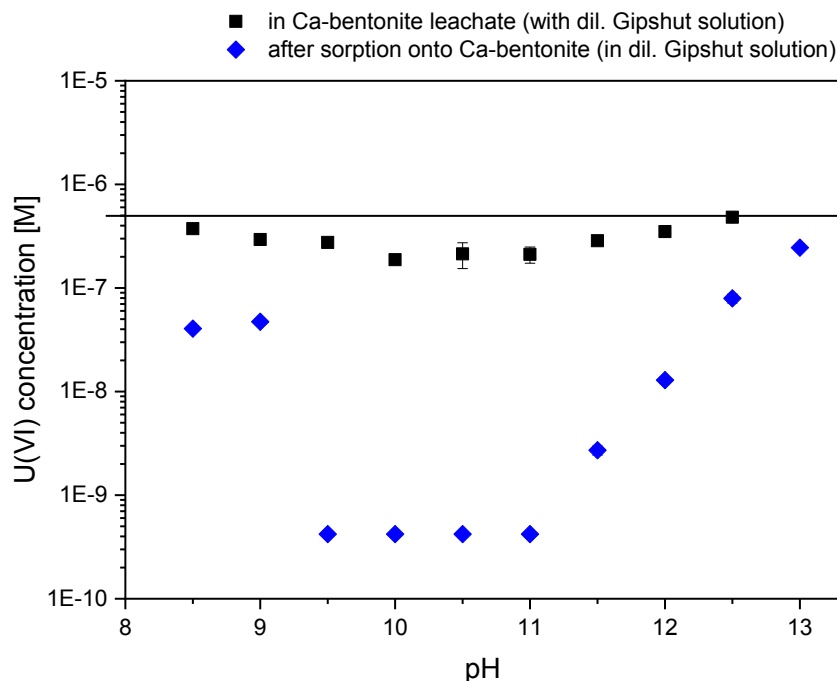
Figure 28: Solubility of U(VI) in Ca-bentonite leachate solution after 7 days contact time and ultracentrifugation in comparison to U(VI) concentrations measured after sorption experiments. The line indicates the initial U(VI) concentration of 5×10^{-7} M in the solubility and sorption experiments.

Having shown that precipitation from the solution does not play a major role, surface-mediated precipitation processes are still possible. Those could occur only when the Ca-bentonite is present, triggered by an increased U(VI) concentration near the surface. In order to unambiguously distinguish between surface precipitation and surface complexation, direct spectroscopic investigation of the U(VI) complexes sorbed to the Ca-bentonite surface was necessary (chapter 4.2.4).

4.2.4. U(VI) surface speciation

4.2.4.1. *In situ* ATR FT-IR spectroscopy

The application of *in situ* ATR FT-IR allows the monitoring of U(VI) accumulation on the Ca-bentonite surface with time. As the obtained spectra are difference spectra (relative to a conditioning stage without sorptive) the appearance of signals can unequivocally be attributed to the sorption of U(VI). The wavenumber of the peaks corresponds to the asymmetric stretch vibration of the uranyl unit and is characteristic for the U(VI) speciation. Experiments were conducted at pH 6.8 in order to be able to compare the results with previous experiments with montmorillonite (Fritsch, 2018), furthermore at pH 8, as this is the lower boundary of the range of interest of this thesis, at which U(VI) retention is already well understood (see chapter 2.4), and at pH 10.5, representative for the so far unstudied regime, where complete retention was observed in the present work in the absence of CO_2 as well as at low carbonate concentration. For the interpretation of the spectra it has to be taken into account that the

initial U(VI) concentration was much higher compared to the batch sorption experiments described above (2×10^{-5} M instead of 5×10^{-7} M, due to the detection limit of the method), so that a direct comparison and deduction of analogous mechanisms is difficult. This will be discussed at the end of this chapter.

At pH 6.8 and 8, a prominent absorption band appears at approx. 941 cm^{-1} (between 939 and 942 cm^{-1} at pH 8), evolving immediately from the onset of the sorption stage. Additionally, shoulders can be observed at lower wavenumbers, namely at 925 cm^{-1} at pH 6.8 and at 915 and 900 cm^{-1} at pH 8. This indicates the simultaneous presence of different U(VI) species on the Ca-bentonite surface. At pH 10.5 the main peak evolves with time between 927 and 929 cm^{-1}. Consequently, the structure of the retained U(VI) compound is fundamentally different from those at pH 6.8 and 8. Also here, small shoulders show the presence of multiple sorption species. In all three samples small negative absorption bands appear at the wavenumbers of the adsorption maxima during the flushing stage. However, these truncations only represent weak remobilization of U(VI) and therefore eliminate classical outer-sphere sorption as relevant retention mechanism at the given conditions.

As described in previous ATR FT-IR studies (Duff *et al.*, 2002; Wazne *et al.*, 2003; Lefevre *et al.*, 2006; Lefevre *et al.*, 2008; Müller *et al.*, 2008; Tsushima, 2011; Gückel *et al.*, 2012; Müller *et al.*, 2012; Müller *et al.*, 2013; Comarmond *et al.*, 2016), the adsorption of U(VI) to the mineral film is accompanied by a red shift of absorption bands compared to the respective aqueous species. In the absence of CO_2 at pH between 6.8 and 10.5 and a U(VI) concentration of 20 µM, the predominant aqueous species are the uranyl hydrolysis species $(UO_2)_3(OH)_5^+$, $UO_2(OH)_2$ and $UO_2(OH)_3^-$ (Müller, 2010). The asymmetric vibrational frequencies of these species decrease with increasing number of hydroxide ligands per U atom and were determined in previous studies to be 925, 922 and 895 cm^{-1}, respectively (Müller *et al.*, 2008; Müller, 2010; Müller *et al.*, 2013). The latter one was not determined experimentally but was derived from the underlying linear correlation. However, the obtained values of the main peaks in the present spectra are not red shifted compared to the respective aqueous species, but appear at higher wavenumbers. Hence, the formation of bidentate inner-sphere sorption complexes, as it has been described by Lefevre *et al.* (2006), Müller (2010), Foerstendorf *et al.* (2012), Müller *et al.* (2013) and Comarmond *et al.* (2016), is not the dominant retention mechanism in all three samples. Nevertheless, such inner-sphere complexes might form at least to some extent, inferred from the observed shoulders.

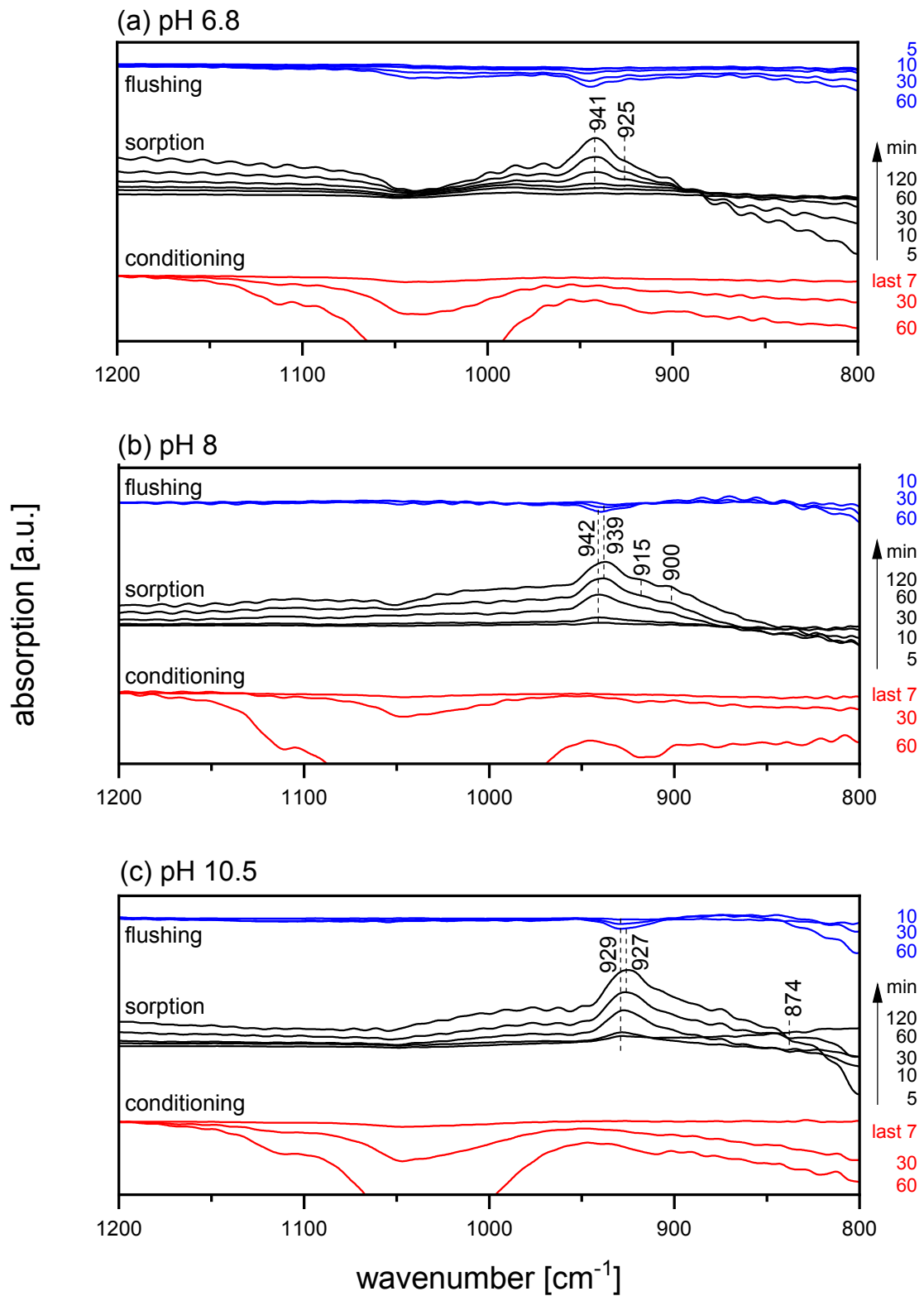*Figure 29: ATR FT-IR spectra of 2×10⁻⁵ M U(VI) sorbed on Ca-bentonite films at pH 6.8 (a), pH 8 (b) and pH 10.5 (c). Difference spectra show the time-dependent evolution of absorption with respect to the initiation of the conditioning (red), sorption (black) and flushing (blue) stage.*

The observed absorption maximum at around 941 cm^{-1} at pH 6.8 and 8 fits very well to the asymmetric vibrational frequency reported for the oxyhydroxide mineral schoepite $(UO_2)_8O_2(OH)_{12} \cdot 12(H_2O))$. Müller *et al.* (2013) determined the absorption band of synthetic schoepite to be at 939 cm^{-1} and found a schoepite-like surface precipitate on Al_2O_3 at 946 cm^{-1}. Furthermore, a colloidal U(VI) solution in 0.1 M NaCl at pH 7, measured by Müller *et al.* (2008) showed an asymmetric vibrational frequency of 940 cm^{-1}. While this comparison with literature data suggests a schoepite-like precipitate at pH 6.8 and 8, the retained U(VI) at pH 10.5 seems to be distinct from that. The precipitation of a different mineral phase than schoepite at pH higher than 8 has been shown in previous studies. Altmaier *et al.* (2017) identified the solubility limiting phase in NaCl solutions to be metaschoepite $(UO_3 \cdot 2H_2O)$ up to pH 6.5-8.5 (depending on NaCl concentration) and sodium diuranate $(Na_2U_2O_7 \cdot H_2O)$ at higher pH values. Consequently, the retained U(VI) compound at pH 10.5 could be sodium diuranate. Chernorukov *et al.* (2016) and Baran and Tympl (1966) measured infrared spectra of sodium diuranate compounds which were synthesized with variable number of H_2O molecules (water of crystallization) and Na/U ratio. The observed asymmetrical stretch vibration strongly depended on these two parameters and varied between 936 and 861 cm^{-1} and between 949 and 869 cm^{-1}, respectively. Therefore, in the present study, a clear assignment to this compound cannot be made. The observed band position of 927-929 cm^{-1} at pH 10.5 is somewhere in between the regions usually attributed to precipitation and to adsorbed species. The only U(VI) compound with a comparable asymmetric stretch vibration (927 cm^{-1}) described in literature is a oligomeric surface complex on Al_2O_3 (Müller *et al.*, 2013). Presumably such oligomeric complexes also form here and display precursors for surface precipitates.

In general, it can be stated that in all three samples (pH 6.8, 8 and 10.5) precipitation (or at least formation of oligomeric surface complexes at pH 10.5) appears to be the predominant retention mechanism. Only minor contributions of inner-sphere adsorption could be observed. This finding is reasonable because with a U(VI) concentration of 2×10^{-5} M, alkaline NaCl solutions are supersaturated by several orders of magnitude according to Altmaier *et al.* (2017). However, this does not have to hold true for the much lower initial U(VI) concentrations of the batch sorption experiments (5×10^{-7} M). Consequently, due to the detection limit, ATR FT-IR spectroscopy is capable of identifying U(VI) speciation in super-micromolar systems but does not allow determination of different retention mechanisms at sub-micromolar concentrations. Thus, in order to resolve underlying processes at 5×10^{-7} M U(VI), where precipitation is less favored, more sensitive techniques such as site-selective TRLFS (chapter 4.2.4.2) and EXAFS (chapter 4.2.4.3) were applied.

4.2.4.2. Site-selective TRLFS

Figure 30a shows the excitation spectrum (black data points) of U(VI) sorbed on Ca-bentonite at pH 11 in the absence of CO_2 and a series of selected emission spectra (in color), obtained at different excitation wavelengths. The excitation spectrum does not contain much spectral information. The absence of distinct maxima is attributed to great variety of sorption sites within the sample, leading to an inhomogeneous broadening. This heterogeneity of sorption sites is not surprising as Ca-bentonite is a very complex, multi-mineral material, where already montmorillonite provides different complexation sites (e.g. edge sharing, corner sharing) and aluminol/silanol functionalities. The variety of sorption species can also be inferred from different emission spectra, which shift strongly, depending on the excitation energy. At low excitation wavelength (e.g. 472.8 nm) the emission spectra appear broadened and weakly resolved as the incident energy is high enough to excite all uranyl moieties within the sample. At higher excitation wavelengths (in Figure 30a exemplarily shown for $\lambda_{ex} = 494.3$, 499.7 and 505.2 nm), however, a clear luminescence line-narrowing can be observed due to resonant/direct excitation of single species. The occurrence of luminescence line-narrowing alone already indicates the presence of adsorbed U(VI) surface complexes and eliminates U(VI) precipitation as the predominant retention mechanism. In U(VI) precipitates, such as Na,Ca-uranates, the phenomenon of luminescence line-narrowing is suppressed by homo-resonance energy transfer between the U-atoms arranged in close distance to each other, leading to a mutual excitation and consequently to a broadening of the signal (Lakowicz, 2006; Tits *et al.*, 2015). Such signal broadening is observed in the present batch sample prepared with an initial U(VI) concentration of 5×10^{-5} M to provoke U(VI) precipitation for comparison (Figure 30b). In fact, the obtained spectra show no luminescence line-narrowing, irrespective of the excitation energy. U(VI) precipitation at these conditions is in accordance with the *in situ* ATR FT-IR spectroscopy measurements at 2×10^{-5} M (chapter 4.2.4.1). Broad and unresolved maxima around 545 nm appear at all excitation wavelengths, featuring luminescence lifetimes between 30 and 60 µs, depending on the excitation wavelength. Spectra with similar appearance and lifetimes have been identified as Ca-uranate in Tits *et al.* (2015) and Tits *et al.* (2011). No such features were observable in the sorption sample with 5×10^{-7} M uranium, implying that adsorption can be considered as the only relevant retention mechanism at these experimental conditions.
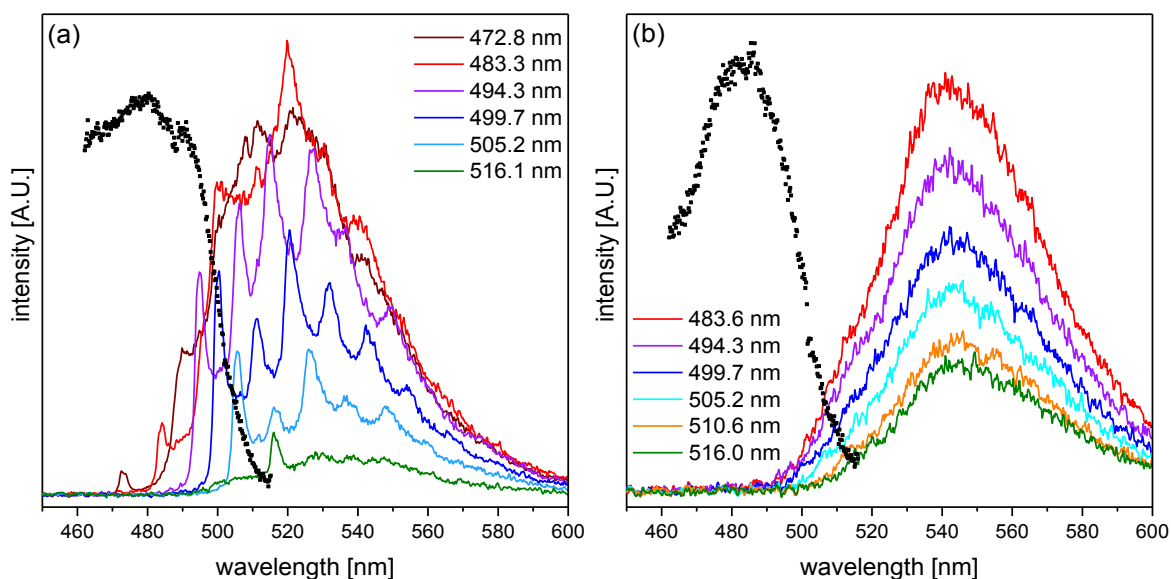
Figure 30: Excitation (black dots) and emission spectra (colored lines) of U(VI) sorbed on Ca-bentonite in the absence of CO_2 at pH 11 with [U(VI)] = 5×10^{-7} M (a) and [U(VI)] = 5×10^{-5} M (b) obtained with site-selective TRLFS at 10 K.

From the absolute positions of the narrowed peaks of the emission spectra alone, not much information about the U(VI) surface speciation can be deduced. However, the relative position of the maxima (i.e. the distance of the different electronic and vibronic transition lines) provides insight into the structure of the uranyl unit. For that purpose, electronic and vibronic transition events were assigned to the single emission lines, exemplarily shown for the emission spectrum obtained at 499.7 nm excitation wavelength (Figure 31). In phase with the incident laser energy, the resonant electronic transition line E_1 appears, followed by the lines of vibronic progression on E_1 ($S_{1,E1}$ and $S_{2,E1}$) caused by the vibronic degeneracy of the electronic ground state. Furthermore, a second (non-resonant) U(VI) species with the non-resonant electronic transition line E_2 can be identified. Also this species is superimposed by the first two lines of vibronic progression ($S_{1,E2}$ and $S_{2,E2}$). As already discussed in section 2.5.1, the spacing between the first two peaks of each species (i.e. between E_1 and $S_{1,E1}$ and between E_2 and $S_{1,E2}$, respectively) corresponds to the total symmetric stretch vibration (v_s) of the uranyl ion in the ground state. The spacing of the first (resonantly excited) species $v_s(1)$ is 781 ± 5 cm^{-1} (Table 5). With 758 ± 12 cm^{-1}, the stretch vibration $v_s(2)$ of the second, non-resonantly excited, species noticeably differs from the first one. Both frequencies lie in the typical range found for U(VI) minerals and sorbed species (Wang *et al.*, 2005; Wang *et al.*, 2011), and are significantly smaller than values found for aqueous species (Nguyen-Trung *et al.*, 2000), such as $UO_2(OH)_3^-$, which is dominating the aqueous speciation at pH 11 (Table 5). Especially for species 2, this strong weakening of the axial U-O bond implies strong bonding in the U(VI) equatorial plane upon adsorption (i.e. inner-sphere surface complexation). The comparatively higher frequency for species 1 could then hint towards outer-sphere sorption.
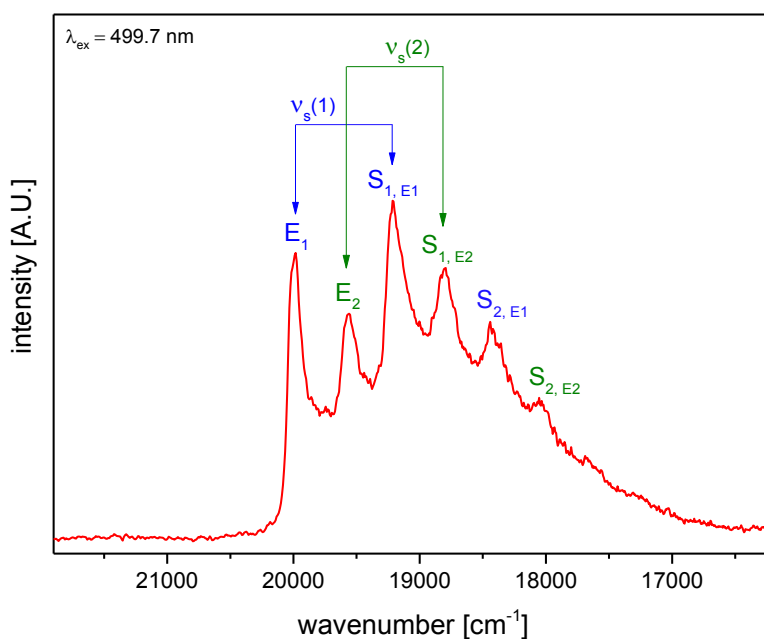
Figure 31: Luminescence emission spectrum of 5×10^{-7} M U(VI) sorbed on Ca-bentonite at pH 11 in the absence of CO_2 after laser excitation at 499.7 nm. Two U(VI) species could be identified based on their different electronic and vibronic transitions. Spacing between the first two main peaks of each species $v_s(1)$ and $v_s(2)$ are indicated.

Table 5: Frequencies of the total symmetric stretch vibration (v_s) deduced from the spacing between the luminescence emission lines of U(VI) (5×10^{-7} M) sorbed on Ca-bentonite at pH 11 in comparison to literature values.

Uranyl species	v_s [cm^{-1}]	Reference
1	781 ± 5	this study
2	758 ± 12	this study
UO_2^{2+}	870	Nguyen-Trung *et al.* (2000)
$UO_2(OH)_3^-$	804	Nguyen-Trung *et al.* (2000)
U(VI) minerals and sorbed species	700-800	Wang *et al.* (2005); Wang *et al.* (2011)
Adsorbed on C-S-H	758	Tits *et al.* (2015)

Inner-sphere surface complexation of U(VI) at montmorillonite silanol and aluminol edge sites has been previously demonstrated at neutral pH by TRLFS (Chisholm-Brause *et al.*, 2001; Chisholm-Brause *et al.*, 2004; Kowal-Fouchard *et al.*, 2004) and EXAFS (Catalano and Brown, 2005; Marques Fernandes *et al.*, 2012). Between pH 8 and 13, no spectroscopic studies dealing with U(VI) surface complexation exist for comparison. The present study suggests that inner-sphere surface complexation at pH 10-12 can occur in a similar way as at neutral pH. A couple of studies are available on U(VI) sorption by cementitious systems above pH 13. The total symmetric stretch vibration of species 2 of the present study compares

very well to that of a surface complex detected on C-S-H phases at pH 13.3 by Tits *et al.* (2015). As $UO_2(OH)_3^-$ is the dominant aqueous U(VI) species at pH 11, electrostatic repulsion does not seem to prevent this anionic complex from adsorbing to the negatively charged clay surface. The general ability of $UO_2(OH)_3^-$ to form surface complexes (in contrast to $UO_2(OH)_4^{2-}$) might be a result of electrostatic inter-ligand repulsion. According to this concept, only a limited number of OH groups can fit in the first coordination sphere of any given actinide, depending on its oxidation state. For U(VI) the maximum number of OH groups in the equatorial plane is four (Neck and Kim, 2000, 2001; Fanghänel and Neck, 2002). Therefore, $UO_2(OH)_3^-$ with three hydroxyls in its first coordination sphere is still able to form an additional bond between the surface and the metal center, while in $UO_2(OH)_4^{2-}$ the equatorial plane is fully occupied. A possible role of cations (i.e. Ca^{2+}) mediating between the anionic hydrolysis complex and the mineral surface is investigated in chapter 4.4.

The luminescence signal decays biexponentially with a short lifetime $\tau_1 = 35.5 \pm 3.9$ µs and a long lifetime $\tau_2 = 148.7 \pm 13.5$ µs, seemingly reflecting the two species identified from the narrow lines in the emission spectra. However, when inspecting single emission spectra at different delay time it becomes evident that the intensity of all narrow lines decays with the same rate (Figure Appendix 4). None of the two species vanishes as a response to a shorter lifetime. That means that both adsorbed species 1 and 2 are represented by lifetime τ_2. Even though it is not becoming apparent in the emission spectra, the shorter lifetime τ_1 is tentatively attributed to a small portion of U(VI) precipitates formed under these conditions.

4.2.4.3.   EXAFS spectroscopy

Figure 32 shows the EXAFS spectra and Fourier transforms (FT) of the sorption samples with different pH and carbonate concentrations (N_2, LC, HC), including a reference spectrum of the aqueous $UO_2(OH)_4^{2-}$ complex. None of the spectra shows indications for U(VI) precipitation (i.e. no U-U backscattering paths detected). Consequently, as already deduced from site-selective TRLFS (chapter 4.2.4.2), the predominant retention mechanism of U(VI) in Ca-bentonite under the given conditions is adsorption. A trend of decreasing average equatorial oxygen (O_{eq}) distance with increasing pH is observed within each sample series. While the peaks for O_{eq} and axial oxygen (O_{ax}) are clearly separated at pH 8 and 9, at elevated pH only combined peaks for O_{eq} and O_{ax} can be observed in the Fourier transforms (FT).

The application of ITFA showed that all ten EXAFS spectra can be reproduced with two spectral components (Figure 32). The *IND* function reaches a minimum at $n = 2$ and only the first two eigenvectors show EXAFS spectral features above the noise level (Figure 33). Consequently, two structurally different sorption complexes are present in the system with different fractions in each sample, depending on the pH. According to the result of the iterative target test (ITT) component 1 is predominant at the lowest pH of each sample set (i.e. sample 1 (N_2, pH 8.0) or sample 5 (LC, pH 9)) and occurs independently of the presence or

absence of carbonate. Conversely, the fraction of component 2 is highest in the samples prepared at high pH (Figure 34). According to the extracted single component spectra and the results of the ITFA, component 2 matches to the $UO_2(OH)_4^{2-}$ reference. Hence, for the samples with high pH, both the spectrum and the local atomic structure around U(VI) agree with those of the aqueous $UO_2(OH)_4^{2-}$ complex. Consequently, component 2 is a sorption species at the bentonite surface with a structure similar to the aqueous $UO_2(OH)_4^{2-}$ complex.

An interaction of U(VI) with carbonate would lead to the detection of a third component in the sample series LC and HC. However, only two components were detected. Consequently, no ternary U(VI) carbonate sorption complexes are present on the Ca-bentonite surface. This observation is in accordance with the work of Marques Fernandes *et al.* (2012), where no influence of carbonate on the surface complexation could be detected with EXAFS, also supporting the hypothesis of Tournassat *et al.* (2018) that uranyl carbonate complexes do not adsorb on montmorillonite surfaces to significant amounts.

Shell fitting of the ITT isolated spectrum of component 1 and of the spectrum of the aqueous $UO_2(OH)_4^{2-}$ complex was performed, while the latter was selected instead of the ITT isolated spectrum of component 2 in order to gain a higher resolution for the determination of radial distances due to the larger available *k*-range. The fit of the spectra and the corresponding EXAFS structural parameters are given in Figure 35 and Table 6.
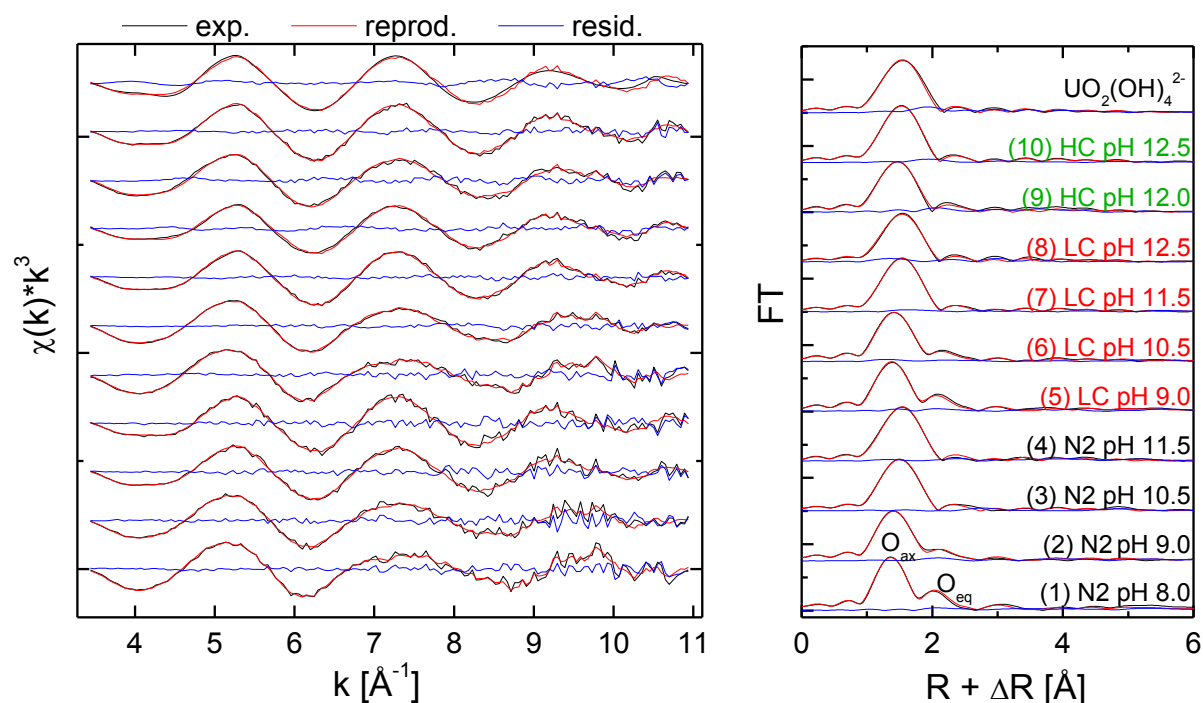
Figure 32: U L$_{III}$-edge EXAFS spectra (left, black) and corresponding Fourier transforms (right, black) with reproductions (red) and the residual (blue) of U(VI) sorption samples on Ca-bentonite in the absence of carbonate (N$_2$) and at low (LC) and high (HC) carbonate concentrations, including a reference spectrum of the aqueous $UO_2(OH)_4^{2-}$ complex (Moll et al., 2014).
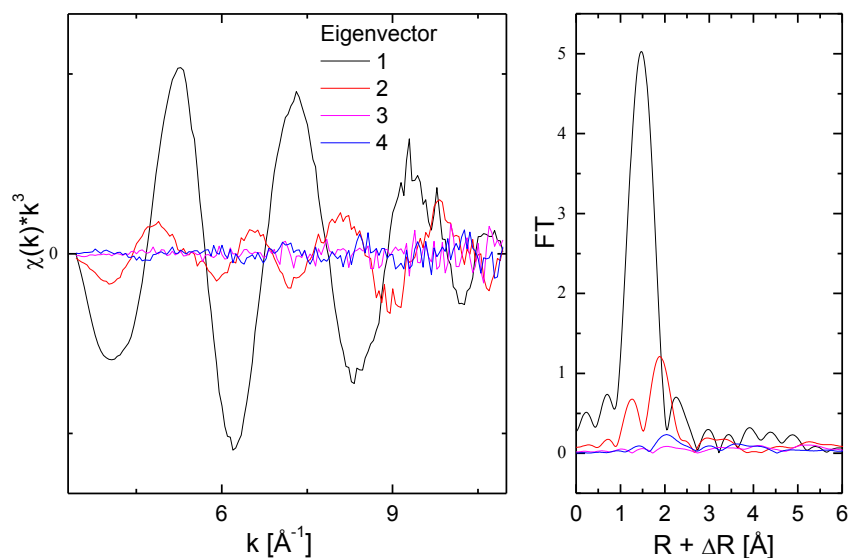
Figure 33: U L$_{III}$-edge EXAFS spectra of the first four eigenvectors (left) and their corresponding Fourier transforms (FT) (right).
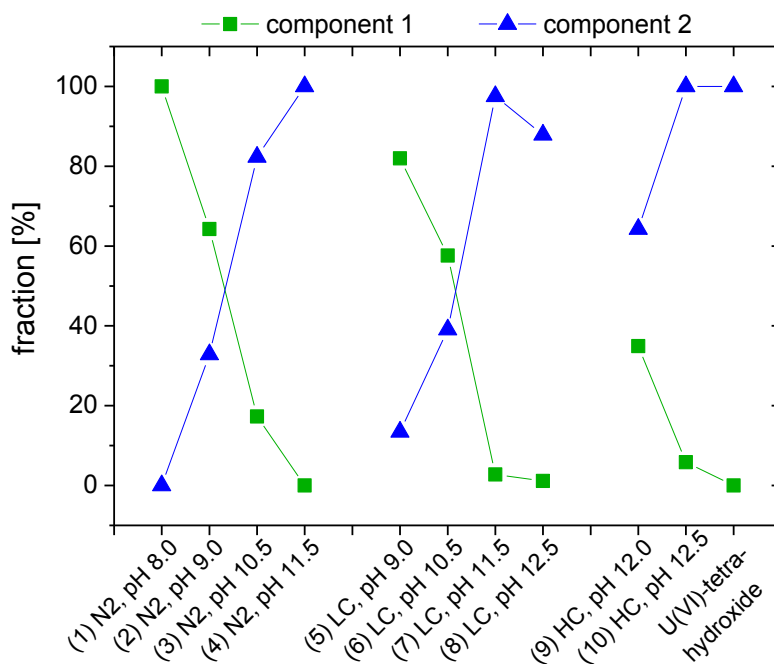
Figure 34: ITT calculated fractions of component 1 and component 2 for U(VI) sorption samples on Ca-bentonite in the absence of carbonate (N$_2$) and at low (LC) and high (HC) carbonate concentrations, including the reference of the aqueous UO$_2$(OH)$_4^{2-}$ complex (Moll et al., 2014).
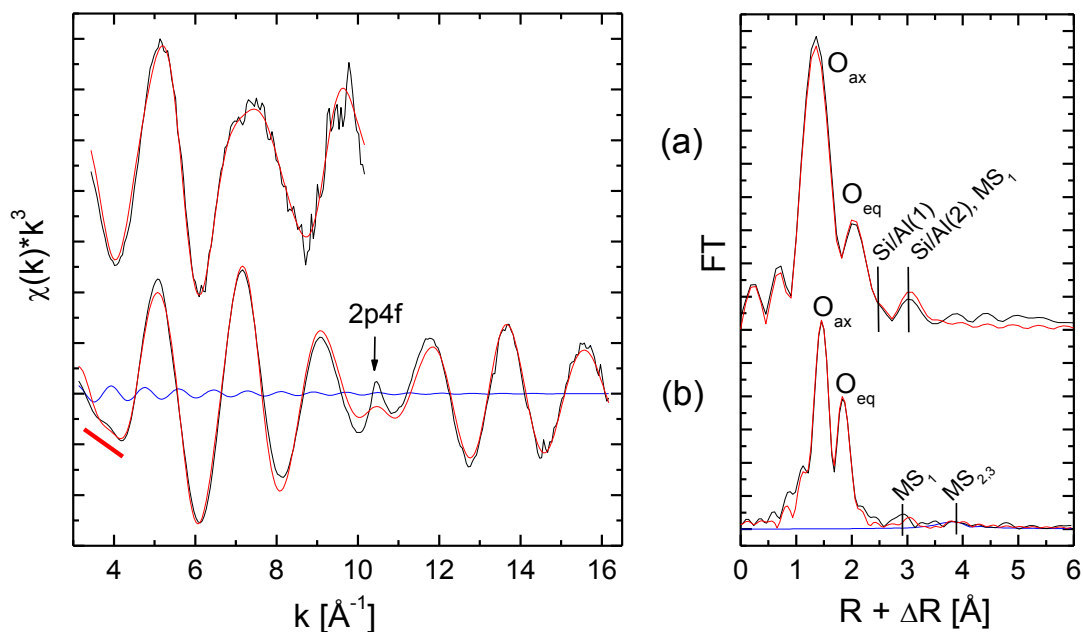
Figure 35: U L_{III}-edge EXAFS spectra of the ITFA isolated component 1 (a) and of the aqueous $UO_2(OH)_4^{2-}$ complex (b) (left) with corresponding Fourier transforms (FT) (right) together with the shell fit (red). Spectral contribution of MS_2 and MS_3 (blue). 2p4f multi-electron excitation assigned with arrow (Hennig, 2007).

For component 1 an equatorial oxygen shell (U-O_{eq}) at a distance of ~2.38 Å (*CN* fixed to 5) was obtained. This shortened distance in comparison to U-O_{eq} of hydrated outer-sphere sorption complexes on montmorillonite described in literature of ~2.43 Å (Chisholm-Brause *et al.*, 1994; Sylwester *et al.*, 2000) suggests the formation of inner-sphere surface complexes. Marques Fernandes *et al.* (2012) observed a splitting of the equatorial oxygen shell in sorption samples at pH 8 and obtained U-O_{eq} distances of ~2.3 Å and ~2.48 Å. Such a splitting cannot be resolved in the present study due to lower resolution in radial distances. However, when averaging the reported distances of Marques Fernandes *et al.* (2012), weighted by the coordination numbers (3.1 and 2.9), a mean U-O_{eq} distance of 2.387 Å can be derived, which is in excellent agreement with the results of the present study. Furthermore, two Si/Al shells could be fitted in radial distances of 3.11 Å and 3.32 Å. Those are in good agreement with the Si/Al distances of 3.09 Å and 3.28 Å for the bidentate inner-sphere sorption complexes on montmorillonite at pH 8 described by Marques Fernandes *et al.* (2012). Therefore, the same type of U(VI) surface complex is proposed for component 1.

Representative for component 2, the high symmetry of the $UO_2(OH)_4^{2-}$ complex leads to the appearance of a spectral feature at $k = 3.5 - 4.3$ Å^{-1} (Figure 35, highlighted with red line) which originates from the multiple scattering (MS) paths MS_2 (U-$O_{eq(1)}$-U-$O_{eq(2)}$) and MS_3 (U-$O_{eq(1)}$-U-$O_{eq(1)}$) (Figure Appendix 5). The scattering contribution of these inherent MS paths is strongly enhanced due to the linear arrangement of the involved atoms, comparable with the arrangement in the linear 'yl' chain of U(VI) for which the MS_1 (U-$O_{ax(1)}$-U-$O_{ax(2)}$) shows a

significant spectral contribution. Note that the 4-fold degenerated 3-legged MS path U-$O_{eq(1)}$-$O_{eq(2)}$ was also tested, but no further improvement of the fit was obtained. The sum of the MS_2 and MS_3 scattering contributions causes a truncation of the negative maximum of the EXAFS oscillation in this k-region (Figure 35). The distance of 4.55 Å measured for MS_2 and MS_3 matches, within the common error in determination of distances probed by EXAFS (Li $et\ al.$, 1995), the theoretically expected distance of 4.54 Å which would be twice the O_{eq} distance of 2.27 Å (Table 6). The O_{ax} and O_{eq} distances and the corresponding Debye-Waller factors (σ^2) are in good agreement with published data (Table 6) where the MS feature was not explored so that only the coordination number (CN) and/or the O_{eq} distance could be used for the structural interpretation of the aqueous $UO_2(OH)_4^{2-}$ complex (Moll $et\ al.$, 2000; Moll $et\ al.$, 2014). However, the error in determination of the CN is approximately 20% (Li $et\ al.$, 1995), hence the EXAFS determined CN is not reliable enough to be used as a proof for the presence of a 4-fold coordinated U(VI) complex. Thus, only the presence of the MS feature at $k = 3.5 -$ 4.3 Å^{-1} indicates univocally a symmetric 4-fold coordination of U(VI). Due to the appearance at low k-values, the MS feature is visible in the X-ray absorption near edge structure (XANES) at 17,240 eV. Therefore, XANES can be also used for the identification of a 4-fold coordination, as exemplary shown for the aqueous complexes of the 5- and 4-fold coordinated U(VI)-hydrate ($UO_2(H_2O)_5^{2+}$) and $UO_2(OH)_4^{2-}$, respectively (Figure Appendix 6).

The MS feature at $k = 3.5 - 4.3$ Å^{-1} is also present in case of the high pH sorption samples (Figure 32), which is in line with the ITFA result (Figure 34) pointing to the prevalence of a sorption complex with an $UO_2(OH)_4^{2-}$ like structure. In the case of 5-fold coordinated U(VI) the $O_{eq(1)}$-U-$O_{eq(2)}$ angles are not straight, so that the spectral contribution of MS_2 and MS_3 diminishes as observed for component 1 which covers the lower pH sorption samples. Thus, beside the fractions of the two sorption complexes the ITT shows also the transition from a 5-fold to a 4-fold coordination of U(VI) with increasing pH.

Despite the strong similarity with the aqueous $UO_2(OH)_4^{2-}$ complex according to the shell fit, it can be ruled out that component 2 corresponds to an aqueous species, as U(VI) was almost completely removed from solution and the EXAFS samples were prepared as wet pastes with only a minor amount of aqueous solution present. An aqueous species could therefore be present in the samples only as a minor fraction, while component 2 accounts for up to 100% in some of the samples. Consequently, component 2 can definitely be assigned to an adsorbed species. Furthermore, $UO_2(OH)_4^{2-}$ is expected to be the dominant aqueous species only at pH > 12, as confirmed by the TRLFS measurements (chapter 4.2.2). In the EXAFS samples between pH 10 and 12, $UO_2(OH)_3^-$ is the dominant aqueous species prior to sorption. Owing to the difficulty to obtain $UO_2(OH)_3^-$ as a single, isolated species, no EXAFS reference spectra exist for this complex. Its structure, especially the coordination number of equatorial oxygen, is not clarified. While sometimes referred to be 5-fold coordinated (3 OH and 2 H_2O), the DFT study of Ingram $et\ al.$ (2006) proposed a 4-fold coordination (3 OH and 1 H_2O). The finding of the present study of a 4-fold coordination of component 2 supports this

hypothesis. Apparently, this geometry is then preserved upon sorption, indicating relatively weak interaction with the substrate. Also the fact that it was not possible to fit U-Si/Al scattering paths for component 2 indicates a larger distance to the mineral surface. The complex could be bound via mediating cations such as Ca^{2+}, located between the negatively charged surface and the anionic uranyl hydroxide unit. Sorption of negatively charged uranyl species would then be realized by initial adsorption of Ca^{2+} to the clay mineral surface (Viallis-Terrisse *et al.*, 2001; Pointeau *et al.*, 2004; Gascó and Méndez, 2005; Missana and García-Gutiérrez, 2007), leading to a local charge inversion and facilitating attachment of anionic uranyl hydroxides. Also the formation of aqueous ternary Ca-uranyl-hydroxides is possible, which would have a neutral or even positive net charge and would be therefore capable of interacting with the negatively charged bentonite surface. The existence of such ternary Ca-uranyl-hydroxide complexes at (hyper)alkaline conditions is hypothesized but has not been explored yet in detail. The influence of calcium on U(VI) sorption on clay minerals is systematically and comprehensively investigated in chapter 4.4.

Table 6: Shell fit EXAFS structural parameters for component 1 and the aqueous $UO_2(OH)_4^{2-}$ complex.

Shell	CN	R [Å]	σ^2 [Å^2]	ΔE_0 [eV]
Component 1				
O_{ax}	2*	1.797(3)	0.0010(2)	11.0(5)
MS_1	/2	/3.594	/0.002	/11.0
O_{eq}	5*	2.382(8)	0.0154(8)	/11.0
Si/Al(1)	1.5(2)	3.11(1)	0.003[a]	/11.0
Si/Al(2)	1.2(2)	3.32(1)	0.003[a]	/11.0
aqueous $UO_2(OH)_4^{2-}$ complex				
O_{ax}	2*	1.8254(9)	0.00176(6)	3.6(3)
		1.83[b], 1.82[c]	0.001[b], 0.0015[c]	
MS_1	/2	/3.6508	/0.00352	/3.6
O_{eq}	4*	2.271(1)	0.0040(1)	/3.6
		2.25[b],	0.0043[b],	
		2.26[b], 2.27[c]	0.0046[b], 0.004[c]	
MS_2	/4	4.55(2)	0.005(3)	/3.6
MS_3	/4	/4.55	/0.005	/3.6

* - fixed parameter, / - linked parameter, CN − coordination number, R − radial distance, σ^2 − Debye-Waller factor, ΔE_0 − shift in energy threshold. The standard deviation of the fitted parameters is given in parentheses. Amplitude reduction factor $S_0^2 = 1.0$. Multiple scattering paths MS_1 ($U-O_{ax(1)}-U-O_{ax(2)}$), MS_2 ($U-O_{eq(1)}-U-O_{eq(2)}$), MS_3 ($U-O_{eq(1)}-U-O_{eq(1)}$). [a] - σ^2 fixed at value taken from literature (Hennig *et al.*, 2002; Marques Fernandes *et al.*, 2012), [b] - (Moll *et al.*, 2000), [c] - (Moll *et al.*, 2014).

Based on the knowledge obtained from EXAFS, also an assignment of the two species detected with site-selective TRLFS (chapter 4.2.4.2) to the structurally different surface complexes is possible. Assuming a $UO_2(OH)_4^{2-}$ like structure for component 2, a theoretical frequency for the symmetric stretch vibration can be calculated according to an empirical relationship for aqueous uranyl hydroxide complexes found by Nguyen-Trung *et al.* (2000). With four equatorial oxygens a v_s of 782 cm^{-1} is obtained, which is almost identical to the v_s of TRLFS-species 1 (781 cm^{-1}, Table 5). Accordingly, TRLFS-species 2, with a lower v_s of 758 cm^{-1}, has to correspond to the 5 fold-coordinated bidentate surface complex (EXAFS-component 1). This assumption is reasonable as a decrease of v_s (as a consequence of a weakening of the axial U-O bonds) is a response to an increased electron density and increased ligand bond strength in the equatorial plane (McGlynn *et al.*, 1961; Nguyen-Trung *et al.*, 2000; Tsushima, 2011; Di Pietro and Kerridge, 2016). For EXAFS-component 1 this is a result of the bidentate binding and the close proximity to substrate atoms (Si/Al) in contrast to EXAFS-component 2, where no backscattering contributions from the substrate could be detected. Due to extensive σ donation from the surface, Tsushima *et al.* (1998) and Morris *et al.* (1994) obtained similar values for v_s for inner-sphere surface complexes on silver nanoparticles (750 cm^{-1}) and smectite edge sites (751 cm^{-1}), respectively.

4.2.4.4. CTR/RAXR

CTR and RAXR were performed in order to gain further information about the spatial distribution of U(VI) at clay mineral surfaces at hyperalkaline condition. As the X-ray reflectivity measurements require a single crystal, the mica (001) surface was used as a structural analogue for clay minerals (mineral characteristics discussed in chapter 2.2). The idea was to test the hypothesis that calcium is mediating between the negatively charged surface and anionic uranyl hydroxides in solution. This could not be directly proven with EXAFS, as EXAFS-component 2, prevailing at hyperalkaline conditions, did not feature any backscattering contribution from the substrate (chapter 4.2.4.3), possibly due to an increased distance of adsorbed U(VI). As CTR/RAXR is a surface sensitive technique, it uncovers the distance of the resonant U(VI) to the mineral surface as well as the electron density between U(VI) and the surface, possible influenced by the presence of calcium.

Fitting of the integrated CTR data yields the total electron density above the surface. In Figure 36 the normalized electron density profiles of the U(VI) sorption samples at pH 11 in the presence and absence of 0.02 M CaCl$_2$, as well as a blank muscovite sample (absence of U(VI) in 0.1 M NaCl + 0.02 CaCl$_2$) are plotted. It is clearly visible that the peaks of the U(VI) sorption samples feature higher electron densities compared to the blank muscovite sample, meaning that U(VI) definitely approaches the crystal to some extent. However, the overall electron density is comparably low in all samples, indicating that the amount of sorbed U(VI) must be relatively small.
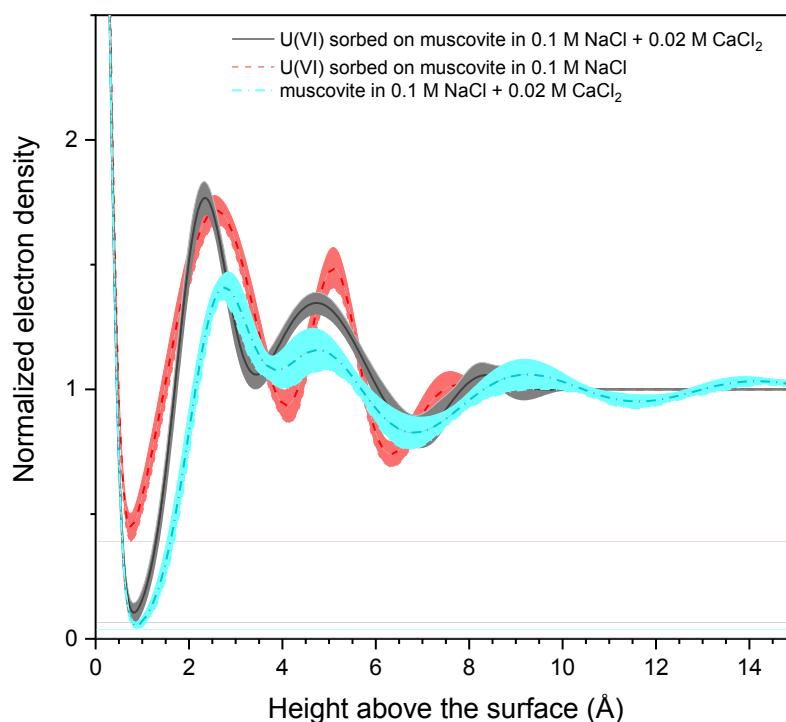
Figure 36: Electron density profile (normalized to the electron density of water) above the surface of the muscovite crystal of the U(VI) sorption samples ([U(VI)] = 5×10⁻⁵ M) in 0.1 M NaCl (grey solid line) and in 0.1 M NaCl + 0.02 M CaCl₂ (red dashed line). The blank sample without U(VI) (only muscovite crystal in 0.1 M NaCl + 0.02 M CaCl₂, blue dashed-dotted line) is included for comparison. Envelopes around the graphs indicate the margins of uncertainty.

Slight differences in the electron density of the sorption samples with and without calcium suggest the adsorption of calcium to the muscovite surface. In the presence of calcium, the first maximum at approx. 2.6 Å is noticeably narrowed in the presence of calcium, while the second maximum at approx. 5.1 Å is broadened. Both peaks are slightly shifted toward the surface. Compared to a muscovite sample in 0.03 M NaCl from Lee *et al.* (2012) especially the second maximum of both samples containing calcium (U(VI) sorption sample and blank) is closer to the surface, suggesting that the solution cation has greatest influence on the region at 4.7-5.1 Å above the surface. Without clearly associating the peaks of bulk electron density to adsorbed water or solution cations Na^+ or Ca^{2+}, it can be stated that the presence of different ions in the solution alters the electron density at the surface due to their adsorption. Depending on the adsorbed cation also the contribution of water to the electron density is influenced, caused by the different hydration behavior of sodium and calcium.

Integrated RAXR data, elucidating the contribution of the resonant U(VI) to the electron density, exhibit small but clear modulations around the L_{III} absorption edge in both U(VI) sorption samples at pH 11 (in the presence as well as in the absence of calcium). Representative for both, as the obtained data is very similar, in Figure 37a only the spectra of the sample in 0.1 M NaCl + 0.02 M CaCl₂ are shown. Noticeable modulations only appear at very low momentum transfer of 0.14, 0.19 and 0.24 Å⁻¹. This indicates a very broad distribution of U(VI) above the surface, i.e. a very variable adsorption height.
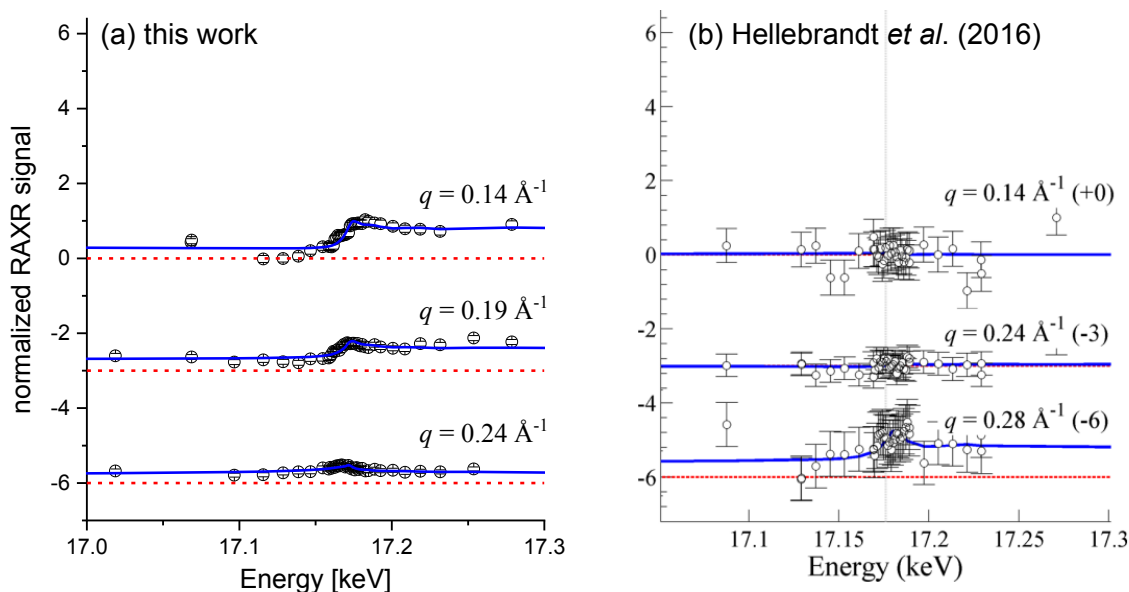
Figure 37: Selected RAXR data measured at the muscovite (001) basal plane at different fixed momentum transfer for the U(VI) sorption sample ([U(VI)] = 5×10⁻⁵ M) at pH 11 in 0.1 M NaCl + 0.02 M CaCl₂ of this work (a) and for a U(VI) sorption sample ([U(VI)] = 5×10⁻⁵ M) at pH 3.2 measured by Hellebrandt et al. (2016) (b). The deviation of the RAXR signal from the U(VI) free baseline (dashed red lines) is a result of adsorbed resonant U(VI). The blue lines display the model-independent fit of the data points and are included to guide the eye.

In a previous CTR/RAXR study of U(VI) sorption on the muscovite basal plane at acidic conditions and with a significantly higher concentration of U(VI) ([U(VI)] = $1×10^{-3}$ M) by Hellebrandt *et al.* (2016) (Figure 37b) no U(VI) was found to adsorb on the surface. This behavior is somewhat counterintuitive as at the chosen experimental conditions (pH 3.2) the cationic uranyl aquo ion dominates the aqueous speciation and should adsorb much better to a negatively charged surface than the anionic solution species prevailing at the very alkaline conditions (pH 11) of the present study. Hellebrandt *et al.* (2016) presumed that the size or the complex charge distribution of uranyl hindered its adsorption in comparison to other divalent cations. Alternatively, U(VI) sorption could be suppressed due to competition with an excess of sodium in solution. Experiments with plutonium revealed that a reduction to the tetravalent oxidation state was necessary for an effective interaction with the muscovite (001) surface. Possible reasons for the increased U(VI) retention in the present thesis could be the lower U(VI) solubility at alkaline conditions but also the fact that solution cations (Na^+, Ca^{2+}) at high pH do not act as competitors for anionic uranyl hydroxides, but maybe even as mediators.

A first approximation of the distribution of the resonant ions above the surface is provided by model-independent fitting of the RAXR data. Based on the output data of the model-independent fit (position, distribution width and integral area of the peaks in the electron density profile) it was attempted to build a model which reproduces the amplitude and phase of the modulations at different momentum transfer (Figure 38a). The corresponding electron density profile is depicted in Figure 38b. It should not be understood as definite structure but only represents one possible solution with satisfactory fit to the data points. The real

distribution of U(VI) above the surface could be different from that (e.g. exact height of the different species) but is expected to be similar. Refining the fit with model-dependent approaches is complicated by the very small number of measurements (data points for the fitting) with significant modulation. This is due to the particular spatial distribution of U(VI) in the samples. Moreover, additional optimization of the model is not worthwhile, as this would not affect the general outcome. U(VI) is very broadly distributed on the surface, resulting in a sharp drop in amplitude already at low momentum transfer (Figure 38a top). The corresponding flat and extremely broad peak of electron density is most likely a representation of U(VI) nanoparticles or surface precipitates. This is in line with the results from ATR FT-IR spectroscopy (chapter 4.2.4.1), where also predominantly surface precipitates or oligomeric U(VI) species were observed at a comparable initial U(VI) concentration (2×10^{-5} M). However, the phase of the RAXR modulations can only be satisfactory reproduced when introducing a second peak (species) to the model. This second peak is small, sharp, located in close proximity to the surface and supposedly represents adsorbed U(VI). Consequently, next to the predominant precipitation of U(VI) due to oversaturation at high pH at such 'high' initial U(VI) concentrations, also a small portion of U(VI) is adsorbed to the surface. Due to the overall low surface coverage, the exact configuration of the small amount of adsorbed U(VI) cannot be resolved. Therefore CTR/RAXR also does not allow to observe differences between the U(VI) adsorption in the presence and in the absence of calcium at very low U(VI) concentrations. Nonetheless, the measurement confirmed the retention mechanisms occurring when applying super-micromolar U(VI) concentrations. Furthermore, for the first time U(VI) was measured on an muscovite (001) surface with CTR/RAXR.
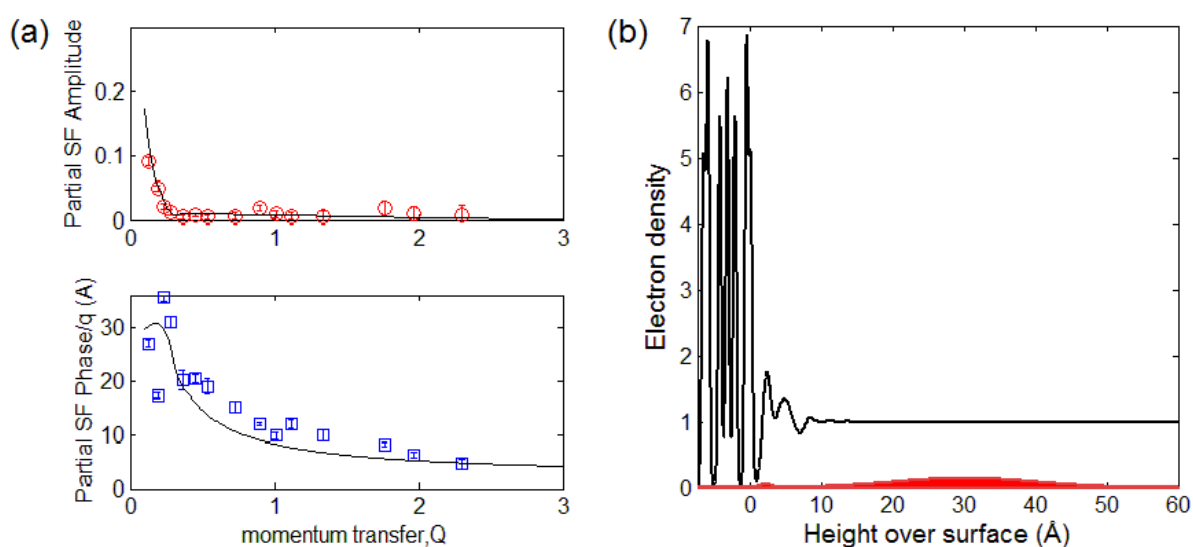

Figure 38: Based on the model-independent fitting of the RAXR data of the U(VI) sorption sample at pH 11 in 0.1 M NaCl + 0.02 M CaCl$_2$ the data points for amplitude and phase (a) were approximated with a model for the resonant part of electron density (normalized to the electron density of water) above the surface (b).

4.3. Influence of ISA on U(VI) sorption on Ca-bentonite

The results presented in this chapter were generated in the course of a master thesis "Untersuchungen zum Einfluss von Isosaccharinsäure auf die U(VI)-Rückhaltung an Ca-Bentonit unter alkalischen Bedingungen" by Paul Dullies (Dullies, 2019), embedded within the works of the BMWi project GRaZ (Geochemische Radionuklidrückhaltung an Zementalterationsphasen) and the European project MIND (Microbiology in nuclear waste disposal). PhD students Thimo Philipp (GRaZ) and Hannes Brinkmann (MIND) were responsible for planning, supervision and evaluation of the master thesis.

Goal of the work was to investigate the ability of small organic molecules, i.e. isosaccharinic acid (ISA) (chemical structure of α-D-isosaccharinic acid shown in Figure 39) to increase the mobility of U(VI) in an alkaline repository environment. This could be realized by complexation of ISA with U(VI), forming stable aqueous species, thus, preventing U(VI) to adsorb to mineral surfaces. Therefore, U(VI) batch sorption experiments at different ISA concentrations were complemented with spectroscopic investigations (i.e. TRLFS) on the aqueous speciation of U(VI) in the presence of ISA.

At U:ISA ratios of 1:10, 1:100 (both not shown) and 1:1,000 (Figure 39) no effect of ISA on U(VI) retention could be observed. The pH-dependent U(VI) sorption on Ca-bentonite follows the same trend as described in chapter 4.2.1.4, with very strong sorption at pH 8-12, followed by a decrease in U(VI) retention at pH > 12. This is in contrast to existing studies at lower pH, where a lower excess of ISA already led to U-ISA complexation and to an associated decrease of U(VI) retention. At pH 7 Baston *et al.* (1994) observed significant reduction of U(VI) sorption on tuff rock at a U:ISA ratio of 1:250 and Warwick *et al.* (2006) described the formation of aqueous U-ISA complexes even at an ISA excess smaller than 1:20. At acidic conditions also Brinkmann *et al.* (2019) found different aqueous U-ISA complexes at very small excess of ISA (U:ISA = 1:16). However, in the alkaline pH range investigated in this study (pH 8-13) uranyl hydrolysis seems to be too strong for readily allowing interaction between U(VI) and ISA. This was confirmed by TRLFS measurements (not shown), where at a U:ISA ratio of 1:1000 no deviation from reference system without ISA could be observed.

Even at a U:ISA ratio of 1:10,000 the sorption behavior was still the same as in the experiment without ISA (see Dullies (2019)). Only at a U:ISA ratio of 1:100,000 (which was the highest excess of ISA achievable with the available stock solutions) a significant effect on U(VI) retention could be detected (Figure 39). Sorption is only at 52% and 41% at pH 8 and 9, respectively. At pH 10, the sorption maximum, U(VI) is retained to 83%, which is still a significant reduction compared to the complete retention in the absence of ISA. At pH > 10, retention decreases gradually, consistently exhibiting smaller values than in the absence of ISA.
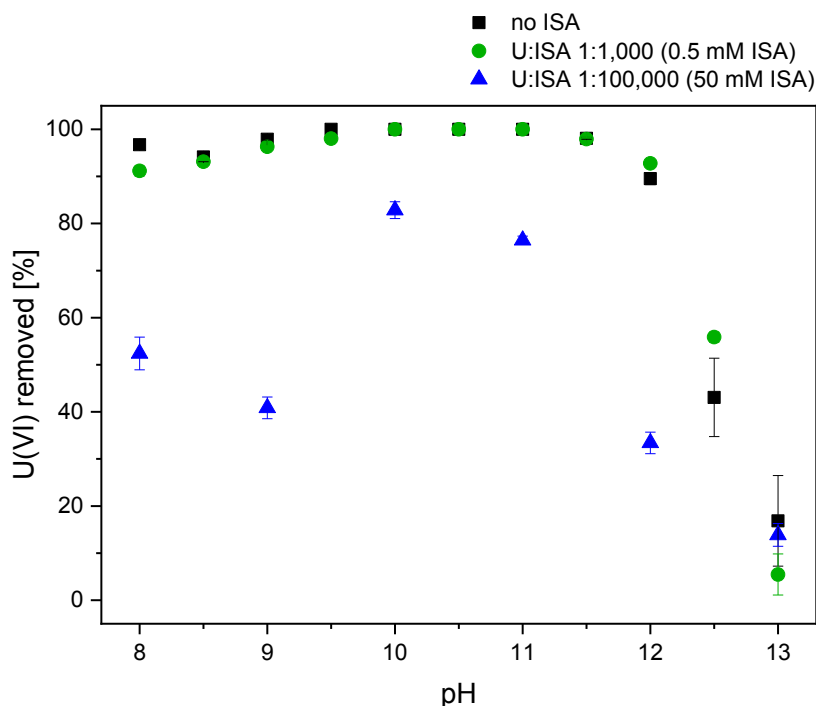
Figure 39: Percentage of U(VI) ([U(VI)] = 5×10⁻⁷ M) sorbed on Ca-bentonite (10 g/L) in 0.1 M NaCl as function of pH and U:ISA ratio in the absence of CO₂. Above the graph, the chemical structure of α-D-isosaccharinic acid is depicted.

TRLFS measurements of the supernatant solutions of the sorption experiments with an U:ISA ratio of 1:100,000 prove, that the decrease of U(VI) retention is caused by complexation of U(VI) with ISA. All luminescence spectra obtained between pH 8 and 13 (Figure 40) differ from the spectra obtained for the uranyl hydroxide complexes in the absence of ISA (not shown). Based on the position of the peaks, two species can be distinguished within the investigated pH range: One at pH 8-10 and another one at pH 11-13. The peak positions of species 1 (approx. 481, 502 and 523 nm) fit very well to the 1:2 U-ISA complex $UO_2(ISA)_2$ (Table 7). By combination of UV-Vis, ATR FT-IR, EXAFS and ESI-MS Brinkmann *et al.* (2019) showed that this complex forms in aqueous solution, provided ISA is present in excess of U(VI). A TRLFS spectrum of this complex was recorded and serves as a reference. So far $UO_2(ISA)_2$ was only observed in acidic solutions. The present work suggests, that it also occurs at up to pH 10 at extreme excess of ISA (U:ISA = 1:100,000). Species 2, which was observed at pH 11-13, is significantly shifted to lower wavelength and could not be assigned to a specific U-ISA species within the scope of this work. Due to an increased concentration of OH^- in hyperalkaline solutions, species 2 might be a mixed U-ISA-OH complex. Warwick *et al.* (2006) proposed the formation of $UO_2ISA(OH)_4$ at pH 13.3 based on the solubility product method (Warwick *et al.*, 2004).

Even though it was shown that U(VI) retention on Ca-bentonite is significantly reduced between pH 8 and 13 at an U:ISA ratio of 1:100,000 due to aqueous complexation of U(VI) and ISA, it can be concluded that U(VI) mobilization by the introduction of ISA is not a major threat at alkaline repository conditions. Justification for this assumption arises from the

great improbability of encountering such a high excess of ISA in deep geological repository environments. The maximum concentration of ISA that might be present in such a repository is estimated to be 3×10^{-6} M (Wieland and Van Loon, 2003). This conclusion is in accordance with results on mobilization of other radionuclides by the introduction of cellulose degradation products. Th(IV), Eu(III) and Am(III) were found to sorb less on calcite at pH 13.3 only at ISA concentrations above 1×10^{-5} M (Tits *et al.*, 2005). This corresponded to very high excess ratios of Th:ISA = 1:1,000,000, Eu:ISA = 1:10,000 and Am:ISA = 1:1,000,000.
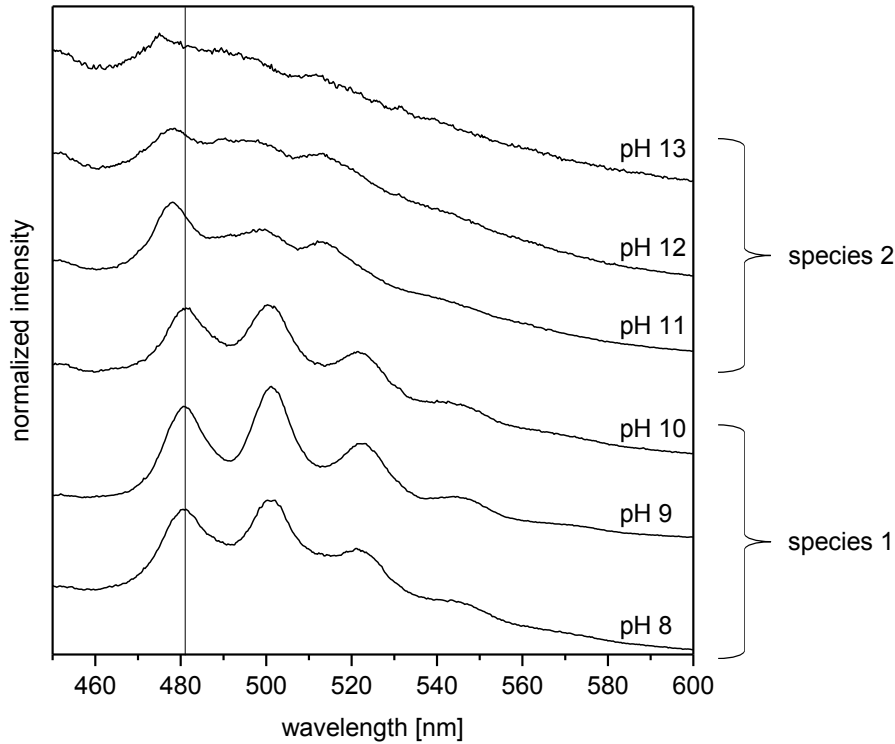
Figure 40: Luminescence spectra of uranyl ([U(VI)] = 5×10^{-7} M) in the supernatant of the sorption experiment with a U:ISA ratio of 1:100,000 in 0.1 M NaCl as a function of pH in the absence of CO_2.

Table 7: Positions of the first three main peaks of the luminescence spectra of uranyl in the supernatant of the sorption experiment with a U:ISA ratio of 1:100,000. [$UO_2(ISA)_2$], measured by Hannes Brinkmann, is included as a reference.

Experiment	pH	Peak positions [nm]		
Supernatant after	8	480.6	501.5	523.4
sorption experiment	9	480.9	501.2	523.4
with U:ISA 1:100,000	10	481.5	501.8	522.2
	11	478.1	499.7	514.5
	12	477.5	496.3	513.5
	13	473.2	499.7	512.9
[$UO_2(ISA)_2$]		482	502	523

4.4. Influence of calcium on U(VI) and Np(VI) sorption on clay minerals

The groundbreaking outcome of the experiments on U(VI) sorption on Ca-bentonite at (hyper)alkaline conditions (chapter 4.2) was that the predominant retention mechanism between pH 10 and 12 under the given conditions was adsorption despite the anionic character of prevailing aqueous species. It was hypothesized that the attachment to the negatively charged mineral surface could be mediated by calcium, of which large amounts were present in the background electrolyte. Possible mechanisms involve the formation of aqueous ternary Ca-U-OH complexes, which do not feature a negative net charge, allowing for interaction with the mineral surface. The existence of such complexes was so far only hypothesized but has never been investigated. Another plausible mechanism is the adsorption of calcium to the mineral surface in the first place, creating local positively charged sites, where the actinyl hydroxides can attach. In order to prove this hypothesis, this chapter is dedicated to the careful evaluation of the effect of calcium on An(VI) sorption on clay minerals. It encompasses the study of calcium sorption on Ca-bentonite (and its effect on the surface charge of Ca-bentonite) (chapter 4.4.1), the influence of calcium on batch sorption of U(VI) (chapter 4.4.2.1) and Np(VI) (chapter 4.4.3) on different clay minerals, and the spectroscopic identification of such calcium-induced U(VI) sorption complexes with site-selective TRLFS (chapter 4.4.2.2).

4.4.1. Ca(II) sorption on Ca-bentonite at (hyper)alkaline conditions

The sorption of calcium on Ca-bentonite was investigated in batch sorption experiments as a function of S/L ratio and pH. The initial calcium concentration of 2×10^{-4} M, spiked with 1×10^{-12} M ^{45}Ca was chosen based on estimations for a monolayer saturation of the bentonite surface with calcium cations according to literature values for montmorillonite surface site density of 2×10^{-5} mol/g (Wieland *et al.*, 1994). The amount of calcium removed from the solution was determined by LSC of ^{45}Ca.

The batch experiments as a function of S/L ratio prove that calcium strongly adsorbs to the Ca-bentonite surface, when sufficient sorption sites (i.e. high enough mineral mass) are provided (Figure 41a). Calcium sorption increases rapidly from 34% at 0.2 g/L to more than 90% at 2 g/L, reaching a plateau of approx. 95% sorption. A maximum surface capacity for calcium of 3.41×10^{-4} mol/g can be derived from the sorption at 0.2 g/L. Assuming that adsorbed Ca^{2+} occupies two surface sites, this corresponds to a surface site density of 6.82×10^{-4} mol/g, being considerably higher than the value given by Wieland *et al.* (1994), but very close to the cation exchange site density of MX-80 bentonite of 6.96×10^{-4} mol/g, assumed by Grambow *et al.* (2006). Based on these results, a S/L ratio of 10 g/L (also used for the U(VI) sorption experiments with Ca-bentonite) was chosen for the pH-dependent sorption experiments, in order to provide enough sites for unrestricted calcium adsorption. Under these conditions sorption of calcium was very high in the whole investigated pH range 8-13 (Figure 41b). A weak dependency on pH can be observed, as sorption is increasing with

increasing pH from 88% at pH 8 to a maximum of 97% at pH 11. This corresponds to a maximum $\log(K_d)$ value of 3.47 log(L/kg). The slight decrease to 86% sorption at pH 13 could be due to beginning dissolution of minerals, as described in chapter 4.1.3.

Strong sorption of Ca^{2+} or Sr^{2+} (which can be regarded as chemical analogue) has been observed previously already on bentonite (Missana and García-Gutiérrez, 2007; Missana *et al.*, 2008; He *et al.*, 2016; Cherian *et al.*, 2018), muscovite (Schlegel *et al.*, 2006; Fenter *et al.*, 2007) and kaolinite (Chen *et al.*, 2014). Predominant retention mechanism is cation exchange, which is largely independent of pH, but highly sensitive to ionic strength, according to the reaction

$$z_B A \equiv X \; + z_A B = z_A B \equiv X \; + z_B A \tag{14}$$
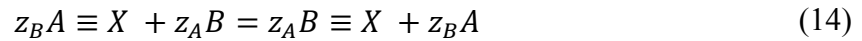
where B is a cation (i.e. Ca^{2+}) with charge z_B, which exists in the aqueous phase, and A is a cation (e.g. H^+ or Na^+), with charge z_A, at the clay surface ($\equiv X$) (Missana and García-Gutiérrez, 2007). A contribution of surface complexation to the retention of calcium was only significant at pH > 8. Missana and García-Gutiérrez (2007) were only able to model an increase in calcium (M^{z+}) sorption from pH 8 to 10 by the introduction of a surface complex on the amphoteric edge sites (SOH) of the clay mineral according to the following reaction

$$SOH + M^{z+} \; \leftrightarrow SOM^{z-1} + H^+ \tag{15}$$
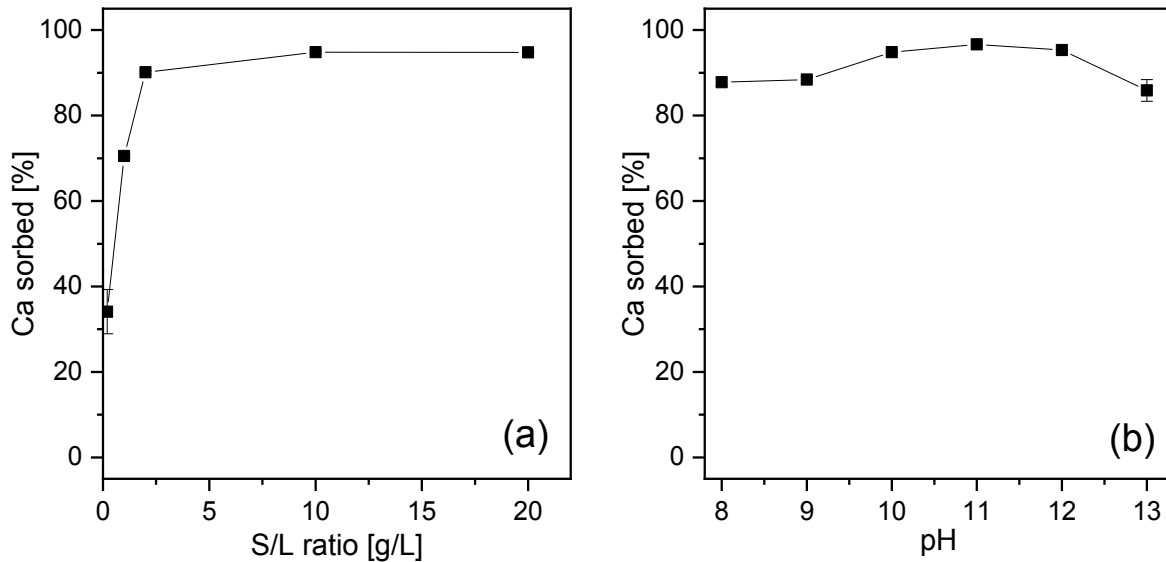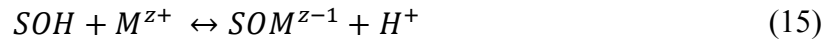
Figure 41: Sorption of calcium (2×10^{-4} M spiked with 1×10^{-12} M ^{45}Ca) on Ca-bentonite in the absence of CO_2 as a function of S/L ratio (pH 10) (a) and as a function of pH (S/L ratio = 10 g/L) (b).

At high pH, surface complexation is promoted due to the successive deprotonation of the clay mineral surface ($SOH \leftrightarrow SO^- + H^+$). Accordingly, Schlegel *et al.* (2006) and Fenter *et al.* (2007) also observed a contribution of surface complexation to calcium and strontium adsorption on the mica 001 surface, expressed in the fact that the hydration shell was partly removed. Based on these findings, surface complexation is also assumed to contribute significantly to the strong calcium retention at pH 8-13 observed in the present study.

Further evidence for the adsorption of calcium on the Ca-bentonite surface arises from the measurement of zeta potential with added $CaCl_2$. Compared to the measurement in 0.1 M NaCl (chapter 4.1.1), the addition of 0.02 M calcium results in a much less negative surface charge over the entire investigated pH range 7-13 (Figure 42). Even though the presence of calcium does not result in a complete reversal of surface charge, negative surface charge is partly compensated, leading to potentials of approx. -15 mV at pH 7-11 and between -15 and +2 mV at pH 11-13. As the measurement of zeta potential is a bulk technique, measuring the average charge of all existing surface sites, partial compensation of negative surface charge implies the existence of locally positively charged sites where calcium is adsorbed. Beside the effect of calcium, also the influence of strontium on the surface charge was tested. Assuming that the charge of the cation is the main driving factor, the adsorption of Sr^{2+} should be similar to the one of Ca^{2+}. In fact, in 0.1 M NaCl + 0.02 M $SrCl_2$, the surface charge at pH 7-13 is almost identical to that in 0.1 M NaCl + 0.02 M $CaCl_2$ (Figure 42). That means, both divalent cations Ca^{2+} and Sr^{2+} obviously have the same charge compensating effect.
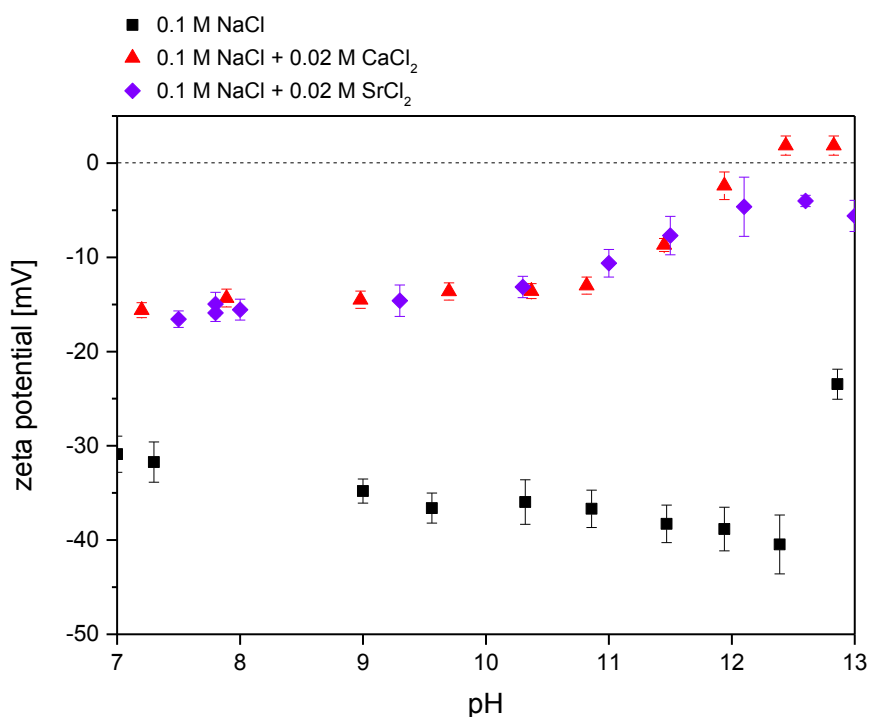
Figure 42: Surface potential of Ca-bentonite (0.1 g/L) as a function of pH and background electrolyte.

Similar impact on surface charge due to adsorption of calcium at alkaline conditions has been previously reported for different types of bentonite (Ho and Handy, 1963; Cherian *et al.*, 2018), kaolinite (Atesok *et al.*, 1988; Farooq *et al.*, 2011) and cementitious material (Viallis-Terrisse *et al.*, 2001; Pointeau *et al.*, 2006), where even an reversal of charge was observed.

Both zeta potential measurements and Ca batch sorption experiments have shown that calcium adsorbs strongly to the Ca-bentonite surface and consequently, potentially generates alternative sorption sites for anionic actinyl hydroxides. The resulting calcium-induced changes in U(VI) and Np(VI) sorption behavior are investigated in the following chapters.

4.4.2. Effect of Ca on U(VI) sorption on montmorillonite, kaolinite and muscovite

As all previous U(VI) sorption experiments (on Ca-bentonite in diluted Gipshut solution) were conducted in the presence of calcium, the aim was to perform similar experiments, but with the exclusion of calcium. For that purpose, suspensions were prepared in NaCl background solutions and the minerals Na-montmorillonite, synthetic kaolinite and muscovite were chosen, which supposedly do not contain any calcium that could be leached during the experiment. Assuming that calcium is responsible for enabling sorption of anionic uranyl hydroxide complexes, U(VI) retention is expected to be radically decreased in these experiments between pH 10 and 12 compared to the results presented in chapter 4.2.

4.4.2.1.   Batch sorption experiments

U(VI) sorption on Na-montmorillonite

Figure 43 shows the batch sorption of U(VI) on Na-montmorillonite between pH 8 and 13 in the absence of CO_2 (a) and at low carbonate concentration (1 mM) (b), both in 0.1 and 2.6 M NaCl. The pH-dependent sorption on Ca-bentonite in diluted Gipshut solution (see chapter 4.2.1.4) is included in the diagrams for comparison. In the absence of CO_2 the U(VI) sorption on Na-montmorillonite is extremely high up to pH 12, followed by a sharp decrease (Figure 43a). This behavior is very similar to the U(VI) sorption on Ca-bentonite. The slightly lower retention at pH 8-9 in the experiments with Ca-bentonite could be a result of small fractions of (calcium) uranyl carbonate complexes which might be forming due to release of minimal amounts of carbonate from the Ca-bentonite. Most significant difference between the sorption curves is the earlier decrease in retention with increasing pH in the series with 0.1 M NaCl. While sorption at pH 12 in 2.6 M NaCl is still at 95%, it has dropped to 52% in 0.1 M NaCl. This behavior can be explained with the ionic strength dependency of U(VI) hydrolysis. With increasing ionic strength, the formation of highly charged species is hampered, meaning that at $I = 2.6$ M the 1:4 hydrolysis species $UO_2(OH)_4^{2-}$, to which the decrease in U(VI) retention is attributed, gains predominance over the 1:3 complex only at higher pH, compared to the low ionic strength case. The U(VI) retention at pH 10-12 remains virtually unchanged

compared to the experiments with Ca-bentonite in diluted Gipshut solution, so that it has to be stated, that the intended reduction of calcium concentration (in solution as well as in the mineral) caused no effect. However, ICP-MS measurements revealed the presence of 3.6×10^{-5} M calcium at pH 11 in the supernatant after the experiments. This must arise from calcium impurities in the structure of Na-montmorillonite due to insufficient Ca-removal in the purification process. Chemical analysis of the purified clay still showed a CaO fraction of 1.00 ± 0.24 weight-% (Fritsch, 2018). Apparently, such low calcium concentrations are sufficient to sustain a complete U(VI) sorption between pH 10 and 12.

Similarly, also at low carbonate concentration no significant deviations from the U(VI) sorption on Ca-bentonite in diluted Gipshut solution could be observed at pH > 10 at reduced amount of dissolved calcium. However, at pH 8-9.5, clear differences appear (Figure 43b). Sorption on Na-montmorillonite in NaCl solutions is much higher in this pH range, ranging between 59 and 68% at pH 9, compared to 27% on Ca-bentonite in diluted Gipshut solution. The reason for this increased U(VI) retention is most probably that the formation of ternary calcium uranyl carbonate complexes is strongly suppressed at very low calcium concentrations. Such ternary calcium uranyl carbonate complexes have even a weaker tendency to adsorb to mineral surfaces compared to $UO_2(CO_3)_3^{4-}$ (Meleshyn *et al.*, 2009; Richter *et al.*, 2016).
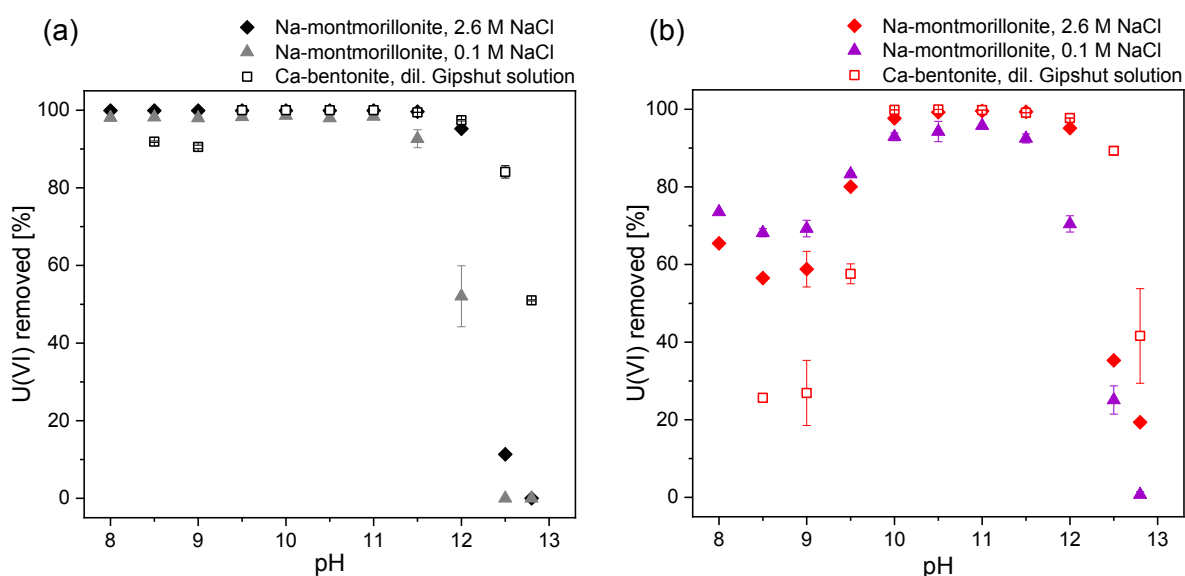
Figure 43: Percentage of U(VI) sorbed on Na-montmorillonite (10 g/L) in 2.6 M and 0.1 M NaCl as function of pH in the absence of CO_2 ($[U(VI)] = 5 \times 10^{-7}$ M) (a) and at low carbonate concentration (1 mM) ($[U(VI)] = 1 \times 10^{-6}$ M) (b). The U(VI) sorption on Ca-bentonite is shown for comparison (see chapter 4.2.1.4).

U(VI) sorption on kaolinite

The U(VI) retention was tested on selected samples of synthetic kaolinite, of which only a very limited amount of sample material was available. Experiments were performed at pH 10, 11, 12 and 12.7 both in 0.1 M NaCl and 0.1 M NaCl + 0.02 M CaCl$_2$ (Figure 44a). In contrast to the experiments with Na-montmorillonite, the sorption of U(VI) on kaolinite is decreasing dramatically at pH ≥ 10 in the absence of calcium, compared to the experiments on Ca-bentonite in diluted Gipshut solution. At pH 12 sorption reaches 0%, supporting the hypothesis that high U(VI) retention at pH 10-12 cannot be sustained in the absence of calcium. Measured calcium concentrations in the supernatant after the sorption experiment were as low as 4×10^{-6} M. This seems to be sufficiently low to prevent U(VI) sorption to the mineral surface at hyperalkaline conditions due to Ca-mediation. Technically, according to SEM-EDX the synthetic kaolinite did not contain any calcium at all (Huittinen *et al.*, 2010). However, trace amounts are beyond the sensitivity of the method. Alternatively, the origin of calcium in the supernatant (close to ICP-MS detection limit) could be due to contamination of laboratory equipment such as the pH electrode, or impurity of the NaCl electrolyte.

Experiments with added CaCl$_2$ serve to check if the decreased U(VI) retention is really associated to the lower calcium concentration or rather to the different mineral structure of kaolinite compared to montmorillonite. In 0.1 M NaCl + 0.02 M CaCl$_2$, U(VI) sorption on kaolinite is very high up to pH 12.7 (Figure 44a). No drop in retention with increasing pH can be observed. Therefore, it can be unequivocally concluded that the presence of calcium significantly enhances U(VI) retention between pH 10 and 13 by mediating between anionic aqueous uranyl hydroxide complexes and the negatively charged mineral surface.
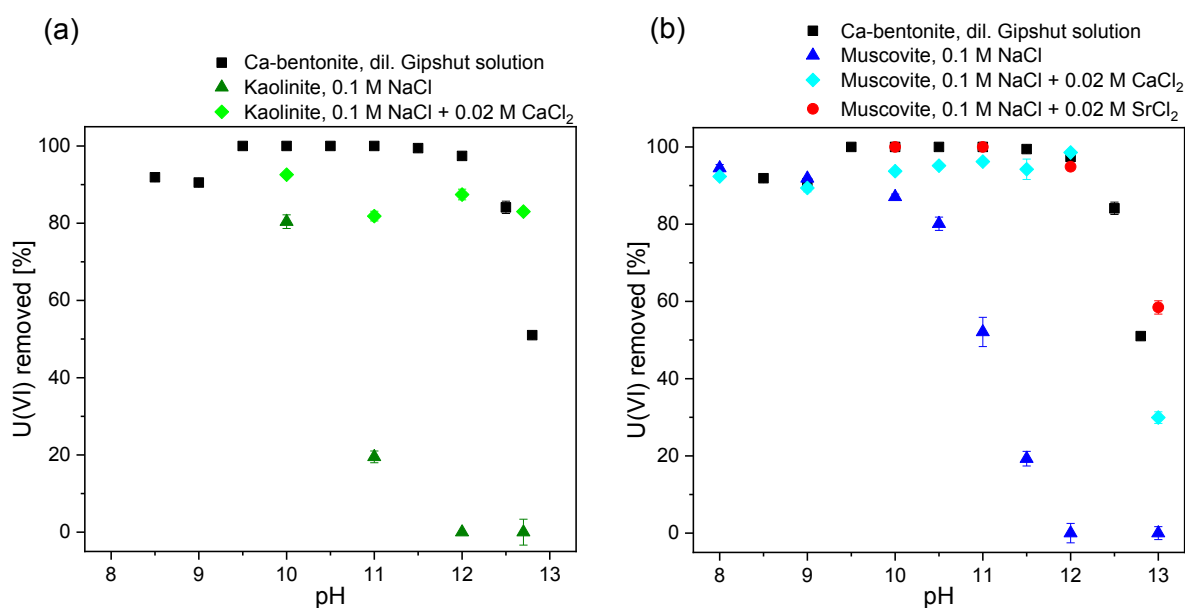
Figure 44: Percentage of U(VI) ([U(VI)] = 5×10^{-7} M) sorbed on synthetic kaolinite (0.5 g/L) (a) and muscovite (3 g/L) (b) in 0.1 M NaCl, 0.1 M NaCl + 0.02 M CaCl$_2$ and 0.1 M NaCl + 0.02 M SrCl$_2$ as function of pH in the absence of CO$_2$. The U(VI) sorption on Ca-bentonite is shown for comparison (see chapter 4.2.1.4).

U(VI) sorption on muscovite

As a clay mineral analogue, also muscovite was studied regarding its retention potential towards U(VI) at pH 8-13 in 0.1 M NaCl and in 0.1 M NaCl + 0.02 M CaCl$_2$. Figure 44b shows that the sorption behavior is indeed comparable to the one on kaolinite. In 0.1 M NaCl U(VI) sorption decreases first slowly at pH > 8 and then rapidly at pH ≥ 10, until reaching 0% at pH 12. Measured calcium concentrations in the solution were approx. 6.3×10^{-6} M. Although being slightly higher than in the experiments with kaolinite, they are still low enough to not allow substantial U(VI) mediation to the mineral surface.

The experiments with addition of CaCl$_2$ exhibit an extremely high U(VI) sorption up to pH 12 and follow essentially the same trend as sorption experiments on Ca-bentonite and Na-montmorillonite (Figure 44b). Again, as for kaolinite, this suggests that the low retention at pH ≥ 10 in 0.1 M NaCl is not a consequence of the different mineral structure but merely of the lack of calcium availability.

As zeta potential measurements (chapter 4.4.1) have shown that strontium adsorbs to Ca-bentonite exactly as calcium, a complementary pH-dependent U(VI) sorption experiment was conducted in 0.1 M NaCl + 0.02 M SrCl$_2$, in order to investigate if strontium can have the same sorption mediating effect on U(VI). Indeed in the presence of strontium an almost identical U(VI) sorption behavior was observed, with very high retention up to pH 12 (Figure 44b). Consequently, the effect of enabling U(VI) adsorption is not attributed to exclusive properties of calcium but to the charge of divalent cations in general.

Effect of calcium concentration on U(VI) sorption & discussion of underlying mechanisms

The batch sorption experiments with Ca-bentonite, Na-montmorillonite, synthetic kaolinite, and muscovite in different background electrolytes demonstrate that certain amounts of dissolved calcium are sufficient to enable U(VI) sorption at pH 10-12, while others are not. Figure 45 summarizes measured calcium concentrations in the supernatant after the sorption experiment and respective percentage of U(VI) sorption of the different previously described batch sorption experiments at pH 11. More reasonable measures for the role of calcium would be the calcium concentration in solution prior to sorption, or even better, the amount of calcium that adsorbed to the surface, displaying possible sorption sites. However, both cannot be determined independently as leached calcium readily adsorbs to the mineral surface. As demonstrated by Figure 45 the concentration of calcium in the supernatant after the experiment is a good enough measure for its availability during the experiment and the connected potential to enhance U(VI) sorption. It is evident that fairly low calcium concentrations are sufficient to obtain very strong U(VI) sorption. While retention is only at 19% in the presence of 4×10^{-6} M calcium, it is already quantitative at 3.6×10^{-5} M calcium. The minimum calcium concentration that is required to achieve complete U(VI) retention

under the given conditions lies somewhere between 6.3×10^{-6} M (on muscovite in 0.1 M NaCl) and 3.6×10^{-5} M (on Na-montmorillonite in 0.1 M NaCl). At higher calcium concentrations (up to 0.022 M) U(VI) sorption remains at a constantly high level close to 100%. It has to be mentioned that the experiments summarized in Figure 45 are not perfectly comparable because the various minerals have different specific surface areas and also applied S/L ratios were different. Nevertheless, the correlation between sorption percentage and calcium detected in the supernatant is striking, implying that the calcium concentration can be assumed to be the dominating factor.

Bridging of a metal to a mineral surface is known from so called type B ternary surface complexes (Hubbard, 2002; Bradl, 2005). Such ternary type B surface complexes have the configuration surface $\equiv$ ligand $-$ metal and form by coordination of a metal to a sorbed ligand. In the present study, the mechanism is similar but the configuration is different. In contrast to type B surface complexes, the metal (U(VI)) is not bridged via the ligand (OH) but via an additional metal cation (Ca^{2+}). This could be described as quaternary surface complex (surface $\equiv Ca^{2+} - UO_2(OH)_3^-$). Due to their complexity, quaternary systems have not been studied thoroughly so far and very few studies are published dealing with similar systems. Commonly accepted textbook knowledge about surface complexation is restricted to simple coordination of the metal to the surface and to ternary surface complexation. Moreover, conventionally the adsorption of ions to surfaces of opposite charge is studied. Sorption of anionic actinide complexes to a negatively charged surface, as observed in the present work, displays a rarely considered scenario.
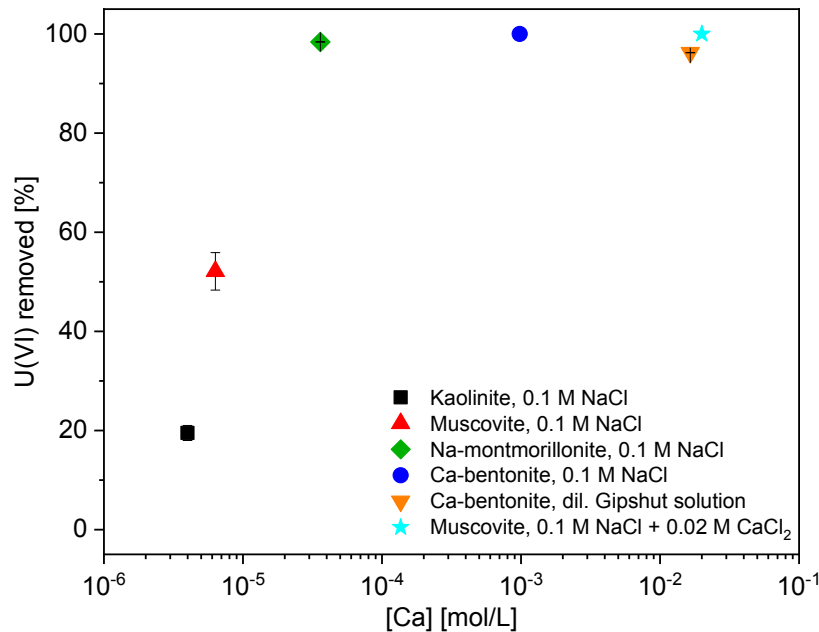

Figure 45: Percentage of U(VI) ([U(VI)] = 5×10^{-7} M) sorbed on Ca-bentonite (10 g/L), Na-montmorillonite (10 g/L), muscovite (3 g/L) and kaolinite (0.5 g/L) at pH 11 as a function of calcium concentration measured in the supernatant after the sorption experiments in the absence of CO_2.

A small number of studies already pointed out the potential of calcium to enhance anion retention. Allen *et al.* (2019) and Griffin *et al.* (2016) described a calcium bridging between the anionic surfactant bis(2-ethylhexyl) sulfosuccinate and mica surfaces. The bridging effect was achieved with low concentrations of divalent cations and was absent in monovalent electrolyte solutions. Arnarson and Keil (2000) found an increased sorption of natural organic matter to montmorillonite due to calcium bridging. For Np(V) and Np(VI) Tits *et al.* (2014) obtained higher retention on TiO_2 in the presence of calcium at pH 13.3. The K_d value of Np(VI) increased by two orders of magnitude upon introduction of 10^{-5} M calcium. As possible explanations, the authors suggested neutralization of negative surface charge or formation of very strong surface stabilized Ca-neptunate complexes, and stated that additional experiments, especially spectroscopic measurements, are necessary to draw conclusions about the retention mechanisms.

No peer-reviewed publication exists about a potential bridging effect of calcium on U(VI) adsorption. However, in the batch sorption data of the PhD theses of both Andreas Schnurr (Schnurr, 2015) and Natalia Mayordomo (Mayordomo, 2017) an increased U(VI) sorption at very alkaline conditions in the presence of calcium is visible. Schnurr (2015) noticed a difference between U(VI) sorption on Illite du Puy in NaCl and $CaCl_2$ at pH 10-12. Mayordomo (2017) was able to model high U(VI) sorption on smectite at pH 9.5-10 only by introduction of a calcium mediated surface complex S^WO-Ca-$UO_2(OH)_3$. The batch sorption results of the present study also suggest such calcium-mediated surface complexes. However, no spectroscopic evidence for the existence of such complexes exists so far. Therefore, site-selective TRLFS measurements on sorption samples were performed (chapter 4.4.2.2).

4.4.2.2. Site-selective TRLFS of Ca-induced U(VI) surface complexes

Solids of muscovite and kaolinite with sorbed U(VI) were investigated at different pH and in different electrolyte solutions (as described in chapter 3.5) in order to be able to detect different sorption species, which either form in the absence or exclusively in the presence of calcium. For muscovite at pH 11 and kaolinite at pH 10, both in 0.1 M NaCl, 'regular' surface complexes are expected, as U(VI) batch sorption was still sufficiently high in the absence of calcium (chapter 4.4.2.1). For muscovite at pH 11 in 0.1 M NaCl + 0.02 M $CaCl_2$ a combination of 'regular' and calcium-induced sorption complexes is supposed. Finally, both for muscovite and kaolinite at pH 12 in 0.1 M NaCl + 0.02 M $CaCl_2$ it is assumed that only calcium-induced sorption species can be observed, as U(VI) was not sorbing under these conditions in the absence of calcium (chapter 4.4.2.1).

Irrespective of the chosen excitation wavelength, in none of the five samples (3 on muscovite and 2 on kaolinite) a characteristic luminescence line-narrowing similar to the one on Ca-bentonite (chapter 4.2.4.2) could be observed. All spectra feature comparatively broad emission bands, suggesting homo-resonance energy transfer from excited uranyl ions to

neighboring uranyl ions with slightly different bonding environments (Figure 46). As described in chapter 4.2.4.2, this phenomenon is observed for precipitates, where the uranium atoms are in close distance to each other. However, a broad maximum shifted to high wavelengths, as it is characteristic for uranates, can only be observed in the kaolinite sample at pH 12 in the presence of calcium. In all other samples no such feature can be found in the spectra at high excitation wavelength (Figure 46a,b,c,). Hence the broadening of the spectra cannot be attributed to the formation of U(VI) precipitates, except for the kaolinite sample at pH 12 in the presence of calcium. The same observation (inhomogeneous line broadening in the absence of precipitate-like spectral features) has been made by Tits *et al.* (2015) for U(VI) sorbed on TiO_2 under comparable conditions. The authors stated that they could not find a reason for the absence of luminescence line-narrowing. Combining the findings of the present study and of the one by Tits *et al.* (2015) (the only two existing studies applying site-selective TRLFS to U(VI)), line-narrowing was observed for Ca-bentonite (this study) and C-S-H but was absent on muscovite, kaolinite (both this study) and TiO_2. Hence, it has to be questioned whether the absence of line-narrowing is really a peculiar exception or rather the rule. Apparently, for the observation of line-narrowing certain preconditions have to be met, which are provided by Ca-bentonite (or rather montmorillonite) and C-S-H phases. These preconditions possibly derive from their mineral structure (and associated uranium immobilization processes) which is distinct from the one in muscovite, kaolinite and TiO_2.

Both montmorillonite and C-S-H have a sheet like structure, with two tetrahedral silicon-oxygen layers, sandwiching aluminum octahedra or calcium polyhedra, respectively. However, this is also the case for muscovite for which no line-narrowing could be observed. A major difference between these minerals is how the above described units are stacked and held together. Montmorillonite and C-S-H are swellable, being able to accommodate variable amounts of water next to counterions in the interlayers between the negatively charged sheets. In contrast to that, in muscovite the layers are bonded via potassium, resulting in a much smaller interlayer distance and absence of swelling properties. As a consequence, in montmorillonite and C-S-H radionuclides could possibly enter the interlayers and interact with the basal planes of the mineral, while the interlayer space is inaccessible in muscovite. A large part of its specific surface area is virtually blocked by the potassium. Also kaolinite does not possess expandable interlayer space. The weakly charged layers are connected via hydrogen bonds, inhibiting interactions of radionuclides with most of the basal planes. Consequently, the possibility to observe luminescence line-narrowing could be related to the ability of U(VI) to adsorb to the basal planes of the minerals and not only to the edge sites. Especially calcium-mediated species which are bound electrostatically could be associated to these sites. In case that the basal planes are not accessible for U(VI), the actual reactive surface area is much lower than the measured BET surface area. All uranium ions then accumulate at the edge sites, which could cause the distance between the uranium atoms to approach the critical Förster distance, at which homo-resonance energy transfer occurs.

Knowing the specific surface area of the minerals and the U(VI) loading of 1.67×10^{-3} mol/kg, it can be calculated that approx. 1.3, 10.1 and 4.5 uranium atoms are adsorbed on a 10 nm^2 surface area of Ca-bentonite, muscovite and kaolinite, respectively. Assuming homogeneous distribution and a model where a square area is attributed to each atom, the distance between the single adsorbed U(VI) atoms would be approx. 2.76 nm on Ca-bentonite, 0.99 nm on muscovite and 1.49 nm on kaolinite. Compared to Ca-bentonite, where a line-narrowing could be observed, the distance between the U atoms on muscovite and kaolinite is much closer to the critical Förster distance of 0.7 nm calculated by Tits *et al.* (2015). When additionally large parts of the surface of muscovite and kaolinite are not reactive, U(VI) is not distributed homogeneously, but accumulates on a smaller area. As a consequence, interatomic distances are further reduced, so that homo-resonance energy transfer can occur. Heterogeneous adsorption of U(VI) in very close distance to each other is also a good explanation for the line broadening on TiO_2 observed by Tits *et al.* (2015). With a U(VI) loading of 1×10^{-3} mol/kg and a specific surface area of 5 m^2/g the theoretical distance of the U atoms is 0.91 nm and therefore also close to the critical Förster distance.
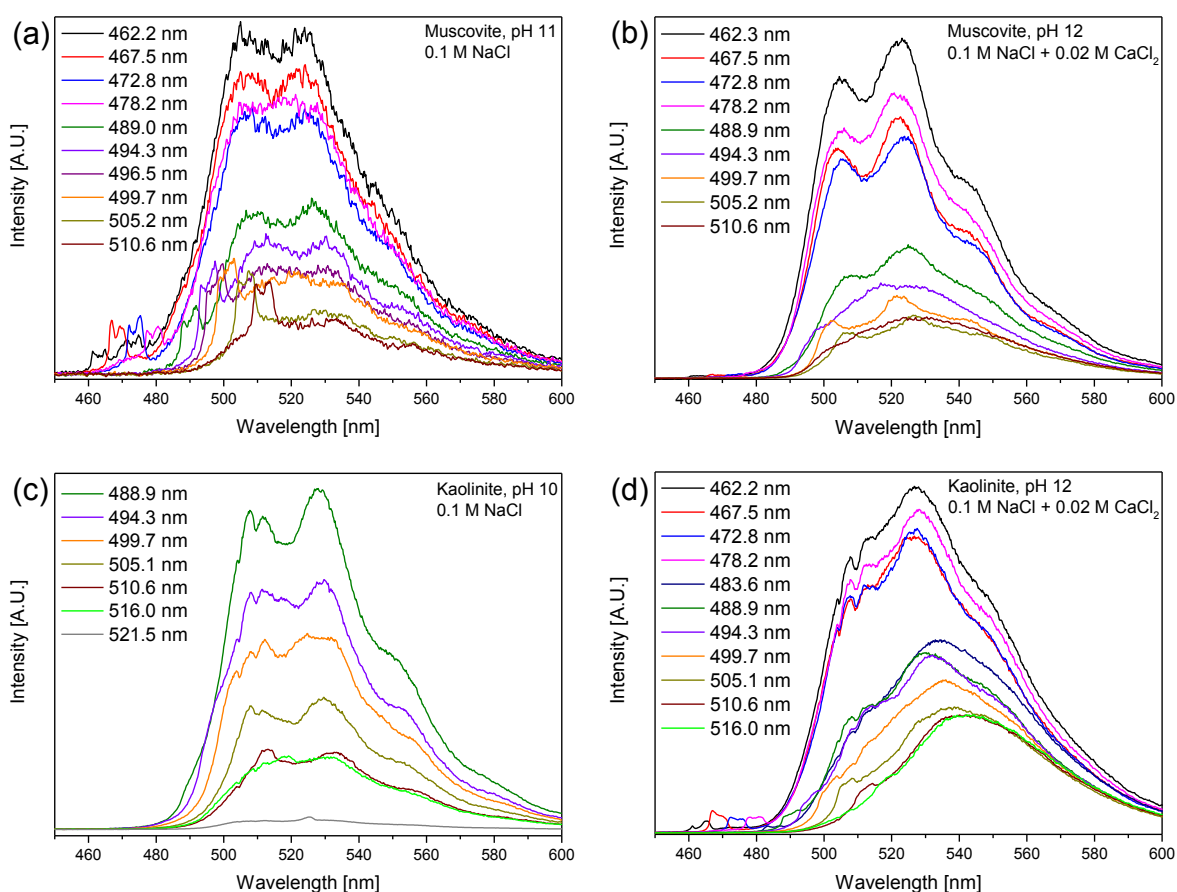

Figure 46: Emission spectra of U(VI) ([U(VI)] = 5×10^{-7} M) sorbed on muscovite at pH 11 in 0.1 M NaCl (a), muscovite at pH 12 in 0.1 M NaCl + 0.02 M CaCl$_2$ (b), kaolinite at pH 10 in 0.1 M NaCl (c) and kaolinite at pH 12 in 0.1 M NaCl + 0.02 M CaCl$_2$ (d) at different excitation wavelengths in the absence of CO$_2$.

The attribution of a reduced reactive surface area and resulting luminescence line-narrowing to the accessibility of interlayer space and availability of sorption sites on the basal plane is only a working hypothesis so far, which has to be confirmed by repeating comparable measurements on further solids.

Despite the absence of luminescence line-narrowing the static emission spectra still contain sufficient spectral information to identify different U(VI) species on both muscovite and kaolinite. Especially the comparison with the U(VI) sorption on Ca-bentonite (in diluted Gipshut solution, pH 11), where emission spectra at λ_{ex} = 499.7 nm revealed the presence of one inner-sphere and one outer-sphere sorption species (chapter 4.2.4.2), allows to draw some conclusions regarding the influence of pH and calcium concentration on the formation of these two different species. Figure 47 shows the normalized emission spectra at λ_{ex} = 499.7 nm of all samples, including U(VI) sorbed on Ca-bentonite and U(VI) precipitated on Ca-bentonite as references. Least information yields the spectrum of U(VI) sorbed on muscovite at pH 11 in the absence of calcium. Here one would expect the presence of one species, which does not involve calcium cations. However, no clear emission bands can be identified. Luminescence intensity is very weak, resulting in a low signal to noise ratio. The poor spectral quality can be explained by the fact that a much smaller amount of U(VI) is retained on the muscovite surface (approx. 50%) compared to the other samples. Direct comparison with the sample in the presence of calcium (otherwise identical experimental conditions) unequivocally reveals the impact of calcium on the static emission spectrum (dark blue spectrum in Figure 47). In the presence of calcium the spectrum is significantly intensified, mainly in the wavelength region around 521 nm. A transition band at this wavelength has been attributed to the first line of vibronic progression of TRLFS-species 1 (not to confuse with EXAFS-component 1) on Ca-bentonite. Additionally, in between the maxima attributed to TRLFS-species 1, slight shoulders appear which fit to the electronic and vibronic transition lines of TRLFS-species 2 on Ca-bentonite. This confirms the hypothesis that under these conditions both species are present – the 'regular' inner-sphere sorption complex and the calcium-mediated species. By contrast, the muscovite sample at pH 12 in the presence of calcium shows exclusively maxima which were attributed to TRLFS-species 1 on Ca-bentonite (light blue spectrum in Figure 47). The absence of shoulders between the emission bands of TRLFS-species 1 is in line with the hypothesis that under these conditions only the calcium-induced species is formed, as U(VI) sorption was at 0% in the absence of calcium. The overlap of the maxima with those from TRLFS-species 1 on Ca-bentonite proves that TRLFS-species 1 is a calcium-induced sorption complex. This was already hypothesized in chapter 4.2.4.2 but could not be proven, because no isolated samples in the absence and presence of calcium could be prepared with Ca-bentonite. The conclusion from the measurements on muscovite that TRLFS-species 1 is the calcium-induced species (and not TRLFS-species 2) is in accordance with the values obtained for the total symmetric stretch vibration of both sorption species (chapter 4.2.4.2). TRLFS-Species 1 has a greater spacing of

the transition bands, indicating weaker interaction with the mineral surface. Retention is realized via calcium which is situated between the mineral surface and the bound anionic uranyl hydroxide. The resulting larger distance of U(VI) from the substrate in the presence of calcium is also reflected in the EXAFS analysis of EXAFS-component 2 (chapter 4.2.4.3), corresponding to TRLFS-species 1, lacking backscattering paths from the substrate.
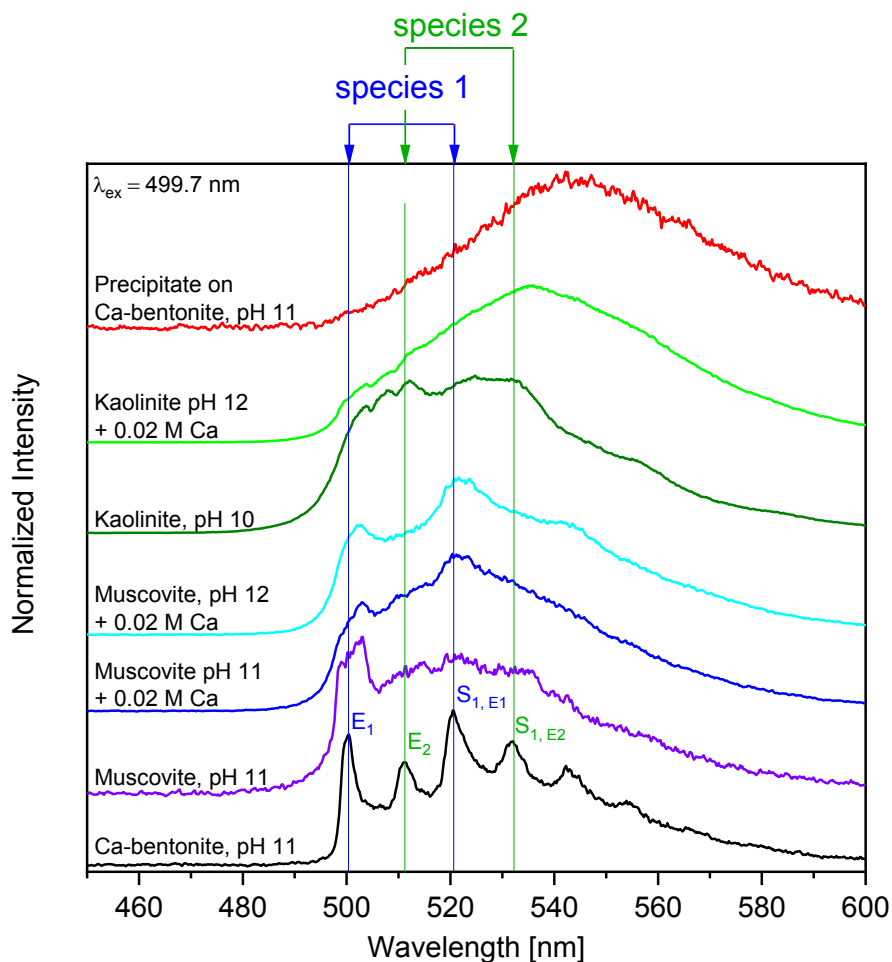
Figure 47: Comparison of single emission spectra at λ_{ex} = 499.7 nm of U(VI) ([U(VI)] = 5×10^{-7} M) sorbed on muscovite and kaolinite in the absence of CO_2 at different pH in 0.1 M NaCl or 0.1 M NaCl + 0.02 M $CaCl_2$. Spectra of U(VI) sorbed on Ca-bentonite and of a uranate-like precipitate on Ca-bentonite (both at pH 11) are included for comparison. Vertical lines in the graph attribute different emission lines to two independent species (presented in chapter 4.2.4.2).

The spectrum of U(VI) sorbed on kaolinite at pH 10 in the absence of calcium shows several small maxima of which the most prominent ones coincide with the electronic transition line and first line of vibronic progression of TRLFS-species 2 (dark green spectrum in Figure 47). In the light of the findings from the measurements on muscovite this makes sense, because TRLFS-species 2 is the one which is not calcium-induced. Conversely, at pH 12 in the presence of calcium, one would expect to observe the calcium-induced TRLFS-species 1 exclusively, as on muscovite. However, at these conditions the spectrum lacks spectral resolution. No single emission bands can be observed (light green spectrum in Figure 47). Additionally, the broad emission spectrum is shifted to higher wavelengths. Both characteristics, inhomogeneous broadening of the spectrum and the shift to higher

wavelengths, indicate U(VI) precipitation as Ca-uranate (see chapter 4.2.4.2). The spectrum resembles the one of U(VI) precipitated on Ca-bentonite. However, the shift to higher wavelengths is not as pronounced as in the reference sample. This can be explained by the fact, that the U(VI) precipitate is not the only U(VI) component in the sample, but that the obtained spectrum is a result of superimposition of single component spectra of both adsorbed and precipitated U(VI). The simultaneous presence of adsorbed U(VI) becomes evident when looking at emission spectra at different delay. As the Ca-uranate precipitate has a shorter luminescence lifetime than the adsorbed U(VI) species (Tits *et al.*, 2011; Tits *et al.*, 2015), with increasing delay time the portion of the spectrum at lower wavelength gains relative importance compared to the region characteristic for U(VI) precipitation (Figure Appendix 7). Even though adsorbed U(VI) is present in the sample, the dominance of U(VI) precipitation makes a spectral evaluation of the adsorbed U(VI) (and therefore also a comparison with the calcium-induced U(VI) species on muscovite) impossible.

The TRLFS results obtained in the presence of 0.02 M calcium at pH 12 show that under equal experimental conditions U(VI) predominantly precipitates on kaolinite, while it does not on muscovite. It can be assumed that U(VI) would also precipitate as Ca-uranate on muscovite and Ca-bentonite with time, if it was not removed from the solution by faster adsorption in the first place. Therefore, the precipitation of U(VI) on kaolinite can be related to its inability to adsorb U(VI) to the mineral surface, which can have different reasons. First of all a general lack of sorption sites could arise from disaggregation and dissolution of kaolinite with increasing pH. As described above, the accessible surface area for U(VI) on the intact kaolinite is already very small, leading to high adsorption density of U(VI). If the surface area is further reduced by mineral dissolution, not all of the U(VI) can be adsorbed anymore. Based on the elemental composition of the synthetic kaolinite given in Huittinen *et al.* (2010) as well as Al and Si concentrations measured in the supernatant after sorption, 2.9% of Al and 11.9% of Si were released from the mineral under these conditions. For muscovite mineral dissolution was weaker, with 2.8% of Al and 3.1% Si leached at pH 12, derived from leaching tests and digestion of the mineral. Hence, it is well possible, that the remaining kaolinite is not capable to accommodate all U(VI) from solution at its surface, forcing the excess U(VI) to precipitate. Alternatively, it is possible that the reduced ability for U(VI) to adsorb is not a result of a general degradation of the mineral but due to the absence of a very specific type of sorption sites in kaolinite, which is necessary for the formation of calcium-mediated sorption complexes. One hypothesis is that this kind of sorption complex requires strongly negatively charged basal planes as they are present in montmorillonite and muscovite, but not in kaolinite. Under chemical conditions where calcium-bridging is the only possible mechanism for U(VI) adsorption, U(VI) would precipitate in the samples with kaolinite in case that this mechanism is hindered due to the different kaolinite structure. The hypothesis that the U(VI) retention mechanism in kaolinite differs from the ones in Ca-bentonite and muscovite is supported by differences in luminescence lifetime.

For all samples U(VI) luminescence shows a biexponential decay (Figure 48 and Table 8). This indicates the presence of two independent U(VI) species on muscovite and kaolinite irrespective of pH and the presence or absence of calcium. As described in chapter 4.2.4.2 for U(VI) sorption on Ca-bentonite, the two adsorbed TRLFS-species 1 and 2 identified from the emission bands, cannot be distinguished based on their lifetimes. Both are represented by the longer lifetime τ_2. The short lifetime τ_1 is attributed to a Ca-uranate precipitate. All samples comprise both adsorbed and precipitated U(VI) but distinguish themselves dramatically by the proportion which these mechanisms add to the luminescence signal. The shape of the luminescence decay curve provides qualitative information about these relative contributions. Figure 48a shows that the three samples with U(VI) sorbed on muscovite exhibit very similar luminescence decay, suggesting that all contain similarly small amounts of precipitated U(VI). In contrast to that, for U(VI) sorbed on kaolinite the luminescence decay at pH 10 in the absence of calcium is fundamentally different to that at pH 12 in the presence of calcium (Figure 48b). At pH 10 in the absence of calcium, the adsorbed U(VI) has a much longer lifetime of $\tau_2 = 394 \pm 15 \, \mu s$, compared to 109-167 μs in the case of muscovite (Table 8). Therefore, a different process for U(VI) sorption has to be assumed. These strong differences in luminescence lifetime could be explained by sorption on different sites, i.e. on aluminol (Al-OH) or silanol (Si-OH) edge sites. Chisholm-Brause *et al.* (2004) and Kowal-Fouchard *et al.* (2004) observed considerably longer luminescence lifetimes for U(VI) inner-sphere complexes on silanol compared to aluminol functionalities at circumneutral pH. Chisholm-Brause *et al.* (2004) obtained lifetimes of 120 and 302 μs for inner-sphere sorption of uranyl hydroxides on gibbsite and silica, respectively. Kowal-Fouchard *et al.* (2004) measured lifetimes of 120 and even 400 μs for sorption of such complexes on corundum and silica. Direct comparison of the absolute values with the results of the present study is difficult, since the mentioned lifetimes in literature were not obtained at cryogenic conditions. Nevertheless, already the qualitative information about the strong difference in luminescence lifetime between U(VI) sorption on aluminol and silanol sites justifies the assumption, that U(VI) forms inner-sphere sorption complexes on silanol sites in the kaolinite sample at pH 10, while U(VI) predominantly adsorbs on aluminol sites in the montmorillonite and muscovite samples. However, it has to be noted that no sample at pH 10 exists for direct comparison in the montmorillonite or muscovite system due to lack of time. Alternatively the long-lived species on kaolinite could represent ternary uranyl silicate surface complexes, promoted by the stronger dissolution of kaolinite compared to the other minerals. Such complexes with silicate have been identified for Cm by Huittinen *et al.* (2012) and Schnurr *et al.* (2015). Additional experiments with all three minerals at various pH could offer more detailed insight but are not within the scope of this thesis. At pH 12 on kaolinite in the presence of calcium the course of the decay curve is shifted towards the one of U(VI) precipitated on Ca-bentonite, indicating greater contribution of U(VI) precipitates. This is in line with the unresolved and red-shifted luminescence spectrum in Figure 47.
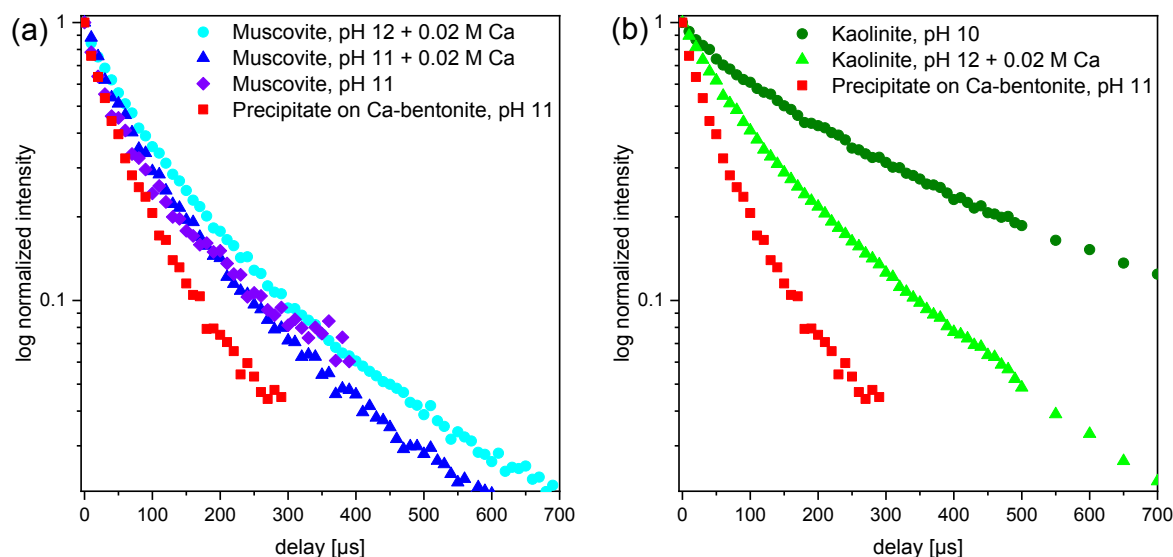
Figure 48: Logarithmized normalized luminescence intensity as function of delay time at λ_{ex} = 499.7 nm of U(VI) sorbed on muscovite (a) and kaolinite (b) at different pH and in 0.1 M NaCl or 0.1 M NaCl + 0.02 M CaCl$_2$. A uranate-like precipitate on Ca-bentonite at pH 11 is included for comparison. For experimental details of these samples please refer to Figure 46 and Figure 30.

Table 8: Luminescence lifetimes at λ_{ex} = 499.7 nm of U(VI) sorbed on muscovite and kaolinite at different pH in the presence and absence of calcium. A uranate-like precipitate on Ca-bentonite at pH 11 is included for comparison.

Sample	τ_1 [µs]	τ_2 [µs]
Muscovite, pH 11	21 ± 3	109 ± 9
Muscovite, pH 11 + 0.02 M CaCl$_2$	45 ± 2	157 ± 5
Muscovite, pH 12 + 0.02 M CaCl$_2$	52 ± 3	167 ± 6
Kaolinite, pH 10	99 ± 6	394 ± 15
Kaolinite, pH 12 + 0.02 M CaCl$_2$	60 ± 2	210 ± 3
Precipitate on Ca-bentonite, pH 11	58 ± 2	

Despite the absence of line-narrowing due to U(VI) adsorption in close proximity to each other and resulting homo-resonance energy transfer, calcium induced sorption species could be detected with site-selective TRLFS and conclusions regarding the nature of such complexes can be drawn. The species observed on muscovite at pH 12 in the presence of calcium corresponds to TRLFS-species 1, identified in Ca-bentonite (chapter 4.2.4.2), which is interpreted to be an outer-sphere sorption species, based on its frequency of the total symmetric stretch vibration. This leads to the conclusion, that the calcium-mediated attachment of U(VI) on clay minerals observed in the batch sorption experiments is realized by outer-sphere complexation based on electrostatic interactions and not by ternary or quaternary inner-sphere surface complexation. While there was no experimental indication for the formation of Ca-U(VI)-OH complexes, Ca(II) sorption experiments, zeta-potential measurements, site-selective TRLFS and EXAFS all support the hypothesis that calcium

adsorbs to the clay minerals in the first place, locally compensating negative surface charge and enabling electrostatic attachment of anionic uranyl hydroxides. Unfortunately, it was not possible to observe this kind of sorption species on kaolinite since the signal of adsorbed U(VI) was superimposed by the one of Ca-uranate, which precipitated due to an insufficient number of sorption sites on the mineral surface. The spectra obtained for muscovite, kaolinite and Ca-bentonite also prove that U(VI) predominantly sorbs on the respective clay minerals and not on C-(A)-S-H which might form as a secondary phase during the experiments (cf. chapter 4.1.3). If the mineral composition was altered severely and U(VI) sorption predominantly happened on C-(A)-S-H, the recorded spectra would all appear to be the same. However, spectral features which are characteristic for the different clay minerals are preserved within the different samples, such as presence or absence of line-narrowing and sorption on aluminol or silanol sites. Especially in the kaolinite sample at pH 12 in the presence of calcium, where mineral dissolution is noticeable, the formation of C-(A)-S-H should be favored. However, instead of adsorbing on C-(A)-S-H, the U(VI) rather appeared to precipitate.

4.4.3. Effect of Ca on Np(VI) sorption on muscovite

Batch sorption experiments with Np(VI) on muscovite were conducted in order to evaluate whether the findings for U(VI) sorption at (hyper)alkaline conditions and especially the strong effect of calcium can be transferred to other hexavalent actinides. Comparable behavior is expected for Np(VI), as the aqueous speciation at alkaline conditions is very similar to the one of U(VI), with a prevalence of anionic actinyl hydroxides. However, studies about the Np(VI) sorption on clay minerals or muscovite are not existent in literature. In order to be able to apply very low initial Np(VI) concentrations, inhibiting precipitation of neptunates, experiments were performed with the highly active isotope ^{239}Np, produced at the TRIGA research reactor of the JGU Mainz as described in chapter 3.1.

The results of the two experimental series in 0.1 M NaCl and in 0.1 M NaCl + 0.02 M CaCl$_2$ at pH 8-13 show a strong dependency of Np(VI) sorption on muscovite on both the pH and the availability of calcium (Figure 49). At pH 8-9 Np(VI) retention increases with increasing pH from ~20% to ~50%, irrespective of the presence of calcium. At higher pH, sorption reaches a maximum of 65% at pH 10.5 in the absence of calcium, before decreasing to almost 0% at pH 13.2. By contrast, in the presence of 0.02 M calcium Np(VI) sorption increases to 99%, forming a plateau of almost complete retention between pH 10.5 and 12, followed by a rapid drop to 9% at pH 12.5 and a sudden re-increase to 59% at pH 13.2. Consequently, the presence of calcium strongly enhances the Np(VI) sorption on muscovite at pH > 9.

Even though the effect of calcium on Np(VI) sorption on muscovite was the same as on U(VI) sorption, the pH-dependent sorption diagrams differ significantly, namely in the pH region 8-10. While sorption of U(VI) in this pH region was > 90% both in the presence and absence of

calcium, it is very low for Np(VI). This strongly decreased retention is surprising as Np(VI) was expected to behave exactly as U(VI), based on the similarities in aqueous speciation. U(VI) sorption on many materials, particularly clay minerals, is generally known to be highest at circumneutral pH so that the observed 15% of Np(VI) sorption at pH 7.9 are especially unexpected. A mechanism that could explain this low retention is reduction of Np(VI) to Np(V). Indeed, the measured E_h values for the sample series in 0.1 M NaCl + 0.02 M CaCl$_2$ at pH ≤ 9 lie within the stability field for Np(V) (red circles in Figure 50). The observed lowered, but increasing, Np-retention in this pH range fits to the sorption behavior of Np(V) reported in literature. In various studies it was found that the adsorption edge of Np(V) located between pH 6 and 10 (see chapter 2.4). However, the presence of Np(V) can only explain the low Np-retention at pH ≤ 9 in the samples containing calcium. The measured E_h values for the sorption series in the absence of calcium clearly plot within the stability field for Np(VI) (black squares in Figure 50). Here, apparently, the well-studied process of formation of strong inner-sphere sorption complexes of hexavalent actinides on amphoteric edge sites (see chapter 2.4) for some reason does not apply to the investigated system Np(VI)/muscovite. The observed increase in Np(VI) retention at pH > 8 seems to coincide with the formation of the anionic aqueous neptunyl hydroxide species $NpO_2(OH)_3^-$, which gains predominance over $NpO_2(OH)_2$ at pH > 8 (see Figure Appendix 1). This behavior is counterintuitive as usually cationic and neutral species are expected to sorb better to negatively charged surfaces than anionic species. In the present experiment, however, the known mechanisms for surface complexation at circumneutral conditions seem to not apply but anionic species are required to enable a sorption of Np(VI) to muscovite. As shown in chapter 4.4.2 for U(VI), the sorption of these anionic species is facilitated by calcium cations (which are also released from the muscovite in minor amounts, see chapter 4.4.2.1), which mediate between the actinide complex and the mineral surface. No literature data exist for the sorption of Np(VI) on muscovite or clay minerals for comparison. Hence, it has also never been demonstrated or postulated that Np(VI) strongly sorbs on muscovite at pH 8-10. This assumption, and the resulting peculiarity of the low retention in the present study, only arises from the fact that U(VI) has been shown to sorb strongly on muscovite under equal conditions. The reason for the different behavior of Np(VI) in the absence of calcium remains unclear for the time being.
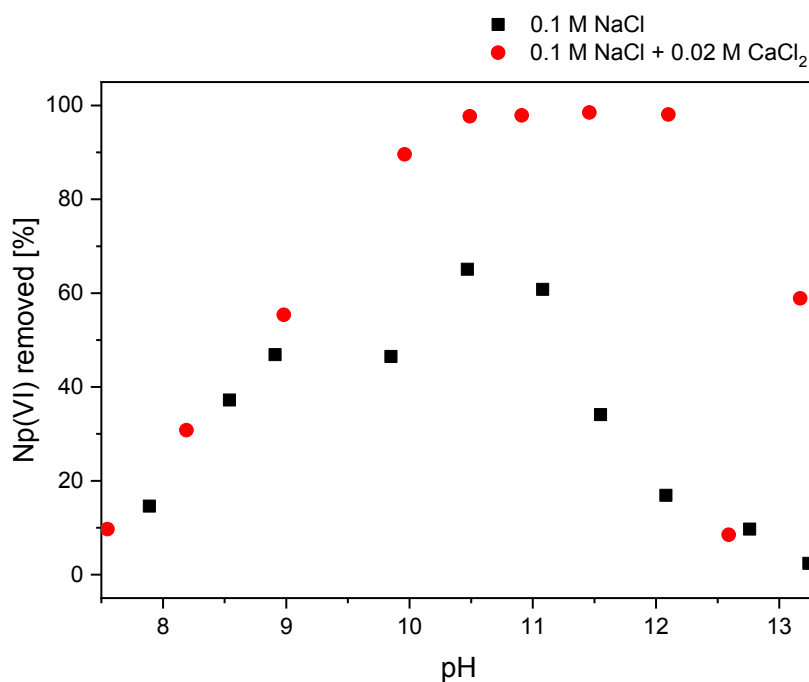
Figure 49: Percentage of Np(VI) ([Np(VI)] = 1×10^{-11} M) sorbed on muscovite (3 g/L) in 0.1 M NaCl and 0.1 M NaCl + 0.02 M CaCl$_2$ as a function of pH in the absence of CO$_2$.

At pH > 10 the Np(VI) sorption on muscovite is as expected, as the pH-dependent sorption diagram resembles the one obtained for U(VI) sorption (see Figure 44b). In the presence of calcium Np(VI) retention is very high up to pH 12 due to adsorbed calcium, locally compensating the negative surface charge of muscovite. In the experimental series without calcium addition this mediation cannot be achieved and Np(VI) sorption decreases at pH > 10.5. Tits *et al.* (2014) studied the Np(VI) sorption on TiO$_2$ at pH 10-14. In the absence of calcium they found high retention at pH 10 and, in accordance to the present study, a decrease of sorption with increasing pH. They were also able to observe a positive correlation between calcium concentration and distribution ratio R_d at pH 12, 13.3 and 14. As possible underlying mechanisms they identified the formation of ternary Ca-Np(VI)-hydroxide complexes or charge compensation at the mineral surface due to calcium adsorption. As already discussed in chapter 4.4.2, the latter theory is favored based on results from calcium sorption on Ca-bentonite, as well as from zeta potential, site-selective TRLFS and EXAFS measurements in the U(VI) system.
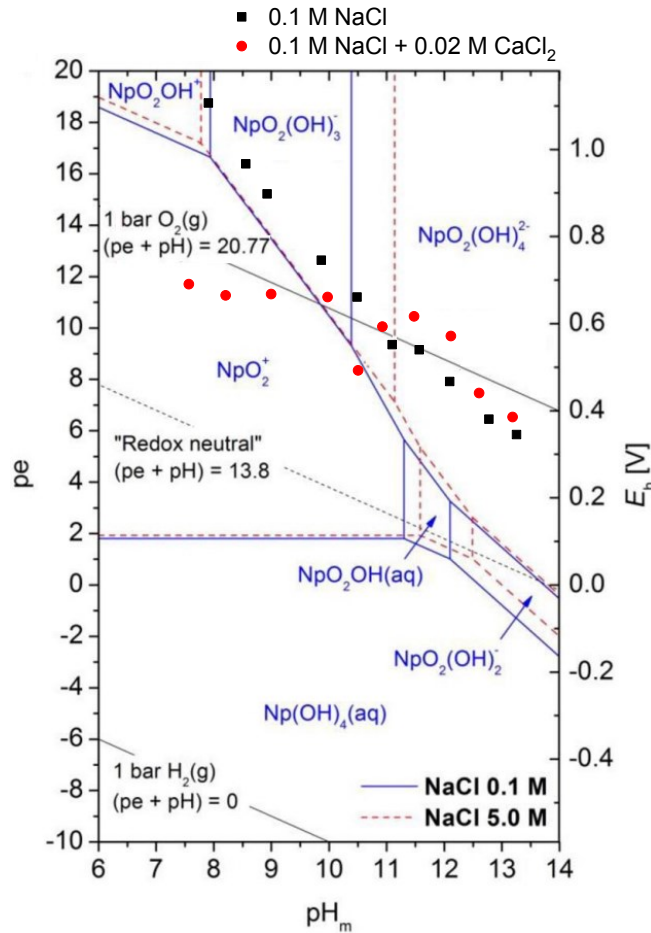
Figure 50: Predominance diagram of aqueous neptunium as a function of redox potential and pH modified after Gaona et al. (2013). Stability constants were recalculated to I=0. Measured E_h values of the sorption samples of the two experimental series (in 0.1 M NaCl and in 0.1 M NaCl + 0.02 M CaCl$_2$) are included in the diagram (black squares and red circles).

The observed unexpected re-increase of Np(VI) retention from pH 12.5 to pH 13.2 in the presence of calcium might be not due to adsorption on muscovite but could be caused by incorporation into or co-precipitation with newly formed mineral phases. In the presence of 0.02 M CaCl$_2$, the solution is supersaturated with respect to Ca(OH)$_2$ at pH > 12.5. Additionally, the formation of C-(A)-S-H phases could be triggered by the partial dissolution of muscovite at very high pH (both discussed in chapter 4.1.3 and 4.4.2). However, this hypothesis has to be assessed with spectroscopic measurements in the future. Alternatively, the data point at pH 12.5 could be regarded as an outlier, caused by potential mistakes during sample preparation. Owing to the low initial Np(VI) concentrations, it can be generally ruled out that precipitation of Np(VI) minerals contributes to the observed retention. Solubility studies showed that Np(VI) solubility is higher than 1×10^{-7} M in the presence of calcium at pH 9-12 (Fellhauer *et al.*, 2017).

5. Conclusions

Batch sorption experiments demonstrated that U(VI) retention on Ca-bentonite, Na-montmorillonite, kaolinite and muscovite in the pH range 8-13 can be very efficient, also in the presence of carbonate and despite the prevalence of anionic aqueous species. Above a certain pH, which is determined by the carbonate concentration, carbonate does not play a role in the U(VI) complexation in solution anymore due to the predominance of hydrolysis. A clear correlation between sorption behavior and aqueous U(VI) speciation was observed. Retention reaches a maximum at conditions where $UO_2(OH)_3^-$ is the predominant aqueous species. The arising question whether the strong retention is really achieved by adsorption of an anionic species or rather by (surface) precipitation of uranates could be answered by direct spectroscopic investigation of the U(VI) surface species. While *in situ* ATR FT-IR and CTR/RAXR showed the formation of U(VI) precipitates on the surface of Ca-bentonite and muscovite at super-micromolar U(VI) concentrations, in the more sensitive spectroscopic investigations TRLFS and EXAFS adsorption was found to be the dominant retention mechanism at sub-micromolar U(VI) concentrations, which were applied in the batch sorption experiments. The occurrence of luminescence line-narrowing and the frequency of the total symmetric stretch vibration obtained from the site-selective TRLFS emission spectra indicate the presence of two U(VI) surface complexes. EXAFS spectroscopy confirmed the presence of two independent U(VI) sorption species on Ca-bentonite at pH 8-13. One bidentate inner-sphere surface complex with an overall equatorial coordination of five adsorbed on aluminol or silanol edge sites and, with increasing fraction at very high pH, one sorption complex with a 4-fold equatorial coordination, resembling the aqueous species $UO_2(OH)_4^{2-}$ and presumed to be an outer-sphere complex.

It was hypothesized that the anionic uranyl hydroxide complexes are mediated to the negatively charged surface by calcium cations. Systematic evaluation of this hypothesis revealed that calcium sorbs strongly on Ca-bentonite at pH between pH 8 and 13, partially compensating negative surface charge of Ca-bentonite. U(VI) sorption on kaolinite and muscovite was strongly reduced in the absence of calcium at pH > 10. An increased retention upon addition of calcium proved the sorption enhancing effect of calcium at pH 10-12. Site-selective TRLFS allowed the spectroscopic observation and identification of calcium-induced U(VI) sorption complexes on muscovite, corresponding to the outer-sphere species found on Ca-bentonite. Combining the findings from batch sorption, zeta potential, TRLFS and EXAFS suggests that calcium adsorbs to the mineral surface in the first place, displaying locally positively charged sites which enable an electrostatically driven attachment of anionic uranyl hydroxides. The same effect of calcium could also be demonstrated for Np(VI) sorption on muscovite, which was associated to the similarity in aqueous speciation of Np(VI) and U(VI).

In conclusion, by combination of batch sorption experiments and different spectroscopic methods, it was unequivocally demonstrated that adsorption can cause strong retention of

hexavalent actinides by clay minerals at (hyper)alkaline conditions and low radionuclide concentrations. That means, that under certain alkaline repository conditions, where precipitation does not occur (due to very low concentrations or kinetic restraints), U(VI) and Np(VI) can still be effectively retained in argillaceous materials by adsorption despite the anionic character of prevailing aqueous species. Repulsive forces between the actinide species and the mineral surfaces are overcome by mediating Ca^{2+}, which is ubiquitous in geological repository environments. This finding is of great relevance, as also the migration of very small amounts of uranium or neptunium out of waste repositories could lead to a hazardous accumulation in the anthroposphere in the long term.

The present work provides insight into radionuclide retention at very complex chemical conditions as they could be encountered in a deep geological repository for radioactive waste. These complex conditions include high pH, high ionic strength, low radionuclide concentrations, the presence of carbonate, calcium and organic ligands as well as a multi-mineral solid phase. Such conditions, and in particular the chosen combination, have been studied very scarcely in the past, so that the thesis displays an important contribution to the understanding of radionuclide retention at environmental conditions, helping to take the next step towards realistic long-term safety assessment of nuclear waste repositories.

6. **Outlook**

The behavior of U(VI) in (hyper)alkaline solutions and its interaction with clay mineral surfaces as a function of pH, ionic strength, carbonate- and calcium concentration has been systematically investigated within the present study. Spectroscopic measurements clarified underlying mechanisms on the molecular level. Nonetheless, a number of additional experiments, which could not be conducted within the time frame of the doctoral thesis, might be helpful to complement the picture. It would be worthwhile to perform additional batch sorption experiments with montmorillonite which is entirely calcium-free. As the Na-montmorillonite in the present work still contained calcium impurities, muscovite and synthetic kaolinite were used as model minerals to achieve calcium-free conditions. A verification of the obtained results with calcium-free montmorillonite, including site-selective TRLFS measurements of calcium-induced sorption species, is still desirable. In general, site-selective TRLFS measurements of sorbed U(VI) should be expanded with further minerals in order to clarify which experimental conditions allow the observation of characteristic luminescence line-narrowing. Another open question is the existence of aqueous Ca-U(VI)-OH species. The presented results clearly show that U(VI) retention on clay minerals is strongly enhanced at pH 10-12 in the presence of calcium. However, so far all results suggest a mechanism where calcium first adsorbs at the mineral surface, generating positively charged sites, at which U(VI) adsorption is most probably realized electrostatically. None of our measurements was capable of providing a proof that complexation of calcium with uranyl hydroxides already occurs in solution. Nonetheless, the existence of such complexes is not unrealistic and the possibility of their formation should be investigated carefully in the future.

Batch sorption experiments with Np(VI) showed that calcium has the same retention-enhancing effect on Np(VI) as it has on U(VI). Complementation of these macroscopic results with spectroscopic measurements should be pursued to proof that the drawn analogy between Np(VI) and U(VI) also exists concerning the underlying retention mechanisms. Further experiments with other hexavalent actinides (such as Pu(VI)) could be performed in order to deduce an even more generalized picture of An(VI) sorption at (hyper)alkaline conditions.

In order to obtain more generalized knowledge about the potential of low molecular weight organic ligands to increase U(VI) mobility at (hyper)alkaline conditions, additional complexation and sorption experiments should be performed in the future with further organic ligands. Molecules with a stronger tendency to form complexes with U(VI) than ISA could compete against the strong hydrolysis of U(VI) at realistic repository conditions.

7. References

Akcay, H. (1998) Aqueous speciation and pH effect on the sorption behavior of uranium by montmorillonite. J. Radioanal. Nucl. Chem. 237, 133-137.

Allen, F.J., Truscott, C.L., Gutfreund, P., Welbourn, R.J.L. and Clarke, S.M. (2019) Potassium, Calcium, and Magnesium Bridging of AOT to Mica at Constant Ionic Strength. Langmuir 35, 5753-5761.

Altmaier, M., Metz, V., Neck, V., Müller, R. and Fanghänel, T. (2003) Solid-liquid equilibria of $Mg(OH)_{2(cr)}$ and $Mg_2(OH)_3Cl \cdot 4H_2O_{(cr)}$ in the system Mg-Na-H-OH-Cl-H_2O at 25°C. Geochim. Cosmochim. Acta 67, 3595-3601.

Altmaier, M., Yalçıntaş, E., Gaona, X., Neck, V., Müller, R., Schlieker, M. and Fanghänel, T. (2017) Solubility of U(VI) in chloride solutions. I. The stable oxides/hydroxides in NaCl systems, solubility products, hydrolysis constants and SIT coefficients. J. Chem. Thermodyn. 114, 2-13.

Amayri, S., Jermolajev, A. and Reich, T. (2011) Neptunium(V) sorption on kaolinite. Radiochim. Acta 99, 349-357.

ANDRA (2013) The Cigeo project - Meuse/Haute-Marne reversible geological disposal facility for radioactive waste. ANDRA, French National Radioactive Waste Management Agency, Châtenay-Malabry, France.

Ankudinov, A.L., Ravel, B., Rehr, J.J. and Conradson, S.D. (1998) Real-space multiple-scattering calculation and interpretation of X-ray-absorption near-edge structure. Phys. Rev. B 58, 7565-7576.

Appelo, C. and Postma, D. (1994) Geochemistry, groundwater and pollution. A.A. Balkema, Rotterdam, Netherlands.

Arnarson, T.S. and Keil, R.G. (2000) Mechanisms of pore water organic matter adsorption to montmorillonite. Mar. Chem. 71, 309-320.

Atesok, G., Somasundaran, P. and Morgan, L.J. (1988) Adsorption properties of Ca^{2+} on Na-kaolinite and its effect on flocculation using polyacrylamides. Colloids Surf 32, 127-138.

Bachmaf, S., Planer-Friedrich, B. and Merkel, B.J. (2008) Effect of sulfate, carbonate, and phosphate on the uranium(VI) sorption behavior onto bentonite. Radiochim. Acta 96, 359-366.

Baran, V. and Tympl, M. (1966) Infrared Spectra of Sodium Uranates. Zeitschrift für anorganische und allgemeine Chemie 347, 175-183.

Baston, G.M.N., Berry, J.A., Bond, K.A., Boult, K.A., Brownsword, M. and Linklater, C.M. (1994) Effects of cellulosic degradation products on uranium sorption in the geosphere. J. Alloys Compd. 213-214, 475-480.

Bell, J.T. and Biggers, R.E. (1968) Absorption spectrum of the Uranyl Ion in Perchlorate Media. J. Mol. Spectrosc 25, 312-329.

Berner, U.R. (1992) Evolution of pore water chemistry during degradation of cement in a radioactive waste repository environment. Waste Manag 12, 201-219.

Bernhard, G., Geipel, G., Reich, T., Brendler, V., Amayri, S. and Nitsche, H. (2001) Uranyl(VI) carbonate complex formation: Validation of the $Ca_2UO_2(CO_3)_{3(aq.)}$ species. Radiochim. Acta 89, 511-518.

BGR (2007) Endlagerung radioaktiver Abfälle in Deutschland - Untersuchung und Bewertung von Regionen mit potenziell geeigneten Wirtsgesteinsformationen. Bundesanstalt für Geowissenschaften und Rohstoffe (BGR), Hannover/Berlin, Germany.

Bleise, A., Danesi, P.R. and Burkart, W. (2003) Properties, use and health effects of depleted uranium (DU): a general overview. J. Environ. Radioact. 64, 93-112.

BMU (2015) Programme for the responsible and safe management of spent fuel and radioactive waste. Federal Ministry for the Environment, Nature Conservation, Building and Nuclear Safety, Berlin, Germany.

Bots, P., Morris, K., Hibberd, R., Law, G.T., Mosselmans, J.F., Brown, A.P., Doutch, J., Smith, A.J. and Shaw, S. (2014) Formation of stable uranium(VI) colloidal nanoparticles in conditions relevant to radioactive waste disposal. Langmuir 30, 14396-14405.

Boult, K.A., Cowper, M.M., Heath, T.G., Sato, H., Shibutani, T. and Yui, M. (1998) Towards an understanding of the sorption of U(VI) and Se(IV) on sodium bentonite. J. Contam. Hydrol. 35, 141-150.

Bradbury, M.H. and Baeyens, B. (1997) A mechanistic description of Ni and Zn sorption on Na-montmorillonite Part II: modelling. J. Contam. Hydrol. 27, 223-248.

Bradbury, M.H. and Baeyens, B. (2005) Modelling the sorption of Mn(II), Co(II), Ni(II), Zn(II), Cd(II), Eu(III), Am(III), Sn(IV), Th(IV), Np(V) and U(VI) on montmorillonite: Linear free energy relationships and estimates of surface binding constants for some selected heavy metals and actinides. Geochim. Cosmochim. Acta 69, 875-892.

Bradbury, M.H. and Baeyens, B. (2009) Sorption modelling on illite Part I: Titration measurements and the sorption of Ni, Co, Eu and Sn. Geochim. Cosmochim. Acta 73, 990-1003.

Bradl, H. (2005) Heavy Metals in the Environment: Origin, Interaction and Remediation, 1st Edition ed. Elsevier Academic Press, London, UK.

Brayden, T.H., Poropatic, P.A. and Watanabe, J.L. (1988) Iterative target testing for calculation of missing data points. Anal. Chem. 60, 1154-1158.

Brewitz, W. (1982) Eignungsprüfung der Schachtanlage Konrad für die Endlagerung radioaktiver Abfälle. Institut für Tiefenlagerung, Neuherberg, Germany.

Brinkmann, H., Patzschke, M., Kaden, P., Raiwa, M., Rossberg, A., Kloditz, R., Heim, K., Moll, H. and Stumpf, T. (2019) Complex formation between $UO_2^{(2+)}$ and alpha-isosaccharinic acid: insights on a molecular level. Dalton Trans.

Catalano, J.G. and Brown, G.E. (2005) Uranyl adsorption onto montmorillonite: Evaluation of binding sites and carbonate complexation. Geochim. Cosmochim. Acta 69, 2995-3005.

Chen, X., Peng, S. and Wang, J. (2014) Retention profile and kinetics characteristics of the radionuclide 90-Sr(II) onto kaolinite. J. Radioanal. Nucl. Chem. 303, 509-519.

Cherian, C., Kollannur, N.J., Bandipally, S. and Arnepalli, D.N. (2018) Calcium adsorption on clays: Effects of mineralogy, pore fluid chemistry and temperature. Appl. Clay Sci. 160, 282-289.

Chernorukov, N.G., Nipruk, O.V. and Kostrova, E.L. (2016) Synthesis and study of sodium uranate $Na_2U_2O_7 \cdot 6H_2O$ and of products of its dehydration and thermal decomposition. Radiochemistry 58, 124-127.

Chisholm-Brause, C., Conradson, S.D., Buscher, C.T., Eller, P.G. and Morris, D.E. (1994) Speciation of uranyl sorbed at multiple binding sites on montmorillonite. Geochim. Cosmochim. Acta 58, 3625-3631.

Chisholm-Brause, C.J., Berg, J.M., Little, K.M., Matzner, R.A. and Morris, D.E. (2004) Uranyl sorption by smectites: spectroscopic assessment of thermodynamic modeling. J Colloid Interface Sci 277, 366-382.

Chisholm-Brause, C.J., Berg, J.M., Matzner, R.A. and Morris, D.E. (2001) Uranium(VI) Sorption Complexes on Montmorillonite as a Function of Solution Chemistry. J Colloid Interface Sci 233, 38-49.

Choppin, G., Liljenzin, J.-O. and Rydberg, J.A.N. (1995) Radiochemistry and Nuclear Chemistry (Second Edition). Butterworth-Heinemann, Oxford, U.K.

Comarmond, M.J., Steudtner, R., Stockmann, M., Heim, K., Muller, K., Brendler, V., Payne, T.E. and Foerstendorf, H. (2016) The Sorption Processes of U(VI) onto $SiO2$ in the Presence of Phosphate: from Binary Surface Species to Precipitation. Environ Sci Technol 50, 11610-11618.

Cotton, S. (2006) Lanthanide and Actinide Chemistry. John Wiley & Sons Ltd, Chichester, England.

Dekov, V.M., Kamenov, G.D., Stummeyer, J., Thiry, M., Savelli, C., Shanks, W.C., Fortin, D., Kuzmann, E. and Vértes, A. (2007) Hydrothermal nontronite formation at Eolo Seamount (Aeolian volcanic arc, Tyrrhenian Sea). Chem. Geol. 245, 103-119.

Denning, R.G. (2007) Electronic Structure and Bonding in Actinyl Ions and their Analogs. J. Phys. Chem. A 111, 4125-4143.

Di Pietro, P. and Kerridge, A. (2016) U-Oyl Stretching Vibrations as a Quantitative Measure of the Equatorial Bond Covalency in Uranyl Complexes: A Quantum-Chemical Investigation. Inorg Chem 55, 573-583.

Drobot, B. (2016) Entwicklung und Validierung mathematischer Methoden zur Auswertung spektroskopischer Daten der Uranyl(VI)-Hydrolyse, Institut für Ressourcenökologie, Helmholtz-Zentrum Dresden-Rossendorf. TU Dresden, Dresden, Germany.

Drobot, B., Bauer, A., Steudtner, R., Tsushima, S., Bok, F., Patzschke, M., Raff, J. and Brendler, V. (2016) Speciation Studies of Metals in Trace Concentrations: The Mononuclear Uranyl(VI) Hydroxo Complexes. Anal Chem 88, 3548-3555.

Duff, M.C., Coughlin, J.U. and Hunter, D.B. (2002) Uranium co-precipitation with iron oxide minerals. Geochim. Cosmochim. Acta 66, 3533-3547.

Dullies, P. (2019) Untersuchungen zum Einfluss von Isosaccharinsäure auf die U(VI)-Rückhaltung an Ca-Bentonit unter alkalischen Bedingungen. Hochschule für Technik und Wirtschaft (HTW) Dresden, Dresden, Germany.

Elo, O., Müller, K., Ikeda-Ohno, A., Bok, F., Scheinost, A.C., Hölttä, P. and Huittinen, N. (2017) Batch sorption and spectroscopic speciation studies of neptunium uptake by montmorillonite and corundum. Geochim. Cosmochim. Acta 198, 168-181.

Fanghänel, T. and Neck, V. (2002) Aquatic chemistry and solubility phenomena of actinide oxides/hydroxides. Pure Appl. Chem. 74, 1895-1907.

Farooq, U., Tweheyo, M.T., Sjöblom, J. and Øye, G. (2011) Surface Characterization of Model, Outcrop, and Reservoir Samples in Low Salinity Aqueous Solutions. J Disper Sci Technol 32, 519-531.

Fay, M.J., Proctor, A., Hoffmann, D.P. and Hercules, D.M. (1988) Unraveling EXAFS spectroscopy. Anal. Chem. 60, 1225A-1243A.

Fellhauer, D., Gaona, X., Rothe, J., Altmaier, M. and Fanghänel, T. (2017) Neptunium(VI) solubility in alkaline $CaCl_2$ solutions: evidence for the formation of calcium neptunates Ca x NpO_3+x (s,hyd). Monatshefte für Chemie - Chemical Monthly 149, 237-252.

Fenter, P., Park, C., Nagy, K.L. and Sturchio, N.C. (2007) Resonant anomalous X-ray reflectivity as a probe of ion adsorption at solid–liquid interfaces. Thin Solid Films 515, 5654-5659.

Fenter, P.A. (2002) X-ray Reflectivity as a Probe of Mineral-Fluid Interfaces: A User Guide. Rev. Mineral. Geochem. 49, 149-221.

Fernández, R., Mäder, U., Rodríguez, M., Virgil de la Villa, R. and Cuevas, J. (2009) Alteration of compacted bentonite by diffusion of highly alkaline solutions. Eur J Mineral 21, 725-735.

Fialips, C.-I., Petit, S., Decarreau, A. and Beaufort, D. (2000) Influence of synthesis pH on Kaolinite "crystallinity" and surface properties. Clay Clay Miner. 48, 173-184.

Foerstendorf, H., Heim, K. and Rossberg, A. (2012) The complexation of uranium(VI) and atmospherically derived CO2 at the ferrihydrite-water interface probed by time-resolved vibrational spectroscopy. J Colloid Interface Sci 377, 299-306.

Fritsch, K. (2018) Investigation of uranium(VI) retention by montmorillonite at high ionic strengths. Technische Universität Dresden, Dresden, Germany.

Gaona, X., Fellhauer, D. and Altmaier, M. (2013) Thermodynamic description of Np(VI) solubility, hydrolysis, and redox behavior in dilute to concentrated alkaline NaCl solutions. Pure Appl. Chem. 85, 2027-2049.

Gaona, X., Tits, J., Dardenne, K., Liu, X., Rothe, J., Denecke, M.A., Wieland, E. and Altmaier, M. (2012) Spectroscopic investigations of Np(V/VI) redox speciation in hyperalkaline TMA-(OH, Cl) solutions. Radiochim. Acta 100, 759-770.

Gascó, G. and Méndez, A. (2005) Sorption of Ca^{2+}, Mg^{2+}, Na^+ and K^+ by clay minerals. Desalination 182, 333-338.

Gaucher, É.C., Blanc, P., Bardot, F., Braibant, G., Buschaert, S., Crouzet, C., Gautier, A., Girard, J.-P., Jacquot, E., Lassin, A., Negrel, G., Tournassat, C., Vinsot, A. and Altmann, S. (2006) Modelling the porewater chemistry of the Callovian–Oxfordian formation at a regional scale. Comptes Rendus Geoscience 338, 917-930.

George, G.N. and Pickering, I.J. (1995) EXAFSPAK: A Suite of Computer Programs for Analysis of X-ray Absorption Spectra, Stanford Synchrotron Radiation Laboratory, Stanford, CA. USA.

Grambow, B., Fattahi, M., Montavon, G., Moisan, C. and Giffaut, E. (2006) Sorption of Cs, Ni, Pb, Eu(III), Am(III), Cm, Ac(III), Tc(IV), Th, Zr, and U(IV) on MX 80 bentonite: An experimental approach to assess model uncertainty. Radiochim. Acta 94.

Griffin, L.R., Browning, K.L., Lee, S.Y., Skoda, M.W., Rogers, S. and Clarke, S.M. (2016) Multilayering of Calcium Aerosol-OT at the Mica/Water Interface Studied with Neutron Reflection: Formation of a Condensed Lamellar Phase at the CMC. Langmuir 32, 13054-13064.

Gückel, K., Rossberg, A., Brendler, V. and Foerstendorf, H. (2012) Binary and ternary surface complexes of U(VI) on the gibbsite/water interface studied by vibrational and EXAFS spectroscopy. Chem. Geol. 326-327, 27-35.

Guillaumont, R., Fanghänel, T., Fuger, J., Grenthe, I., Neck, V., Palmer, D.A. and Rand, M.H. (2003) Update on the Chemical Thermodynamics of Uranium, Neptunium, Plutonium, Americium and Technetium. Elsevier, Amsterdam, The Netherlands.

Hama, K., Kunimaru, T., Metcalfe, R. and Martin, A.J. (2007) The hydrogeochemistry of argillaceous rock formations at the Horonobe URL site, Japan. Phys Chem Earth 32, 170-180.

Harfouche, M., Wieland, E., Dähn, R., Fujita, T., Tits, J., Kunz, D. and Tsukamoto, M. (2006) EXAFS study of U(VI) uptake by calcium silicate hydrates. J Colloid Interface Sci 303, 195-204.

Hartmann, E., Geckeis, H., Rabung, T., Lützenkirchen, J. and Fanghänel, T. (2008) Sorption of radionuclides onto natural clay rocks. Radiochim. Acta 96.

He, Y., Chen, Y.-G. and Ye, W.-M. (2016) Equilibrium, kinetic, and thermodynamic studies of adsorption of Sr(II) from aqueous solution onto GMZ bentonite. Environ. Earth Sci. 75.

Heim, D. (1990) Tone und Tonminerale: Grundlagen der Sedimentologie und Mineralogie. Ferdinand Enke Verlag, Stuttgart, Germany.

Hellebrandt, S. (2017) Grenzflächenreaktionen von Actiniden an Muskovit. Technische Universität Dresden, Dresden, Germany.

Hellebrandt, S., Lee, S.S., Knope, K.E., Lussier, A.J., Stubbs, J.E., Eng, P.J., Soderholm, L., Fenter, P. and Schmidt, M. (2016) A Comparison of Adsorption, Reduction, and Polymerization of the Plutonyl(VI) and Uranyl(VI) Ions from Solution onto the Muscovite Basal Plane. Langmuir 32, 10473–10482.

Hennig, C. (2007) Evidence for double-electron excitations in the L-3-edge X-ray absorption spectra of actinides. Phys. Rev. B 75, 1-7.

Hennig, C., Reich, T., Dähn, R. and Scheidegger, A.M. (2002) Structure of uranium sorption complexes at montmorillonite edge sites. Radiochim. Acta 90, 653-657.

Henry, W. (1803) Experiments on the Quantity of Gases Adsorbed by Water, at Different Temperatures and under Different Pressures. Phil. Trans. R. Soc. Lond. 93.

Hiltmann, W. and Stribrny, B. (1998) Tonmineralogie und Bodenphysik. Springer Verlag, Heidelberg, Germany.

Ho, C. and Handy, R.L. (1963) Electrokinetic properties of lime-treated bentonites. Clay Clay Miner. 12, 267-280.

Hubbard, A.T. (2002) Encyclopedia of surface and colloid science, Encyclopedia of surface and colloid science. Dekker, New York (USA); Basel (Switzerland).

Huittinen, N., Rabung, T., Andrieux, P., Lehto, J. and Geckeis, H. (2010) A comparative batch sorption and time-resolved laser fluorescence spectroscopy study on the sorption of Eu(III) and Cm(III) on synthetic and natural kaolinite. Radiochim. Acta 98, 613-620.

Huittinen, N., Rabung, T., Schnurr, A., Hakanen, M., Lehto, J. and Geckeis, H. (2012) New insight into Cm(III) interaction with kaolinite – Influence of mineral dissolution. Geochim. Cosmochim. Acta 99, 100-109.

Ingram, K.I., Haller, L.J. and Kaltsoyannis, N. (2006) Density functional theory investigation of the geometric and electronic structures of $[UO_2(H_2O)m(OH)n](2 - n)$ (n + m = 5). Dalton Trans, 2403-2414.

Ivanov, P., Griffiths, T., Bryan, N.D., Bozhikov, G. and Dmitriev, S. (2012) The effect of humic acid on uranyl sorption onto bentonite at trace uranium levels. J Environ Monit 14, 2968-2975.

Jahn, S. and Sönnke, J. (2013) Endlagerstandortmodell Nord (AnSichT) - Teil II Zusammenstellung von Gesteinseigenschaften für den Langzeitsicherheitsnachweis - Zwischenbericht. BGR, Hannover, Germany.

Jasmund, K. and Lagaly, G. (1993) Tonminerale und Tone. Steinkopff Verlag Darmstadt, Darmstadt, Germany.

Jobmann, M., Bebiolka, A., Jahn, S., Lommerzheim, A., Maßmann, J., Meleshyn, A., Mrugalla, S., Reinhold, K., Rübel, A., Stark, L. and Ziefle, G. (2017) Projekt ANSICHT - Sicherheits- und Nachweismethodik für ein Endlager im Tongestein in Deutschland - Syntheseberich. DBE TECHNOLOGY & GRS, Peine, Germany.

Joseph, C. (2013) The ternary system U(VI) / humic acid / Opalinus Clay, Helmholtz-Zentrum Dresden-Rossendorf, Institut für Ressourcenökologie. Technische Universität Dresden, Dresden, Germany.

Joseph, C., Stockmann, M., Schmeide, K., Sachs, S., Brendler, V. and Bernhard, G. (2013) Sorption of U(VI) onto Opalinus Clay: Effects of pH and humic acid. Appl Geochem 36, 104-117.

Kaiser, H.F. (1958) The varimax criterion for analytic rotation in factor analysis. Psychometrika 23, 187–200.

Kaplan, D.I., Gervais, T.L. and Krupka, K.M. (1998) Uranium(VI) Sorption to Sediments Under High pH and Ionic Strength Conditions. Radiochim. Acta 80, 201-211.

Kasar, S., Kumar, S., Kar, A., Bajpai, R.K, Kaushik, C.P. and Tomar, B.S. (2014) Retention behaviour of Cs(I), Sr(II), Tc(VII) and Np(V) on smectite-rich clay. J. Radioanal. Nucl. Chem. 300, 71-75.

Kaszuba, J.P. and Runde, W.H. (1999) The Aqueous Geochemistry of Neptunium: Dynamic Control of Soluble Concentrations with Applications to Nuclear Waste Disposal. Environ. Sci. Technol 33, 4427-4433.

Kenney, J.P.L., Kirby, M.E., Cuadros, J. and Weiss, D.J. (2017) A conceptual model to predict uranium removal from aqueous solutions in water–rock systems associated with low- and intermediate-level radioactive waste disposal. RSC Adv. 7, 7876-7884.

Kessler, G. (2012) Minor Actinides: Partitioning, Transmutation and Incineration, Sustainable and Safe Nuclear Fission Energy, pp. 243-282.

Kitamura, A., Yamamura, T., Haseb, H., Yamamoto, T. and Moriyama, H. (1998) Measurement of Hydrolysis Species of U(VI) by Time-Resolved Laser Induced Fluorescence Spectroscopy. Radiochim. Acta 82, 147-152.

Koningsberger, D.C., Mojet, B.L., van Dorssen, G.E. and Ramaker, D.E. (2000) XAFS Spectroscopy: Fundamental Principles and Data Analysis. Top. Catal. 10, 143-155.

Kowal-Fouchard, A., Drot, R., Simoni, E. and Ehrhardt, J. (2004) Use of Spectroscopic Techniques for Uranium(VI)/Montmorillonite Interaction Modeling. Environ. Sci. Technol 38, 1399-1407.

Kratz, J.V. and Lieser, K.H. (2013) Nuclear and Radiochemistry: Fundamentals and Applications, 2 Volume Set. Wiley-VCH, Hoboken, USA.

Lakowicz, J.R. (2006) Principles of fluorescence spectroscopy. Springer, New York, USA.

Langmuir, I. (1918) The adsorption of gases on plane surfaces of glass, mica and platinum. J. Am. Chem. Soc. 40.

Lee, J.-Y., Vespa, M., Gaona, X., Dardenne, K., Rothe, J., Rabung, T., Altmaier, M. and Yun, J.-I. (2017) Formation, stability and structural characterization of ternary $MgUO_2(CO_3)_3^{2-}$ and $Mg_2UO_2(CO_3)_{3(aq)}$ complexes. Radiochim. Acta 105, 171–185.

Lee, J.Y. and Yun, J.I. (2013) Formation of ternary $CaUO_2(CO_3)_3^{(2-)}$ and $Ca_2UO_2(CO_3)_{3(aq)}$ complexes under neutral to weakly alkaline conditions. Dalton Trans 42, 9862-9869.

Lee, S.S., Fenter, P., Nagy, K.L. and Sturchio, N.C. (2012) Monovalent ion adsorption at the muscovite (001)-solution interface: relationships among ion coverage and speciation, interfacial water structure, and substrate relaxation. Langmuir 28, 8637-8650.

Lefevre, G. (2004) In situ Fourier-transform infrared spectroscopy studies of inorganic ions adsorption on metal oxides and hydroxides. Adv Colloid Interface Sci 107, 109-123.

Lefevre, G., Kneppers, J. and Fedoroff, M. (2008) Sorption of uranyl ions on titanium oxide studied by ATR-IR spectroscopy. J Colloid Interface Sci 327, 15-20.

Lefevre, G., Noinville, S. and Fedoroff, M. (2006) Study of uranyl sorption onto hematite by in situ attenuated total reflection-infrared spectroscopy. J Colloid Interface Sci 296, 608-613.

Lewis, G.N. and Kasha, M. (1944) Phosphorescence and the Triplet State. J. Am. Chem. Soc. 66, 2100-2116.

Li, G.G., Bridges, F. and Booth, C.H. (1995) X-ray-absorption fine-structure standards: A comparison of experiment and theory. Phys Rev B Condens Matter 52, 6332-6348.

Lieser, K. (1991) Einführung in die Kernchemie. VCH Verlagsgesellschaft, Weinheim, Germany.

Lommerzheim, M. and Jobmann, A. (2014) Endlagerkonzept sowie Verfüll- und Verschlusskonzept für das Standortmodell NORD, TEC-08-2014-Z. DBE Technology, Peine, Germany.

Macé, N., Wieland, E., Dähn, R., Tits, J. and Scheinost, A.C. (2013) EXAFS investigation on U(VI) immobilization in hardened cement paste: influence of experimental conditions on speciation. Radiochim. Acta 101, 379-389.

Maher, K., Bargar, J.R. and Brown, G.E., Jr. (2013) Environmental speciation of actinides. Inorg Chem 52, 3510-3532.

Malinowski, E.R. (2002) Determination of the number of factors and the experimental error in a data matrix. Anal. Chem. 49, 612-617.

Manceau, A., Marcus, M.A. and Tamura, N. (2002) Quantitative Speciation of Heavy Metals in Soils and Sediments by Synchrotron X-ray Techniques, in: Fenter, P., Sturchio, N.C. (Eds.), Rev. Mineral. Geochem. Mineralogical Society of America, Washington, D.C., U.S.

Marques Fernandes, M., Baeyens, B., Dähn, R., Scheinost, A.C. and Bradbury, M.H. (2012) U(VI) sorption on montmorillonite in the absence and presence of carbonate: A macroscopic and microscopic study. Geochim. Cosmochim. Acta 93, 262-277.

Martínez-Torrents, A., Meca, S., Baumann, N., Martí, V., Giménez, J., de Pablo, J. and Casas, I. (2013) Uranium speciation studies at alkaline pH and in the presence of hydrogen peroxide using time-resolved laser-induced fluorescence spectroscopy. Polyhedron 55, 92-101.

Matz, W., Schell, N., Bernhard, G., Prokert, F., Reich, T., Claussner, J., Oehme, W., Schlenk, R., Dienel, S., Funke, H., Eichhorn, F., Betzl, M., Prohl, D., Strauch, U., Hüttig, G., Krug, H., Neumann, W., Brendler, V., Reichel, P., Denecke, M.A. and Nitsche, H. (1999) ROBL - a CRG beamline for radiochemistry and materials research at the ESRF. J. Synchrotron Radiat 6, 1076-1085.

Mayordomo, N. (2017) Experimental and theoretical studies of mixed smectite and Al_2O_3 nanoparticles to improve pollutant retention in geochemical barriers, Departamento de Química Analítica, Química Física e Ingeniería Química. Universidad de Alcalá, Madrid, Spain.

Mazurek, M. (2004) Long-term Used Nuclear Fuel Waste Management – Geoscientific Review of the Sedimentary Sequence in Southern Ontario. Institute of Geological Sciences, University of Bern Bern, Switzerland.

McGlynn, S.P., Smith, J.K. and Neely, W.C. (1961) Electronic Structure, Spectra, and Magnetic Properties of Oxycations. III. Ligation Effects on the Infrared Spectrum of the Uranyl Ion J. Chem. Phys. 35, 105-116.

Meleshyn, A., Azeroual, M., Reeck, T., Houben, G., Riebe, B. and Bunnenberg, C. (2009) Influence of (Calcium-)Uranyl-Carbonate Complexation on U(VI) Sorption on Ca- and Na-Bentonites. Environ. Sci. Technol 43, 4896–4901.

Milodowski, A.E., Norris, S. and Alexander, W.R. (2016) Minimal alteration of montmorillonite following long-term interaction with natural alkaline groundwater: Implications for geological disposal of radioactive waste. Appl Geochem 66, 184-197.

Missana, T. and García-Gutiérrez, M. (2007) Adsorption of bivalent ions (Ca(II), Sr(II) and Co(II)) onto FEBEX bentonite. Phys Chem Earth 32, 559-567.

Missana, T., Garcia-Gutierrez, M. and Alonso, U. (2008) Sorption of strontium onto illite/smectite mixed clays. Phys Chem Earth 33, S156-S162.

Moll, H., Reich, T. and Szabo, Z. (2000) The hydrolysis of dioxouranium(VI) investigated using EXAFS and O-17-NMR. Radiochim. Acta 88, 411-415.

Moll, H., Rossberg, A., Steudtner, R., Drobot, B., Mueller, K. and Tsushima, S. (2014) Uranium(VI) Chemistry in Strong Alkaline Solution: Speciation and Oxygen Exchange Mechanism. Inorg. Chem. 53, 1585-1593.

Moroni, L.P. and Glasser, F.P. (1995) Reactions between cement components and U(VI) oxide. Waste Manag 15, 243-254.

Morris, D.E., Conradson, S.G., Chisholm-Brause, C.J., Barr, M.E. and Eller, P.G. (1994) Optical spectroscopic studies of the sorption of UO_2^{2+} species on a reference smectite. Geochim. Cosmochim. Acta 58, 3613-3623.

Morss, L.R., Edelstein, N.M. and Fuger, J. (2006) The Chemistry of the Actinide and Transactinide Elements, Third Edition ed. Springer Science + Business Media B.V., Dordrecht, The Netherlands.

Moulin, C., Laszak, I., Moulin, V. and Tondre, C. (1998) Time-Resolved Laser-Induced Fluorescence as a Unique Tool for Low-Level Uranium Speciation. Appl. Spectrosc. 52, 528-535.

Müller, K. (2010) The sorption of uranium(VI) and neptunium(V) onto surfaces of selected metal oxides and alumosilicates studied by in situ vibrational spectroscopy. Technische Universität Dresden, Dresden, Germany.

Müller, K., Brendler, V. and Foerstendorf, H. (2008) Aqueous uranium(VI) hydrolysis species characterized by attenuated total reflection Fourier-transform infrared spectroscopy. Inorg Chem 47, 10127-10134.

Müller, K., Foerstendorf, H., Brendler, V., Rossberg, A., Stolze, K. and Gröschel, A. (2013) The surface reactions of U(VI) on γ-Al$_2$O$_3$ — In situ spectroscopic evaluation of the transition from sorption complexation to surface precipitation. Chem. Geol. 357, 75-84.

Müller, K., Foerstendorf, H., Meusel, T., Brendler, V., Lefèvre, G., Comarmond, M.J. and Payne, T.E. (2012) Sorption of U(VI) at the TiO2–water interface: An in situ vibrational spectroscopic study. Geochim. Cosmochim. Acta 76, 191-205.

Nagra (2002) Entsorgungsnachweis für abgebrannte Brennelemente, verglaste hochaktive sowie langlebige mittelaktive Abfälle - Synthese der geowissenschaftlichen Untersuchungsergebnisse, Technischer Bericht 02-03. Nagra, Wettingen, Switzerland.

Neck, V. and Kim, J.I. (2000) An electrostatic approach for the prediction of actinide complexation constants with inorganic ligands-application to carbonate complexes. Radiochim. Acta 88, 815–822.

Neck, V. and Kim, J.I. (2001) Solubility and hydrolysis of tetravalent actinides. Radiochim. Acta 89, 1-16.

Newville, M. (2004) Fundamentals of XAFS, Consortium for Advanced Radiation Sources. University of Chicago, Chicago, USA.

Nguyen-Trung, C., Palmer, D.A., Begun, G.M., Peiffert, C. and Mesmer, R.E. (2000) Aqueous Uranyl Complexes 1. Raman Spectroscopic Study of the Hydrolysis of Uranyl(VI) in Solutions of Trifluoromethanesulfonic Acid and/or Tetramethylammonium Hydroxide at 25°C and 0.1 MPa. J Solution Chem 29, 101-129.

Nitsche, H. (1995) Synchrotron X-ray absorption spectroscopy: a new tool for actinide and lanthanide speciation in solids and solution. J. Alloys Compd. 223, 274-279.

Nowak, T. and Maßmann, J. (2013) Endlagerstandortmodell Nord (AnSichT) - Teil III: Auswahl von Gesteins- und Fluideigenschaften für numerische Modellberechnungen im Rahmen des Langzeitsicherheitsnachweises. Bundesanstalt für Geowissenschaften und Rohstoffe (BGR), Hannover, Germany.

NUMO (2013) Safety of the Geological Disposal Project 2010 - Safe Geological Disposal Based on Reliable Technologies. Nuclear Waste Management Organization of Japan (NUMO), Tokyo, Japan.

Ochs, M., Mallants, D. and Wang, L. (2016) Radionuclide and Metal Sorption on Cement and Concrete. Springer International Publishing, Switzerland.

OECD/NEA (2006) Physics and Safety of Transmutation Systems - A Status Report, NEA No. 6090. OECD Nuclear Energy Agency, Paris, France.

Ościk, J. (1982) Adsorption. PWN - Polish Scientific Publishers, Warszawa, Poland.

Park, C. and Fenter, P.A. (2007) Phasing of resonant anomalous X-ray reflectivity spectra and direct Fourier synthesis of element-specific partial structures at buried interfaces. J. Appl. Crystallogr. 40, 290-301.

Parkhurst, L. and Appelo, C. (2013) Description of input and examples for PHREEQC version 3 — A computer program for speciation, batch-reaction, one-dimensional transport, and inverse geochemical calculations, Techniques and Methods, book 6. U.S. Geological Survey, Denver, USA.

Philipp, T., Shams Aldin Azzam, S., Rossberg, A., Huittinen, N., Schmeide, K. and Stumpf, T. (2019) U(VI) sorption on Ca-bentonite at (hyper)alkaline conditions - Spectroscopic investigations of retention mechanisms. Sci Total Environ 676, 469-481.

Pierloot, K. and van Besien, E. (2005) Electronic structure and spectrum of UO_2^{2+} and $UO_2Cl_4^{2-}$. J Chem Phys 123, 204309.

Pointeau, I., Landesman, C., Giffaut, E. and Reiller, P. (2004) Reproducibility of the uptake of U(VI) onto degraded cement pastes and calcium silicate hydrate phases. Radiochim. Acta 92, 645–650.

Pointeau, I., Reiller, P., Mace, N., Landesman, C. and Coreau, N. (2006) Measurement and modeling of the surface potential evolution of hydrated cement pastes as a function of degradation. J Colloid Interface Sci 300, 33-44.

Ressler, T. (1998) WinXAS: a program for X-ray absorption spectroscopy data analysis under MS-Windows. J Synchrotron Radiat 5, 118-122.

Richter, C. (2015) Sorption of environmentally relevant radionuclides (U(VI), Np(V)) and lanthanides (Nd(III)) on feldspar and mica, Institut für Ressourcenökologie des Helmholtz-Zentrums Dresden - Rossendorf. Technische Universität Dresden, Dresden, Germany.

Richter, C., Müller, K., Drobot, B., Steudtner, R., Großmann, K., Stockmann, M. and Brendler, V. (2016) Macroscopic and spectroscopic characterization of uranium(VI) sorption onto orthoclase and muscovite and the influence of competing Ca^{2+}. Geochim. Cosmochim. Acta 189, 143-157.

Rossberg, A. (2002) Anwendung der Faktorenanalyse auf die Röntgenabsorptionsspektroskopie zur Bestimmung der Speziation von Uran in Lösungen. Technische Universität Dresden, Dresden, Germany.

Rossberg, A., Reich, T. and Bernhard, G. (2003) Complexation of uranium(VI) with protocatechuic acid - application of iterative transformation factor analysis to EXAFS spectroscopy. Analytical and Bioanalytical Chemistry 376, 631-638.

Rossberg, A., Ulrich, K.-U., Weiss, S., Tsushima, S., Hiemstra, T. and Scheinost, A.C. (2009) Identification of Uranyl Surface Complexes on Ferrihydrite: Advanced EXAFS Data Analysis and CD-MUSIC Modeling. Environ. Sci. Technol 43, 1400-1406.

RWM (2017) Geological Disposal - Concept Status Report. Nuclear Decommissioning Authority (NDA), Radioactive Waste Management Limited (RWM), Harwell Oxford, UK.

Saleh, A.S., Lee, J.Y., Jo, Y. and Yun, J.I. (2018) Uranium(VI) sorption complexes on silica in the presence of calcium and carbonate. J Environ Radioact 182, 63-69.

Schatz, T., Kanerva, N., Martikainen, J. and Sane, P. (2013) Buffer Erosion in Dilute Groundwater. Posiva Oy, Eurajoki, Finland.

Schlegel, M.L., Nagy, K.L., Fenter, P., Cheng, L., Sturchio, N.C. and Jacobsen, S.D. (2006) Cation sorption on the muscovite (001) surface in chloride solutions using high-resolution X-ray reflectivity. Geochim. Cosmochim. Acta 70, 3549-3565.

Schmeide, K. and Bernhard, G. (2010) Sorption of Np(V) and Np(IV) onto kaolinite: Effects of pH, ionic strength, carbonate and humic acid. Appl Geochem 25, 1238-1247.

Schmeide, K., Gürtler, S., Müller, K., Steudtner, R., Joseph, C., Bok, F. and Brendler, V. (2014) Interaction of U(VI) with Äspö diorite: A batch and in situ ATR FT-IR sorption study. Appl Geochem 49, 116-125.

Schmidt, M., Lee, S.S., Wilson, R.E., Soderholm, L. and Fenter, P. (2012) Sorption of tetravalent thorium on muscovite. Geochim. Cosmochim. Acta 88, 66-76.

Schnurr, A. (2015) Untersuchungen zur Radionuklidsorption an Tonmineraloberflächen bei hohen Ionenstärken, Fakultät für Chemie und Biowissenschaften. Karlsruher Institut für Technologie (KIT), Karlsruhe, Germany.

Schnurr, A., Marsac, R., Rabung, T., Lützenkirchen, J. and Geckeis, H. (2015) Sorption of Cm(III) and Eu(III) onto clay minerals under saline conditions: Batch adsorption, laser-fluorescence spectroscopy and modeling. Geochim. Cosmochim. Acta 151, 192-202.

Seher, H. and Bracke, G. (2012) Chemische Vorgänge in einem Endlager für hochradioaktive Abfälle in Ton- und Salzgestein, GRS - 301. Gesellschaft für Anlagen- und Reaktorsicherheit (GRS), Cologne, Germany.

Semenkova, A.S., Romanchuk, A.Y., Krupskaya, V.V., Pokidko, B.V., Dorzhieva, O.V., Sobolev, A.V., Presnyakov, I.A., Verma, P.K., Mohapatra, P.K. and Kalmykov, S.N. (2018) Np(V) uptake by various clays. Appl Geochem 92, 1-8.

Silva, R.J. and Nitsche, H. (1995) Actinide environmental Chemistry. Radiochim. Acta 70/71.

Smith, K.F., Bryan, N.D., Swinburne, A.N., Bots, P., Shaw, S., Natrajan, L.S., Mosselmans, J.F.W., Livens, F.R. and Morris, K. (2015) U(VI) behaviour in hyperalkaline calcite systems. Geochim. Cosmochim. Acta 148, 343-359.

Steudtner, R. (2010) Zur Wechselwirkung von Uran mit den Bioliganden Citronensäure und Glucose, Institut für Radiochemie, Forschungszentrum Dresden-Rossendorf. TU Dresden, Dresden, Germany.

Steudtner, R., Sachs, S., Schmeide, K., Brendler, V. and Bernhard, G. (2011) Ternary uranium(VI) carbonato humate complex studied by cryo-TRLFS. Radiochim. Acta 99, 687-692.

Stumm, W. (1992) Chemistry of the Solid-Water Interface Processes at the Mineral-Water and Particle-Water Interface in Natural Systems. John Wiley & Sons, Inc., New York, USA.

Sylwester, E.R., Hudson, E.A. and Allen, P.G. (2000) The structure of uranium (VI) sorption complexes on silica, alumina, and montmorillonite. Geochim. Cosmochim. Acta 64, 2431-2438.

Takeno, N. (2005) Atlas of Eh-pH diagrams - Intercomparison of thermodynamic databases, in: Japan, G.S.o. (Ed.), Open File Report No.419, Open File Report No.419 ed. National Institute of Advanced Industrial Science and Technology - Research Center for Deep Geological Environments.

Tan, X., Fang, M. and Wang, X. (2010) Sorption speciation of lanthanides/actinides on minerals by TRLFS, EXAFS and DFT studies: a review. Molecules 15, 8431-8468.

Thoenen, T., Hummel, W., Berner, U. and Curti, E. (2014) The PSI/Nagra Chemical Thermodynamic Database 12/07, PSI report 14-04. Paul Scherrer Institut (PSI), Villigen, Switzerland.

Tits, J., Fujita, T., Tsukamoto, M. and Wieland, E. (2008) Uranium(VI) Uptake by Synthetic Calcium Silicate Hydrates. MRS Proceedings 1107, 467-474.

Tits, J., Gaona, X., Laube, A. and Wieland, E. (2014) Influence of the redox state on the neptunium sorption under alkaline conditions: Batch sorption studies on titanium dioxide and calcium silicate hydrates. Radiochim. Acta 102.

Tits, J., Geipel, G., Mace, N., Eilzer, M. and Wieland, E. (2011) Determination of uranium(VI) sorbed species in calcium silicate hydrate phases: a laser-induced luminescence spectroscopy and batch sorption study. J Colloid Interface Sci 359, 248-256.

Tits, J., Walther, C., Stumpf, T., Mace, N. and Wieland, E. (2015) A luminescence line-narrowing spectroscopic study of the uranium(VI) interaction with cementitious materials and titanium dioxide. Dalton Trans 44, 966-976.

Tits, J. and Wieland, E. (2018) Actinide Sorption by Cementitious Materials. Paul Scherrer Institut (PSI), Nuclear Energy and Safety Research Department (NES), Laboratory for Waste Management (LES), Villigen, Switzerland.

Tits, J., Wieland, E. and Bradbury, M.H. (2005) The effect of isosaccharinic acid and gluconic acid on the retention of Eu(III), Am(III) and Th(IV) by calcite. Appl Geochem 20, 2082-2096.

Tournassat, C., Tinnacher, R.M., Grangeon, S. and Davis, J.A. (2018) Modeling uranium(VI) adsorption onto montmorillonite under varying carbonate concentrations: A surface complexation model accounting for the spillover effect on surface potential. Geochim. Cosmochim. Acta 220, 291-308.

Troyer, L.D., Maillot, F., Wang, Z., Wang, Z., Mehta, V.S., Giammar, D.E. and Catalano, J.G. (2016) Effect of phosphate on U(VI) sorption to montmorillonite: Ternary complexation and precipitation barriers. Geochim. Cosmochim. Acta 175, 86-99.

Tsushima, S. (2011) On the "yl" bond weakening in uranyl(VI) coordination complexes. Dalton Trans 40, 6732-6737.

Tsushima, S., Nagasaki, S., Tanaka, S. and Suzuki, A. (1998) A Raman Spectroscopic Study of Uranyl Species Adsorbed onto Colloidal Particles. J. Phys. Chem. B 102, 9029–9032.

U.S.NRC (2014) Safety Evaluation Report Related to Disposal of High-Level Radioactive Wastes in a Geologic Repository at Yucca Mountain, Nevada - Volume 3: Repository Safety After Permanent Closure. Office of Nuclear Material Safety and Safeguards, U. S. Nuclear Regulatory Commission, Washington DC, U.S.

Van Loon, L.R., Glaus, M.A., Stallone, S. and Laube, A. (1997) Sorption of Isosaccharinic Acid, a Cellulose Degradation Product, on Cement. Environ. Sci. Technol 31, 1243-1245.

Verma, P.K., Pathak, P., Mohapatra, M., Yadav, A.K., Jha, S., Bhattacharyya, D. and Mohapatra, P.K. (2015) Spectroscopic investigations on sorption of uranium onto suspended bentonite: effects of pH, ionic strength and complexing anions. Radiochim. Acta 103, 293–303.

Viallis-Terrisse, H., Nonat, A. and Petit, J.-C. (2001) Zeta-Potential Study of Calcium Silicate Hydrates Interacting with Alkaline Cations. J. Colloid Interface Sci. 244, 58-65.

Vuorinen, U., Lehikoinen, J., A., L. and Ervanne, H. (2006) Effects of Salinity and High pH on Crushed Rock and Bentonite – Experimental Work and Modelling, POSIVA 2006-01. Posiva Oy, Olkiluoto, Finland.

Wang, Z., Zachara, J.M., Boily, J.-F., Xia, Y., Resch, T.C., Moore, D.A. and Liu, C. (2011) Determining individual mineral contributions to U(VI) adsorption in a contaminated aquifer sediment: A fluorescence spectroscopy study. Geochim. Cosmochim. Acta 75, 2965-2979.

Wang, Z., Zachara, J.M., Gassman, P.L., Liu, C., Qafoku, O., Yantasee, W. and Catalano, J.G. (2005) Fluorescence spectroscopy of U(VI)-silicates and U(VI)-contaminated Hanford sediment. Geochim. Cosmochim. Acta 69, 1391-1403.

Wang, Z., Zachara, J.M., Yantasee, W., Gassman, P.L., Liu, C. and Joly, A.G. (2004) Cryogenic Laser Induced Fluorescence Characterization of U(VI) in Hanford Vadose Zone Pore Waters. Environ. Sci. Technol 38, 5591-5597.

Warwick, P., Evans, N., Hall, T. and Vines, S. (2004) Stability constants of uranium(IV)-α-isosaccharinic acid and gluconic acid complexes. Radiochim. Acta 92, 897–902.

Warwick, P., Evans, N. and Vines, S. (2006) Studies on some divalent metal α-isosaccharinic acid complexes. Radiochim. Acta 94, 363–368.

Wazne, M., Korfiatis, G.P. and Meng, X. (2003) Carbonate Effects on Hexavalent Uranium Adsorption by Iron Oxyhydroxide. Environ. Sci. Technol 37, 3619-3624.

Wieland, E. (2014) Sorption Data Base for the Cementitious Near Field of L/ILW and ILW Repositories for Provisional Safety Analyses for SGT-E2. National Cooperative for the Disposal of Radioactive Waste (nagra), Wettingen, Switzerland.

Wieland, E. and Van Loon, L.R. (2003) Cementitious Near-Field Sorption Data Base for Performance Assessment of an ILW Repository in Opalinus Clay, PSI Bericht Nr. 03-06. Paul Scherrer Institut, Villigen, Switzerland.

Wieland, E., Wanner, H., Albinsson, Y., Wersin, P. and Karnland, O. (1994) A surface chemical model of the bentonite-water interface and its implications for modelling the near field chemistry in a repository for spent fuel. Swedish Nuclear Fuel and Waste Management Company (SKB), Stockholm, Sweden.

Wolfgramm, M., Thorwart, K., Rauppach, K. and Brandes, J. (2011) Zusammensetzung, Herkunft und Genese geothermaler Tiefengrundwässer im Norddeutschen Becken (NDB) und deren Relevanz für die geothermische Nutzung. Z. Geol. Wiss. 339, 173-193.

Wolter, J.-M., Schmeide, K., Weiss, S., Bok, F., Brendler, V. and Stumpf, T. (2019) Stability of U(VI) doped calcium silicate hydrate gel in repository-relevant brines studied by leaching experiments and spectroscopy. Chemosphere 218, 241-251.

Yamamura, T., Kitamura, A., Fukui, A., Nishikawa, S., Yamamoto, T. and Moriyama, H. (1998) Solubility of U(VI) in highly basic solutions. Radiochim. Acta 83, 139-146.

Appendix

Note: The order of the material in the Appendix (figures, texts and tables) is chronologically, as cross references appear in the thesis.
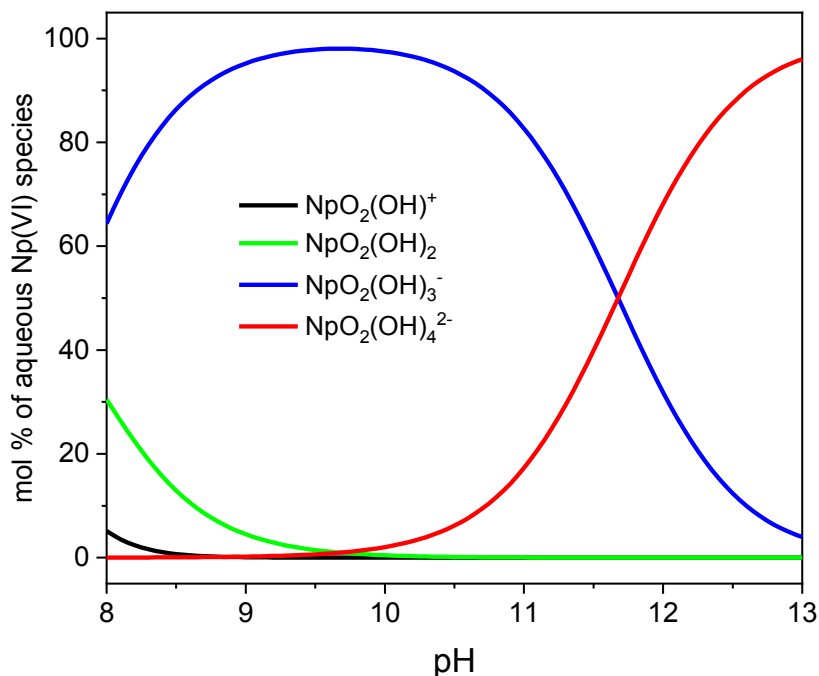

Figure Appendix 1: Aqueous speciation of Np(VI) (1×10^{-11} M) in 0.1 M NaCl in the absence of CO_2 calculated with the geochemical modelling software PHREEQC (Parkhurst and Appelo, 2013), based on thermodynamic data of the PSI/Nagra Chemical Thermodynamic Database 12/07(Thoenen et al., 2014). Stability constant for $NpO_2(OH)_2$ from Gaona et al. (2013).

Table Appendix 1: Elemental composition of Ca-bentonite and muscovite from ICP-MS measurement after digestion and of synthetic kaolinite from SEM-EDX.

elemental composition [wt %]	Ca-bentonite	muscovite	kaolinite (syn.)*
Na	0.22	0.50	-
Mg	0.21	0.48	-
Al	1.87	16.35	15.81
Si	n.d.	18.28	15.98
K	0.40	8.05	-
Ca	0.60	0.04	-
Fe	3.89	1.65	-

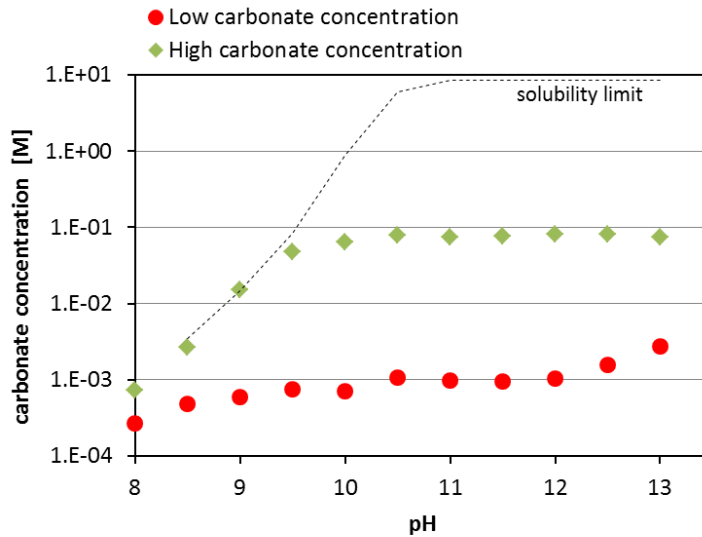n.d.= not determined, * Huittinen *et al.* (2010)

Figure Appendix 2: Measured carbonate concentrations in the supernatant of batch sorption samples after completion of the experiments with low (1 mM) and high (100 mM) amount of carbonate added (here exemplarily shown for U(VI) sorption on Na-montmorillonite).
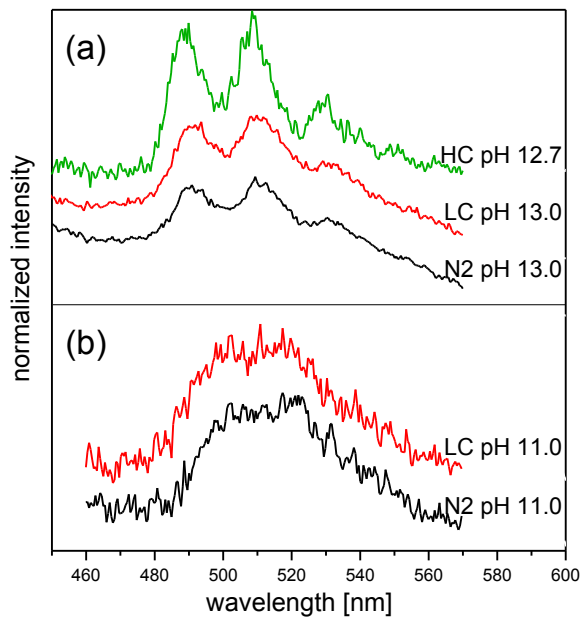

Figure Appendix 3: Comparison of luminescence spectra of uranyl ([U(VI)] = 5×10^{-7} M) in the diluted Gipshut solution at pH 13 (pH 12.7 at high carbonate concentrations) (a) and pH 11 (b) at different carbonate concentrations. Similarity of spectra shows that the aqueous U(VI) speciation is independent of carbonate concentration at such elevated pH. (carbonate concentrations of the series N_2, LC and HC as described in chapter 3.3)
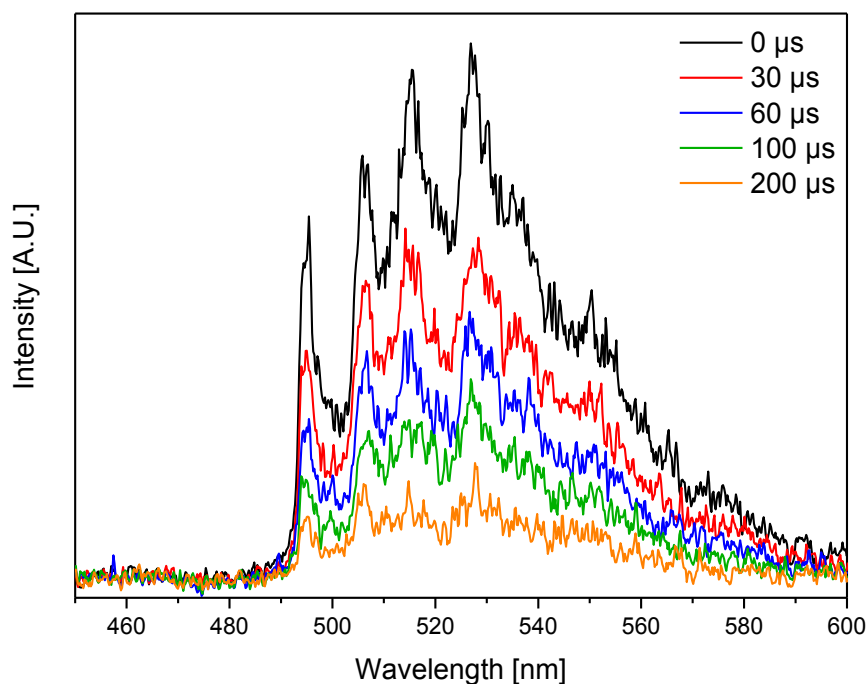
Figure Appendix 4: Luminescence emission spectra at λ_{ex}=494.3 nm of U(VI) ([U(VI)] = 5×10^{-7} M) sorbed on Ca-bentonite in the absence of CO_2 at pH 11 at different delay time (as indicated in the diagram). The intensity of all emission bands decreases uniformly with increasing delay time. Hence, coexisting species do not feature different luminescence lifetimes.
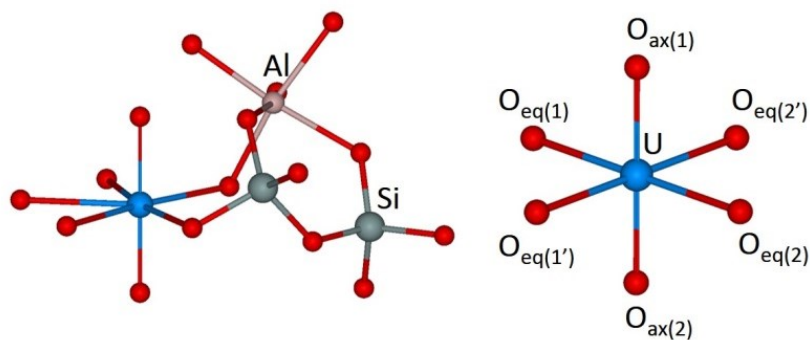

Figure Appendix 5: Arbitrary structural model of the sorption complex and of the aqueous $UO_2(OH)_4^{2-}$ complex used for the calculation of theoretical phase and amplitude functions by FEFF8.20. O_{ax}: axial oxygen, O_{eq}: equatorial oxygen.
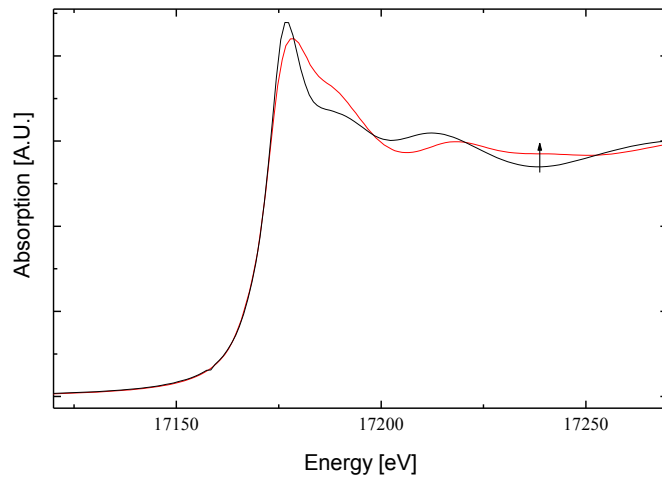
Figure Appendix 6: U L$_{III}$-edge XANES spectrum of UO$_2$(H$_2$O)$_5^{2+}$ (black) and UO$_2$(OH)$_4^{2-}$ (red). Arrow marks position of the multiple scattering (MS) feature at 17,240 eV resulting from U-O$_{eq(1)}$-U-O$_{eq(2)}$ and U-O$_{eq(1)}$-U-O$_{eq(1)}$ MS paths.
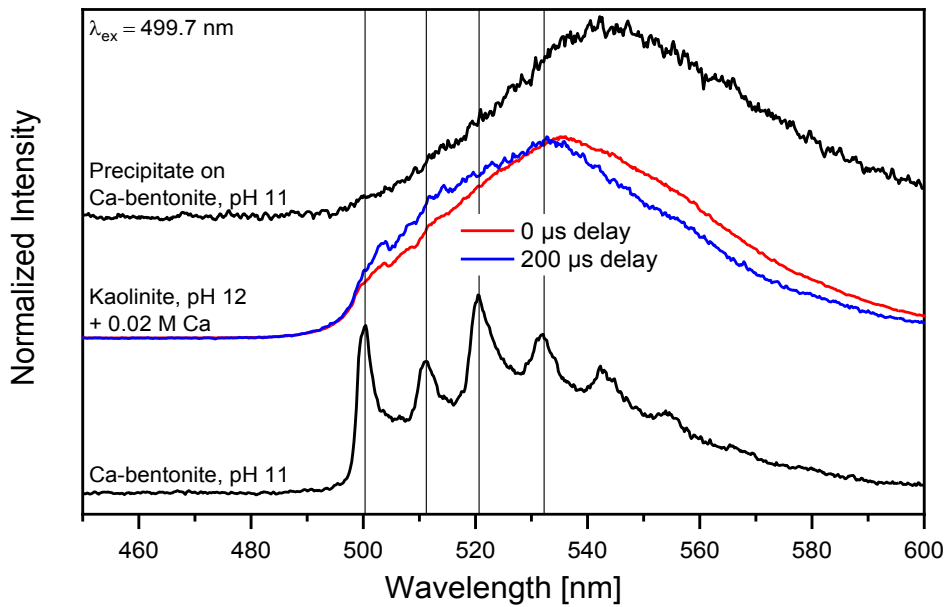

Figure Appendix 7: Normalized luminescence emission spectra at λ$_{ex}$=499.7 nm of U(VI) ([U(VI)] = 5×10^{-7} M) sorbed on kaolinite in the absence of CO$_2$ at pH 12 in 0.1 M NaCl + 0.02 M CaCl$_2$ at 0 and 200 μs delay time. Spectra of U(VI) sorbed on Ca-bentonite and of a uranate-like precipitate on Ca-bentonite (both at pH 11) are included for comparison. Vertical lines in the graph attribute different emission lines to two independent species (presented in chapter 4.2.4.2).

Publications

Articles in peer-reviewed journals

Published

Philipp, T., Shams, S., Rossberg, A., Huittinen, N., Schmeide, K., Stumpf, T. (2019) U(VI) sorption on Ca-bentonite at (hyper)alkaline conditions – Spectroscopic investigations of retention mechanisms. Science of the Total Environment. Volume 676, 469-481.

Philipp, T., Amann-Hildenbrand, A., Laurich, B., Desbois, G., Littke, R., Urai, J. L. (2017) The effect of microstructural heterogeneity on pore size distribution and permeability in Opalinus Clay (Mont Terri, Switzerland): insights from an integrated study of laboratory fluid flow and pore morphology from BIB-SEM images. Geological Society, London, Special Publications. Volume 454, 85-106.

In preparation

Philipp, T., Shams, S., Huittinen, N., Häussler, V., Stern, T., Reich, T., Schmeide, K., Stumpf, T.: Influence of calcium on U(VI) and Np(VI) sorption on clay minerals at (hyper)alkaline conditions. Environmental Science and Pollution Research, in preparation.

Oral presentations at international conferences

Philipp, T., Schmeide, K., Rossberg, A., Huittinen, N., Stumpf, T.: Influence of pH, carbonate and calcium concentration on U(VI) retention by clay minerals at (hyper)alkaline conditions – A batch sorption and spectroscopy study. International Conference on Clay Science and Technology – EUROCLAY 2019, 01.-05.07.2019, Paris, France.

Philipp, T., Schmeide, K., Stumpf, T.: Influence of calcium on uranium and neptunium sorption on clay minerals at (hyper)alkaline conditions. 2nd International Conference on Radioanalytical and Nuclear Chemistry, May 5-10, 2019, Budapest, Hungary.

Philipp, T., Schmeide, K., Rossberg, A., Stumpf, T.: U(VI) sorption by Ca-bentonite at pH 8-13: Spectroscopic investigation of retention mechanisms. 28th Goldschmidt Conference 2018, August 12-17, 2018, Boston, USA.

Poster presentations at international conferences

Philipp, T., Schmeide, K., Rossberg, A., Stumpf, T.: Competition of U(VI) hydroxide and carbonate complexation in alkaline solutions − implications for U(VI) retention by Ca-bentonite. RadChem 2018 - 18th Radiochemical Conference, May 13-18, 2018, Mariánské Lázně, Czech Republic.

Philipp, T., Schmeide, K., Stumpf, T.: Retention of uranium(VI) by Ca-bentonite at high ionic strength and high pH studied by batch sorption tests and TRLFS. 7th International Conference on Clays in Natural and Engineered Barriers for Radioactive Waste Confinement, September 24-27, 2017, Davos, Schweiz.

Philipp, T., Schmeide, K., Stumpf, T.: U(VI) sorption by Ca-bentonite under alkaline and saline conditions as a function of pH and carbonate content. Migration 2017 - 16th International Conference on the Chemistry and Migration Behaviour of Actinides and Fission Products in the Geosphere, September 10-15, 2017, Barcelona, Spain.

Versicherung

Hiermit versichere ich, dass ich die vorliegende Arbeit ohne unzulässige Hilfe Dritter und ohne Benutzung anderer als der angegebenen Hilfsmittel angefertigt habe; die aus fremden Quellen direkt oder indirekt übernommenen Gedanken sind als solche kenntlich gemacht. Die Arbeit wurde bisher weder im Inland noch im Ausland in gleicher oder ähnlicher Form einer anderen Prüfungsbehörde vorgelegt.

Köln, den …………………

Eidesstattliche Erklärung

Die vorliegende Arbeit wurde am Helmholtz-Zentrum Dresden-Rossendorf (Institut für Ressourcenökologie) in der Zeit von Dezember 2015 bis Mai 2019 unter der wissenschaftlichen Betreuung von Herrn Prof. Dr. Thorsten Stumpf und Frau Dr. Katja Schmeide angefertigt.

Köln, den …………………